

**Modelling and Control of Integrated PV-Converter Modules under
Partial Shading Conditions**

Javier González Garza

Submitted in accordance with the requirements for the degree of
Doctor of Philosophy

The University of Leeds
School of Electronic & Electrical Engineering

December, 2013

Intellectual Property and Publication Statements

The candidate confirms that the work submitted is his/her own, except where work which has formed part of jointly-authored publications has been included. The contribution of the candidate and the other authors to this work has been explicitly indicated below. The candidate confirms that appropriate credit has been given within the thesis where reference has been made to the work of others.

Some of the work presented in Chapter 5 of this thesis has been published or submitted for publication in the follow article:

- Garza, J.G.; Chong, B.; Zhang, L., "Control of integrated Ćuk converter and photovoltaic modules for maximum power generation," Power Electronics for Distributed Generation Systems (PEDG), 2012 3rd IEEE International Symposium , pp.175,181, 25-28 June 2012

The work contained within the above publication which is directly attributable to the candidate includes the converter design, simulation, experimental work and preparation of the article. The work directly attributable to others authors include the participation in experimental work and editing of the article.

This copy has been supplied on the understanding that it is a copyright material and that no quotation from the thesis may be published without proper acknowledgment.

The right of Javier González Garza to be identified as Author of this work has been asserted by him in accordance with the Copyright, Designs and Patents Act 1988.

Acknowledgements

Firstly, I am very grateful to my Supervisor Dr Li Zhang for her guidance, support and encouragement throughout the whole Ph.D. program. Her energy and advice were an inspiration during all this time. Special thanks go to Dr. Chong for his help through the entire course.

I thank my Mother, Sister and Brother and all the family for the support during this time away.

I thank my friends Azael, Alexis, Camille, Paula, Vicky among others, that without them my time in Leeds would not have been the same.

I express my gratitude to the Mexican Government and CONACYT for their sponsorship throughout the degree.

Finally, thanks to the love of my life, my girlfriend Gris for her full support and being with me all these years and the ones to come.

Abstract

It has been well-recognized that non-uniform solar irradiation of photovoltaic (PV) panels causes electrical mismatching of cells and may result in reduced output power and cell thermal breakdown. Bypass diodes are commonly used, but challenges exist into obtaining the maximum power point tracking in these partially shaded PV panels for each weather condition. This is due to that there are multiple peak power points present in their Power-Voltage characteristic curves which makes difficult to locate the global maximum power point. The work presented in this thesis studies in detail the converter topologies and control methods which can be used in the PV power generation systems to overcome effectively the shortcomings caused by partial shading.

The proposed topology is an integrated bi-directional Ćuk converter and PV-panel module. The particular example investigated includes two PV panels connected across two terminals of the Ćuk converter. The features of this system in power harness are studied under partial shading conditions, its superior performance in power generation is demonstrated through simulation and practical tests. The generated power is 30% higher than that from a two PV panel system using only bypass diodes.

To develop the control schemes for the above system a detailed study was performed leading to the derivation of the transfer function model describing the dynamic responses of voltages across the two PV panels corresponding to the variations of converter switch duty ratio. Experimental verification of this confirms that the model is sufficiently accurate for the application of controller design and tests.

A novel maximum power point tracking scheme is developed. This consists of a switching selection scheme and a model based on an optimal control algorithm. The former determines which switch-diode pair in the bidirectional Ćuk converter to be active according to measured light levels on each PV panel and the ability to

predict the optimal voltage values across the individual PV panels under any practical irradiance and temperature levels. The performance of the controller is tested in simulation as well as in practice under various modes of partial shading, all giving desired results in achieving the maximum power generation.

The final contribution lies in the design and construction of an experimental prototype consisting of an inner bidirectional Ćuk converter across two PV panels and a terminal boost converter, controlled by DSP-based microcontroller. This set-up enables further development and verification of the control schemes for this integrated converter and PV-panel system.

Keywords: Photovoltaic Systems, Partial Shading, Ćuk Converter, DC-DC Power Converters, Solar Power Generation, Maximum Power Point Tracking, Bypass Diode.

Content

Intellectual Property and Publication Statements	ii
Acknowledgements	iii
Abstract	iv
Content	vi
List of Figures	x
List of Tables	xiv
List of Symbols and Abbreviations	xv
Chapter 1	1
1.1 The Photovoltaic Energy	1
1.2 Aim and Objectives of the Thesis	4
1.3 Thesis Structure.....	5
Chapter 2	7
2.1 Mathematic Models for PV Panels.....	8
2.1.1Equivalent Circuit Representation and Single Diode Model...8	
2.1.2Mathematical Expressions for Single-Diode Model.....9	
2.1.3The Bishop Model.....	10
2.1.4Model Parameters	11
2.2 Numerical Methods for Photovoltaic Cell Simulation	17
2.2.1The Newtown-Raphson Iterative method.....	17
2.2.2Bishop's proposed model.....	20
2.3 PV Panels under Partial Shading Conditions.....	23
2.3.1Effects of Light and Temperature to PV panel output power23	
2.3.2Causes and Consequences of Partial Shading.....	24
2.3.3The use of Bypass Diode for Partial Shading	26
2.4 Analysis of a photovoltaic panel for experimental setup	28
2.4.1I-V Characteristic Curves of the PV panels.....	29
2.4.2Typical I-V and P-V characteristics of PV panels under partial shading	31

2.4.3 Three PV panels under partial shading conditions with Bypass Diode	32
2.5 Integrated Converter PV Unit for Partial Shading	33
2.6 Summary	37
Chapter 3	38
3.1 Ćuk Converter Circuit.....	39
3.2 Operation Principle	40
3.2.1 Circuit Analysis	40
3.2.2 Analysis of Components Selection in a Photovoltaic Converter	
43	
3.3 Bidirectional Ćuk Converter with photovoltaic application.....	46
3.3.1 Bidirectional Ćuk Converter	46
3.3.2 Application of a bidirectional Ćuk converter with two PV panels	47
3.4 Operations under Uneven Solar irradiation.....	49
3.4.1 Case when Irradiation over PV_1 is greater than PV_2	49
3.4.2 Case when irradiation over PV_2 is greater than PV_1	50
3.4.3 Power Flow Analysis.....	50
3.5 Integrated-converters with three PV Panels.....	53
3.6 Converter components design	56
3.7 Discontinuous Conduction Mode (DCM).....	57
3.8 Summaries.....	58
Chapter 4	59
4.1 State-Space Equations for Ćuk Converter	59
4.2 Introducing Small ac Perturbation Signals	64
4.3 Transformation of ac Equations to Transfer Functions	66
4.4 Verification of Analysis and Simulation Verification of the Two Transfer functions	68
4.5 Summary & conclusions	81
Chapter 5	82
5.1 Open Loop Test	82
5.1.1 Resistive load	83
5.1.1.1 Solar Modules with Bypass Diodes.....	83

5.1.1.2	Bidirectional Ćuk Converter + PV + Resistive Load	84
5.1.1.3	Comparison	86
5.1.2	DC Bus connected to the system.....	88
5.1.2.1	Solar modules with bypass diode and Boost converter.....	89
5.1.2.2	1 Bidirectional Ćuk Converter + PV + Boost Converter + DC Bus.....	91
5.1.2.3	Comparison	92
5.1.3A	comparison of bypass diode and integrated converter with three solar modules	94
5.2	Closed loop Control of Integrated Converter PV modules	98
5.2.1A	comparison of two MPPT implemented in closed loop ...	102
5.2.1.1	Perturb and Observe in closed loop system	102
5.2.1.2	Real-Time Model for MPPT	107
5.3	Summary	111
Chapter 6	113
6.1	Bidirectional Ćuk Converter	114
6.1.1	Efficiency	117
6.2	Photovoltaic System Interface	118
6.2.1	Hardware	118
6.2.1.1	Light Irradiance and Temperature Sensor	118
6.2.1.2	Voltage & Current Transducers	120
6.2.1.3	Microcontroller eZdsp™ F28335.....	123
6.2.1.4	PWM Driver	126
6.2.2	Software.....	127
6.2.2.1	Matlab Simulink Embedded Encoder and Code Composer Studio	127
6.2.2.2	Signal Conditioning.....	128
6.3	Summary	132
Chapter 7	133
7.1	Open loop Test	133
7.1.1	Experimental results versus Transfer Function Model	133
7.2	Closed-Loop Tests.....	137

7.2.1 Step responses under equal light level $G_1=G_2=100\%$	137
7.2.2 Step responses under partial shading over PV1	140
7.2.3 System responses for different shading conditions.....	143
7.3 Summary	147
Chapter 8	148
8.1 Recommendations for Future Work	151
Appendix A.....	152
Appendix B.....	154
Appendix C.....	155
Appendix D.....	157
Appendix E.....	158
Appendix F.....	161
Appendix G.....	162
Appendix H.....	165
Appendix I.....	166
Appendix J.....	167
Appendix K.....	168
Bibliography.....	169

List of Figures

Figure 1.1 Evolution of PV capacity installed in Megawatts [1].....	1
Figure 2.1 Equivalent circuit of a solar cell	8
Figure 2.2 Solar cell equivalent circuit by J.W. Bishop	10
Figure 2.3 Example for silicon Photon Energy (eV) vs. Wavelength (μm) [3]	12
Figure 2.4 Radiation power vs. Wavelength [3].....	13
Figure 2.5 Effects of R_p and R_s over the I-V Curve.....	15
Figure 2.6 a) Solar cells in series b) Solar cells in parallel	16
Figure 2.7 I-V and P-V Characteristic curve obtained by iterative process	20
Figure 2.8 I-V characteristic curve with Bishop's equations.....	21
Figure 2.9 I-V and P-V Characteristic curve obtained by Bishop Model	22
Figure 2.10 PV curve simulation with different sunlight proportion	23
Figure 2.11 PV curve simulation with different temperature.....	24
Figure 2.12 Comparison of string of cells in full sun and in partial shading	25
Figure 2.13 Example of a PV panel under partial shading.....	26
Figure 2.14 Two solar cells + diode connected in series under partial shading	27
Figure 2.15 I-V curve with bypass diodes under different irradiance level	28
Figure 2.16 Solar Setup	29
Figure 2.17 PV connection to extract the I-V Curve	30
Figure 2.18 IV Curve from the PV installation.....	31
Figure 2.19 Local and Global MPP	32
Figure 2.20 Bypass diode + three PV panels under uneven irradiance	33
Figure 2.21 Evolution of Grid connected PV Market Segmentation [1].	34
Figure 2.22 Overview of PV Inverters (a) Central Inverter, (b)String Inverter, (c)Multi-string Inverter, (d)Module Integrated Inverters ..	36
Figure 2.23 Bypass dc-dc Module Integrated Converter	37
Figure 3.1 Basic Cuk Converter.....	39

Figure 3.2 Switching On-State and Off-State of the Ćuk converter	40
Figure 3.3 Ćuk converter waveforms at On/Off State a) inductor currents and voltages, b) C_n current and voltage, Switch voltage and current.	41
Figure 3.4 Output current and voltage waveforms for the Ćuk Converter	44
Figure 3.5 Interconnection of two PV Panels with the Bidirectional Ćuk Converter.....	47
Figure 3.6 Integrated Photovoltaic Converter connected to a DC Bus .	48
Figure 3.7 Switch Stage of the Ćuk Converter with $G_1 > G_2$	49
Figure 3.8 Switch Stage of the Ćuk Converter with $G_2 > G_1$	50
Figure 3.9 Configuration for three Solar Panel System.....	53
Figure 4.1 Switch State Analysis	60
Figure 4.2 I-V characteristic from Pv1 at 100% and Pv2 at 50%.....	70
Figure 4.3 Step Response of V_{PV1} with different K values with $G_1=100\%$	71
Figure 4.4 Step Response of V_{PV2} with different K values with $G_2=50\%$	72
Figure 4.5 Bode plot of V_{pv1} for different K.....	73
Figure 4.6 Bode plot of V_{pv2} for different K.....	73
Figure 4.7 Transfer function G_{k1} and its pole-zero location plots for different K.....	76
Figure 4.8 Transfer function G_{k2} and its pole-zero location plots for different K.....	78
Figure 4.9 Step Response of V_T with different K values.....	79
Figure 4.10 MATLAB/SIMULINK simulation of PV-Ćuk Converter system step response of V_{PV1} and step response of V_{PV2}	80
Figure 5.1 PV Panels with bypass diodes and load	83
Figure 5.2 Bidirectional Ćuk Converter with resistive load.....	85
Figure 5.3 Gain ΔP Power chart.....	88
Figure 5.4 Boost converter and DC Bus	89
Figure 5.5 Integrated bypass diode with DC Bus.....	89
Figure 5.6 Simulink setup of 2 PV Panels with Ćuk Converter with a Boost Converter at the output, a resistive load and DC Bus	91
Figure 5.7 Power gain using the Integrated Converter	94
Figure 5.8 Three Panels with Bypass Diode	95

Figure 5.9 Three PV panels with two Integrated Bidirectional Ćuk Converters.....	96
Figure 5.10 First order linearization	101
Figure 5.11 Vmpp model simulation.....	102
Figure 5.12 Response of P&O during an irradiation mismatch	104
Figure 5.13 Simulation with automatic response.....	106
Figure 5.14 Improved switch scheme flowchart and Simulink Models	107
Figure 5.15 Block diagram of the integrated converter in close loop .	108
Figure 5.16 Results Ćuk Converter with online model.	110
Figure 6.1 Photovoltaic converter with module integrated converter and sensors	114
Figure 6.2 Bidirectional Ćuk Converter.....	116
Figure 6.3 Efficiency graph of the Ćuk Converter	117
Figure 6.4 Irradiance and Temperature Sensor.....	119
Figure 6.5 Solar Module with Temperature and Irradiance Sensors ...	119
Figure 6.6 Voltage transducer block diagram	120
Figure 6.7 Voltage transducer circuit mounted.....	121
Figure 6.8 Connection diagram of current transducer LA 25-NP	122
Figure 6.9 Current transducers boxed	122
Figure 6.10 Transducers control box	123
Figure 6.11 eZdsp™ F28335 board with interface box.....	125
Figure 6.12 PWM driver Block diagram.....	126
Figure 6.13 PWM Driver	127
Figure 6.14 Simulink model with F28335 board support	128
Figure 6.15 ADC conversion configuration	129
Figure 6.16 ePWM Generation	131
Figure 6.17 ePWM block configuration	131
Figure 6.18 Hardware Final implementation	132
Figure 7.1 Integrated converter with PV	134
Figure 7.2 Response to Duty ratio of PV1 and PV2.....	135
Figure 7.3 Transfer Function terminal response.....	136
Figure 7.4 PV1 and PV2 step response, no shading.....	139
Figure 7.5 Terminal step response, no shading.....	139

Figure 7.6 Switching signals for converter switches under equal light level.....	140
Figure 7.7 Responses of PV₁ and PV₂ with 30% Partial shading on PV₁	141
Figure 7.8 Terminal responses with PV model for a 30% Partial shading on PV₁	142
Figure 7.9 Switching signals for converter switches under a shading condition.....	142
Figure 7.10 Terminal responses with P&O for a 30% Partial shading on PV₁.....	143
Figure 7.11 Irradiation changes over time	144
Figure 7.12 PV1 and PV2 measurements to dynamic response	146
Figure 7.13 Terminal measurements to dynamic response	146
Figure 7.14 PWM switch signal when $G_2/G_1 < 0.7$	147

List of Tables

Table 2-1 Single solar cell parameters.....	19
Table 2-2 Different irradiance cases.....	32
Table 3-1 Switch/Diode Bidirectional behaviour	48
Table 3-2 Three Panel Case switching configuration	56
Table 5-1 Bypass Diode Power Chart.....	84
Table 5-2 PV Integrated Ćuk Converter Power Chart.....	86
Table 5-3 Comparison of power produced	87
Table 5-4 Power chart of Integrated bypass diode with DC bus.....	90
Table 5-5 Power chart of integrated converter with DC Bus	92
Table 5-6 Power Gain Chart bypass diode and integrated converter....	93
Table 5-7 Three Panel with Bypass Diode	96
Table 5-8 Three PV panels with Bidirectional Ćuk Converter	97
Table 5-9 Contrast of two methods with three PV Panels	98
Table 5-10 P+I controller values	108
Table 6-1 Ćuk converter components values.....	114
Table 6-2 ADC acquisition signal channels.....	129
Table 6-3 ADC Scaling factor	130
Table 7-1 Dynamic Irradiation and switch activation.....	144

List of Symbols and Abbreviations

A	Ideality factor of silicon material used in cell
a	Fraction of ohmic current involved
C	Capacitance (Farads)
C_n	Transfer Capacitance (Farads)
E_g	Energy band gap of one cell in eV
f	Frequency (Hz)
G	Percentage of solar irradiance (%) 100%= 367mW/cm ²
G_{k1}	Transfer Function for Vpv1
G_{k2}	Transfer Function for Vpv2
H	Solar Irradiance (mW/cm ²)
I_{or}	reverse saturation I at ref T in Amps
I_{PV}	Current across the PV Panel in Amps
I_s	Leakage current in Amps
I_{sc}	Photovoltaic current in Amps
I_{scr}	Cell short circuit I at ref T in Amps
I_T	Current across the Terminal in Amps
k	Boltzmann constant
K	Duty ratio
k_i	Short circuit current temperature coefficient at I_{scr} in Amps/Celsius
L	Inductance (Henry)
m	Avalanche Breakdown Exponent
MPPT	Maximum Power Point Tracker
n_p	Numbers of PV cells connected in parallel
n_s	Numbers of PV cells connected in series
P&O	Perturb and Observe
P_{PV}	Power across the PV Panel (Watts)
P_T	Power across the Terminal (Watts)
q	Electron charge in Coulomb
R	Load resistance in ohms)

R_p	Parallel resistance in Ohms
R_{pv}	resistance across PV panel in Ohms
R_s	Series resistance in Ohms
R_{sht}	Total parallel resistance in Ohms
R_{st}	Total series resistance in Ohms
T_{cell}	Cell temperature in K°
T_r	Reference temperature in K°
V_{br}	Junction Breakdown Voltage
V_{bus}	Voltage Across DC Bus in Volts
V_{Cn}	Voltage across capacitor C_n in Volts
V_{mpp}	Predicted MPP voltage in Volts
V_o	Voltage Output in Volts
V_{PV}	Voltage across capacitor PV panel in Volts
V_r	Voltage Ripple at output in Volts
V_s	Voltage Source in Volts
V_T	Voltage across the Terminal in Volts

Chapter 1

Introduction

1.1 The Photovoltaic Energy

Energy demand increases every day across the world and with it the need for practical and simple solutions to satisfy the modern market. Solar energy and the importance of improving its control and management is a major area in Electrical Engineering. PV market has increase exponentially (Figure 1.1) due to each years price reductions in installation materials opening new opportunities for energy production in grid connected and off-grid connected applications [1].

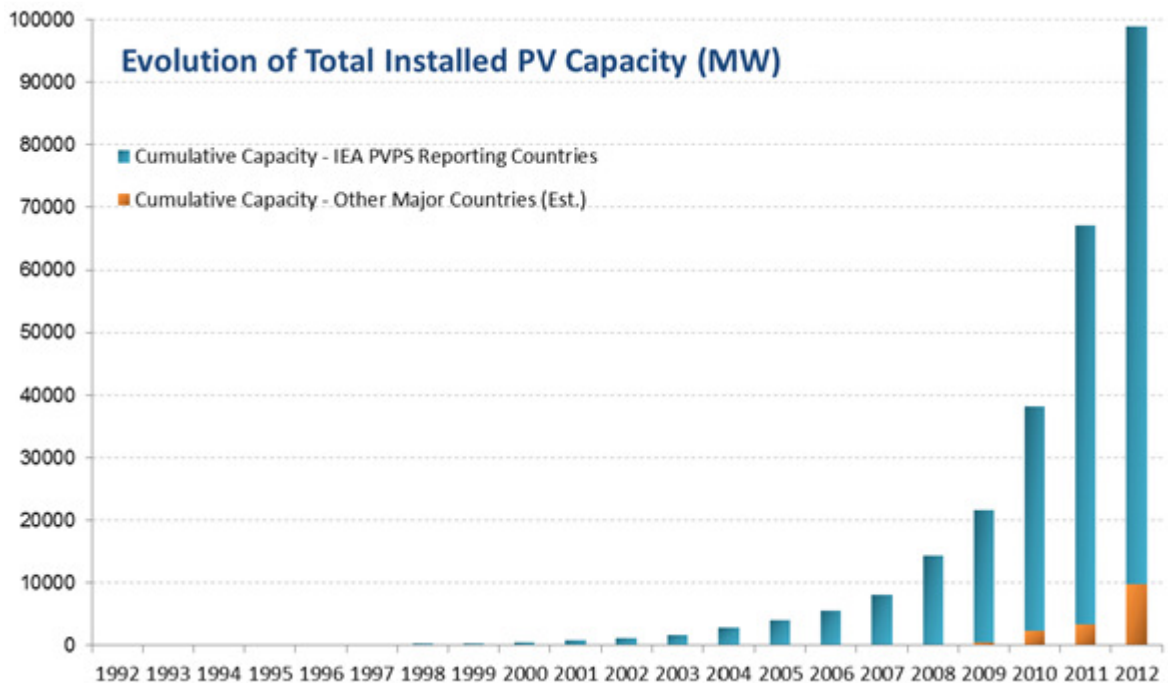


Figure 1.1 Evolution of PV capacity installed in Megawatts [1]

Photovoltaic cells have an average size of 15cmx15cm in each PV panel. Cells can be made from different materials are generally classified as wafer-based crystalline, (monocrystalline and polycrystalline silicon, compound semi-conductor) and thin film and organic. Currently 80% of all installations reported are based on crystalline silicon technology [1], [2].

Modern PV power generators are composed of many tens or hundreds of solar cells connected in series and/or parallel to form a PV module. Multiple modules are connected to form a PV panel capable of generating power at voltage and current levels comparable to the load requirement. Solar modules are typically rated from 50 W to 300 W but sometimes with greater capacity for specialized for building integrated PV systems. A group of solar modules is called PV array, which can consist of a number of modules connected in series or parallel depending the output required [1], [3].

The role that power electronic converters play in photovoltaic technology is crucial for the performance of the harvested energy from the sun through the panels. Because there are different voltage levels that a photovoltaic application can use and variable amounts of power that can be produced, a fixed output is needed to get the best performance of the plant such as a deep discharge lead-acid battery (e.g. NiCad, NiMH, LiO) for “Off-Grid” systems, or the alternating current and voltage levels of an “On-Grid” electricity network. The design of a photovoltaic system with the integration of all the features to overcome problems in the solar cells physics is critical in order to make photovoltaics a possible solution for the energy industry [4].

Solar converters are usually controlled by algorithms called Maximum Power Point Trackers (MPPT), which ensure the optimal control and management of a photovoltaic plant. The amount and quality of power harnessed from the PV panels will depend on the performance of these trackers in all possible illumination scenarios. Since PV panel characteristics are nonlinear and vary with irradiation and temperature, the system needs a fast and adaptable response [5].

Since the creation of PV modules, an inherent problem occurs when the irradiation over the modules are uneven, the issue is known as “Partial shading” [6]. When the partial shading is present over a string of solar panels, power generation declines due to internal resistors inherent to the physics of the solar cell. A commercial protection integrated to a solar panel is known as “Bypass Diode”, which is connected by the manufacturer in parallel by the terminals of the module and with this stop the solar module to consume the energy by the internal resistors integrated in the photovoltaic material. Figure 1.2 represents the daily production of a string with one panel under partial shading presented in Figure 1.3. The shade being casted over the solar module is from a building next to the installation. The production decreases a yearly average of 20% due to this case of partial shading and the lack of a good maximum power point tracker. Since the commercial value of a PV installation represents an average of \$5.00dolls/watt and the average domestic installation is around 3kWp, the initial investment would be of 15,000.00dolls, the yearly payback is being delay by 20% due to shading.

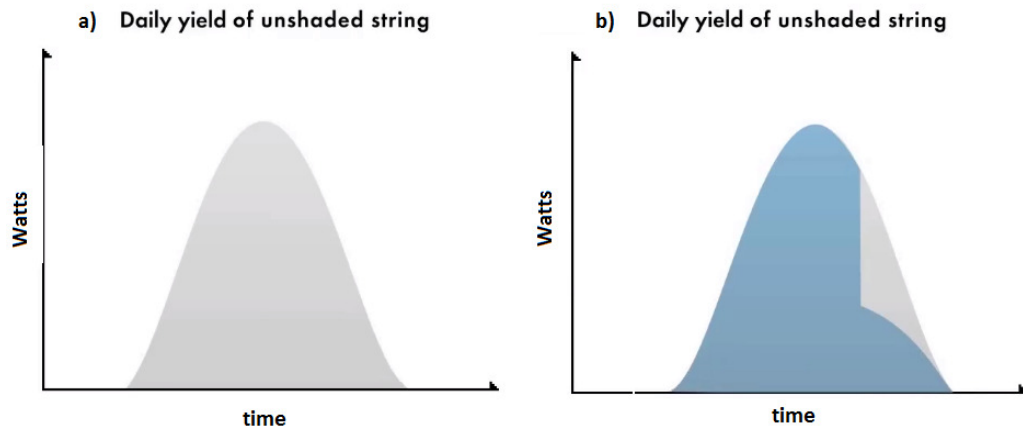


Figure 1.2 Generation over a day affected with partial shading

Partial shading is frequently found in PV installations, from domestic represented by a tree, a chimney or a nearby building (Figure 1.3) to Solar Farms represented as dust, bird drops or the shadow casted by the front row of PV modules (Figure 1.4). The partial shading problem could be mitigated with a good design of power

optimizer composed by a DC/DC converter and optimum MPPT algorithm in order to extract the maximum power available from the solar modules with shading problems.



Figure 1.3 Real case partial shading

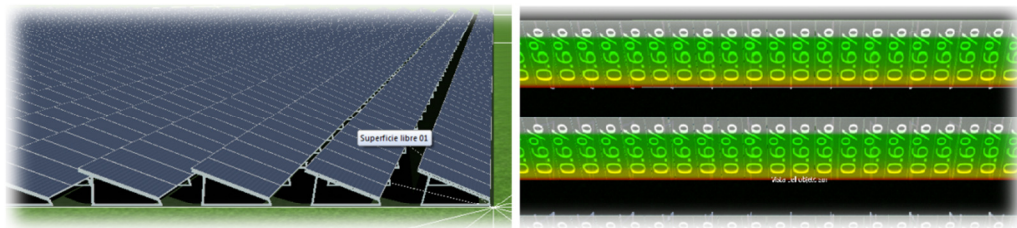


Figure 1.4 Optimal situations in solar farm with 0.6% of daily partial shading

1.2 Aim and Objectives of the Thesis

The scope of the thesis is to design and control an optimal integrated PV-Converter which includes PV panels connected in series presenting a mismatch in the solar irradiation over the modules solving the partial shading issue inherent to the PV modules.

The key objectives of this work are:

1. A complete analysis of the PV modules as a renewable source and the understanding of the limitations of this energy solution
2. A study of proposed solutions over the years for the partial shading issue within PV installations.
3. The development of a computer model to simulate the partial shading effect.
4. A thorough study of the Bidirectional Ćuk Converter as a solution for the partial shading.
5. Develop of a control scheme to increase the power production from the Integrated PV-Converter module and compare it with bypass diode solution.
6. Design and construct an experimental Integrated PV-Converter and implement the proposed control algorithm to provide validation of the research.

1.3 Thesis Structure

This thesis is divided into eight chapters and the outline is as follows:

Chapter 1 presents a global overview of the potential of Photovoltaic energy productions nowadays. Photovoltaics playing an important role in the renewable power industry since the combination of decreasing prices and a higher demand of energy have given it an exponential growth. The aim of the thesis is also stated.

Chapter 2 describes an overview of the features of the PV panels and mathematical models stated over the years are compared using simulation. The "Partial shading issue" is introduced by an inherent feature attributed to the physics of the solar cell, affecting directly the power production. An analysis of the I-V curve under partial shading and a survey of different solutions to avoid this problem are also performed.

Chapter 3 discusses the Ćuk converter as a solution for an uneven irradiation upon a chain of PV modules. The feature of bidirectional solar converter integrated with two PV modules is developed by circuit analysis. The switch scheme is presented

depending on irradiation levels. Expansion possibility of for three PV panels and the switch scheme is discussed.

Chapter 4 describes a thorough circuit analysis where a mathematical model in the Laplace “s” domain is obtained from state space equations and ac small signal analysis. Introduction of perturbations to the duty ratio are use to analyse the voltage step and frequency response in each PV panel.

Chapter 5 describes an exhaustive list of tests performed to different connections in open loop to solve the partial shading in PV panels. A novel control algorithm is designed from analysis to increase the power produced by the PV panels under uneven irradiance conditions. Maximum power point trackers are explained and compared using closed loop simulations where the Vmpp model presents a better control than the P&O algorithm.

Chapter 6 presents the hardware design and construction of an experimental PV system integrated with a bidirectional Ćuk converter. A systematic hardware design is presented including transducers, PWM drivers and converters. Control of the system is performed by a Digital Signal Processor (DSP) is described using high level programming with Matlab/Simulink.

Chapter 7 presents the responses of the practical converter applying different duty ratios in open loop confirming the simulation of the Transfer Functions in Chapter 4. Experimental validation of the proposed control algorithm in closed loop and Integrated PV-Converter system is also described

Chapter 8 summarizes the research findings and provides recommendations for future development of the work.

Chapter 2

Models for Photovoltaic Panels and Their Operations under Partial Shading

Modelling of Photovoltaic cells is important for understanding and predicting of the behaviour of a PV panel under different weather and operating conditions. Furthermore, it facilitates the controller design for achieving the maximum power generation. Developing PV cell/panel models has been a well-researched topic, studied and improved over the years by researchers [7]–[14]. However, it remains an on-going work to develop models that offer sufficient accuracy and computational efficiency, particularly for panels and their associated systems under unusual operating conditions, such as partial shading.

The issues of PV panels operating under un-equal irradiation conditions have been studied through advanced modelling and detailed investigations on various practical PV applications such as analysis of the multiple power peaks generated by partial shading [7], reverse characteristics of solar cells [8], modelling according to datasheet values [10], evaluating accuracy of PV models[12], mathematical model of PV fields under partial shading [13] and models that calculate the power losses due to partial shading conditions [15]–[20]. On-going research is aimed to find the most efficient and cost-saving PV and converter configurations and corresponding control schemes.

This chapter will present two well-known equivalent circuit models for PV cells and their corresponding mathematical equations. The aim of this study is to compare these models in terms of accuracy and computational cost. The better model will

be used to investigate the behaviour of the PV panels under shadowing conditions, and to design the power conditioners which will improve the efficiency in this condition. The chapter will then describe the causes and consequences of the PV panels operating under partial shading. A comprehensive review on the current published systems and approaches to overcome this problem will be given. Their advantages and drawbacks will be highlighted.

2.1 Mathematic Models for PV Panels

2.1.1 Equivalent Circuit Representation and Single Diode Model

According to its operating principle [21] proposed that a single PV cell can be modelled by an equivalent circuit as shown in Figure 2.1. The main element in this circuit is a current source I_{sc} whose magnitude is directly proportional to the sun irradiance. A diode is used to represent the p-n junction of the PV cell, and its forward current I_d travels in the opposite direction to I_{sc} . A parallel resistance R_p in the circuit represents the leakage current resulting from imperfections in the silicon material, while the series resistance R_s is due to the bulk resistance of the non-depleted semiconductor regions in the diode and the connection between the cells and cables.

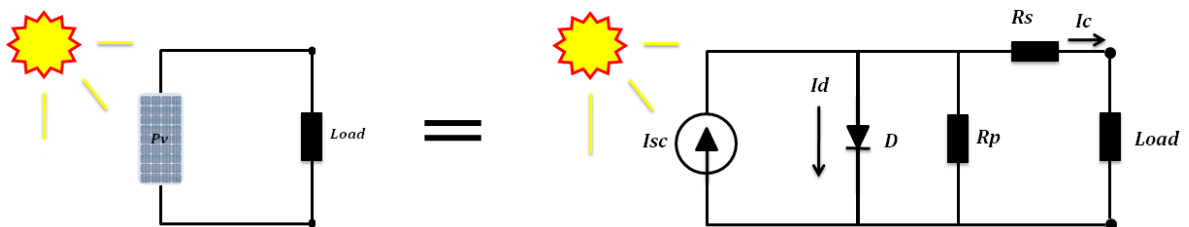


Figure 2.1 Equivalent circuit of a solar cell

In general for the ideal device, R_s is very small and R_p is large, hence the losses of the circuit would be negligible. In a real scenario the design will try to keep R_s at a minimum and R_p at a maximum. In this research the circuit will be simulated using

the ideal component values [3]. There are different equivalent circuit models such as the “double diode” model [22], [23]. However this study will be based on the single diode model.

2.1.2 Mathematical Expressions for Single-Diode Model

The mathematical expressions corresponding to each element in the circuit in Figure 2.1 are derived. There are three current branches in the circuit; I_{sc} , I_d , and I_s . The first is the photocurrent I_{sc} and its dependence on the irradiance and cell temperature can be described by the following empirical equation:

$$I_{sc} = \{I_{scr} + k_i [T_{cell} - T_r]\} \left(\frac{H}{100}\right)$$

2-1

where I_{scr} is the short-circuit current generated at T_r , which is the reference temperature in K° , the factor k_i is the temperature coefficient of the short-circuit current, and H is the irradiance in mW/cm^2 . According to the mathematical model of the Shockley diode given by [2], [23]–[25], the diode current I_d is expressed as:

$$I_d = I_o \left[e^{\left(\frac{qV_j}{AkT_{cell}}\right)} - 1 \right]$$

2-2

where I_o is the reverse saturation current (Amp), q is the electron charge ($1.602 \times 10^{-19}C$), V_j is the junction voltage (V), k is the Boltzmann’s constant ($1.381 \times 10^{-23}J/K$), T_{cell} is the cell temperature ($^\circ K$), and A the diode ideality factor [2], [6], [26], [27].

The third is leakage current I_s is given as $I_s = \frac{V_j + R_s I_c}{R_p}$.

Following the equivalent circuit representation in Figure 2.1 the equation expressing the output current, I_c of the solar cell is given as

$$I_c = I_{sc} - I_o \left[e^{\left\{\frac{q}{AkT_{cell}}(V_j + R_s I_c)\right\}} - 1 \right] - \left(\frac{V_j + R_s I_c}{R_p}\right)$$

2-3

This can be rewritten as.

$$I_c \left(1 + \frac{R_s}{R_p} \right) = I_{sc} - I_o \left[e^{\left\{ \frac{q}{AKT_{cell}} (V_j + R_s I_c) \right\}} - 1 \right] - \frac{V_d}{R_p}$$

2-4

where I_c depends on the magnitude of I_{sc} which is due to light intensity, the magnitude of I_o , and the temperature of the cell T_{cell} . The parameters of the model are affected by the atmospheric conditions, which are explained further in this chapter.

2.1.3 The Bishop Model

Another equivalent circuit model proposed by J.W. Bishop [6] is shown in Figure 2.2.

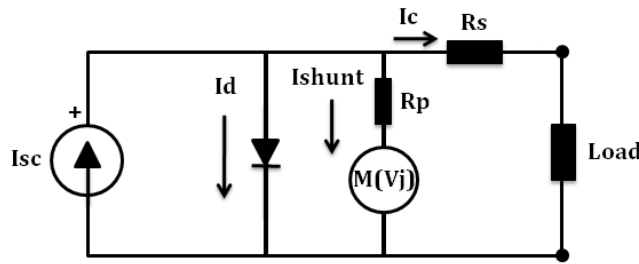


Figure 2.2 Solar cell equivalent circuit by J.W. Bishop

This also has a light and temperature dependent current source I_{sc} and a parallel diode, but the shunt branch is different from that of the previous model. This consists of a fixed resistance R_p plus a variable resistance whose value is dependent on the junction voltage V_j , which is expressed as $M(V_j)$. The shunt current I_{shunt} is thus given by:

$$I_{shunt} = \frac{V_j}{R_p} \left\{ 1 + a \left(1 - \frac{V_j}{V_{br}} \right)^{-m} \right\}$$

2-5

where V_j is the voltage across the junction (V), R_p is the fixed cell parallel or shunt resistance (Ω), V_{br} the junction breakdown voltage (V), a is the factor of ohmic

current involved in avalanche breakdown and m the avalanche breakdown exponent. This expression separates the device leakage current due to ohmic effect and that due to nonlinear overvoltage breakdown avalanche. The latter is dependent on V_j which may range from the high device breakdown voltage V_{br} to the much lower forward threshold level.

Subsequently according to the equivalent circuit in Figure 2.2 the equation for cell current is expressed as

$$I_c = I_{sc} - I_o \left[e^{\left\{ \frac{qV_j}{AkT_{cell}} \right\}} - 1 \right] - I_{shunt}$$

2-6

This model makes it possible to describe the condition where some PV cells begin to breakdown in partial shading conditions. For example when shading occurs on one cell in a series PV string, the current through the whole string is higher than that generated by the shaded cell, hence V_j of the shaded one becomes negative simulating the cell breakdown condition as shown in Figure 2.13.

2.1.4 Model Parameters

There are a number of parameters in the model important to represent the cell characteristics which are explained below.

- Photocurrent (I_{sc})

This current has been defined in Equation 2-1. Literature on the wavelength distribution [3] suggests how much energy from the sun can be absorbed by a solar cell. As pointed out in Figure 2.3, the band gap of silicon is about 1.08eV, or 2.63×10^{-19} J, and only those photons whose energy is of that magnitude or larger (i.e. with wavelengths less than 1150 nm) can create electron-hole pairs. Solar radiation contains a broad range of wavelengths. Any energy above the critical wavelength has not high enough energy to liberate electrons. Furthermore, the Air Mass of 1.5 standard spectrums for temperate latitudes is presented, taking into account the sun at an assumed angle of elevation of 42°. Defined as the AM1.5,

the atmospheric thickness should attenuate to a standard level of $1000W/m^2$ [3], [23].

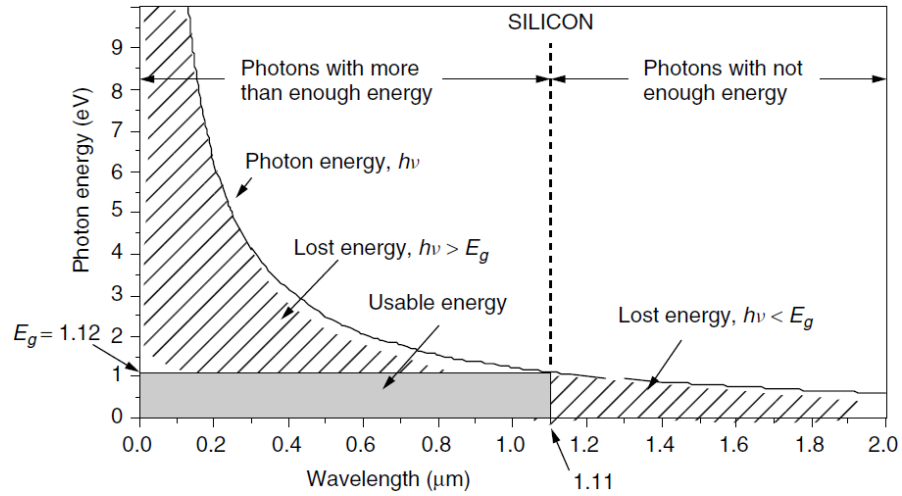


Figure 2.3 Example for silicon Photon Energy (eV) vs. Wavelength (μm) [3]

The radiant power (W/m^2) versus the wavelength in Figure 2.4 shows the solar spectrum at an air mass ratio of 1.5. The energy available for silicon is only 49.6% of the total energy. Analysis of the relationships between these factors leads to the conclusion that a cell with lower band gap will produce more current at less voltage, and vice versa. Moreover, the selection of a solar cell with the ideal band gap between 1.2 eV and 1.8 eV should be considered for optimal energy generation.

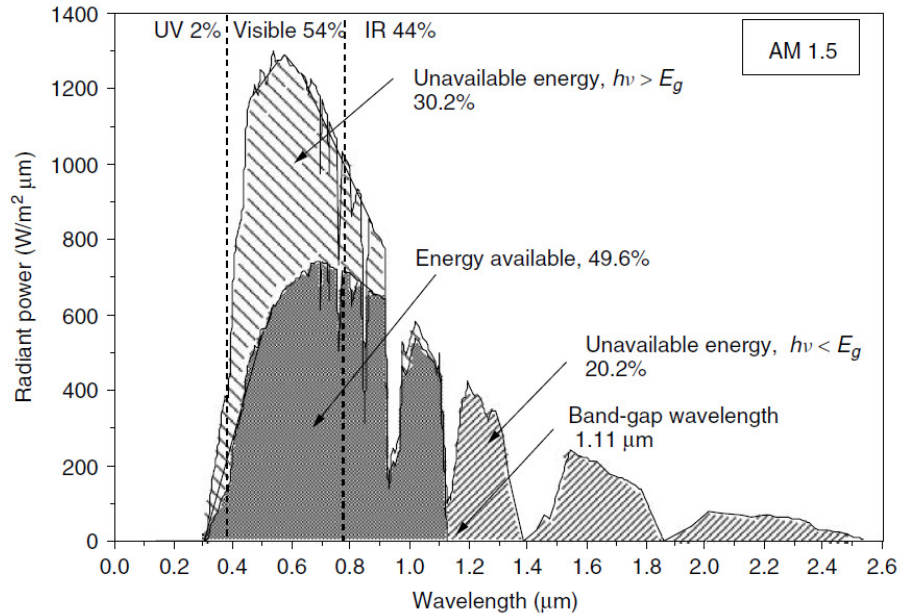


Figure 2.4 Radiation power vs. Wavelength [3]

- Reverse Saturation Current (I_o)

The temperature of the solar cell directly affects the reverse saturation current. At higher temperature, the concentration of the intrinsic charge carriers will rise giving a higher carrier recombination. Therefore, increase of temperature will raise the reverse saturation current. The current I_o [21] can be expressed by the following equation:

$$I_o = I_{or} \left(\frac{T_{cell}}{T_r} \right)^3 \exp \left\{ \frac{qE_g}{kA} \left(\frac{1}{T_r} - \frac{1}{T_{cell}} \right) \right\}$$

2-7

where I_{or} is the reverse saturation current at T_r , and E_g is the band gap.

- Cell Temperature (T_{cell})

The solar cell needs to be exposed directly to the Sun and therefore will have a different temperature from the ambient. An empirical proposed model [21] of the temperature in a solar cell provides the equation:

$$T_{cell} = 0.899 * T_{amb} + 0.25 * H - 1.3 * w_s + 30.42$$

2-8

where T_{amb} is the ambient temperature in Kelvin, and w_s is the wind speed in m/s.

- Shunt and Series Resistances

Both of these resistances are present in the equation 2-4 of the single diode model and equation 2-6 of Bishop model. The effects of these parasitic resistances on the photovoltaic material are intrinsic in the semiconductor and the physical wiring of the cells. The parallel resistor or shunt resistance R_p is caused by the leakage current due to poor insulation of the material and R_s is due to ohmic losses in the semiconductor itself as well as the wires that connect the cells [3]. Under the standard test condition (STC) of irradiation equals $100\text{mw}/\text{cm}^2$ and temperature of 25°C , R_p is very large to above $5 \times 10^5 \Omega$ and R_s is as small as $5 \times 10^{-5} \Omega$. Their effects to the PV output power are negligible. However when operating under non STC, both these resistances changes and influence the cell performance. These are investigated below.

A PV panel having 34 cells connected in series delivers the maximum power of 49 watts under full irradiance of $1000\text{W}/\text{m}^2$ at 25°C . The internal resistances are $R_p=5 \times 10^5 \Omega$ and $R_s=5 \times 10^{-5} \Omega$. When the parallel resistance R_p is reduced from $5 \times 10^5 \Omega$ to 34Ω , a significant reduction in output current occurs as shown in Figure 2.5a. Consequently the output power is reduced from 49 watts to 40 watts, namely 9 watts are consumed by the PV panel itself. Another impedance variation is introduced as illustrated in Figure 2.5b, this time the series resistance R_s increases from $5 \times 10^{-5} \Omega$ to $1 \times 10^{-3} \Omega$, causing the I-V curve slope around knee region steeper. Again this has led to a significant output power reduction from 49 watts to 39 watts. As presented in by Sera et al. in [10], practical values of these resistance at summer with temperature of 50°C can be $R_p=1,194 \Omega$ and $R_s=0.51 \times 10^{-3} \Omega$, while in winter temperature of 0° the internal resistance perform with values of $R_p=1,535 \Omega$ and $R_s=0.36 \times 10^{-3} \Omega$. According

manufacturer it has a temperature coefficient of 0.5%/°C of power degradation.

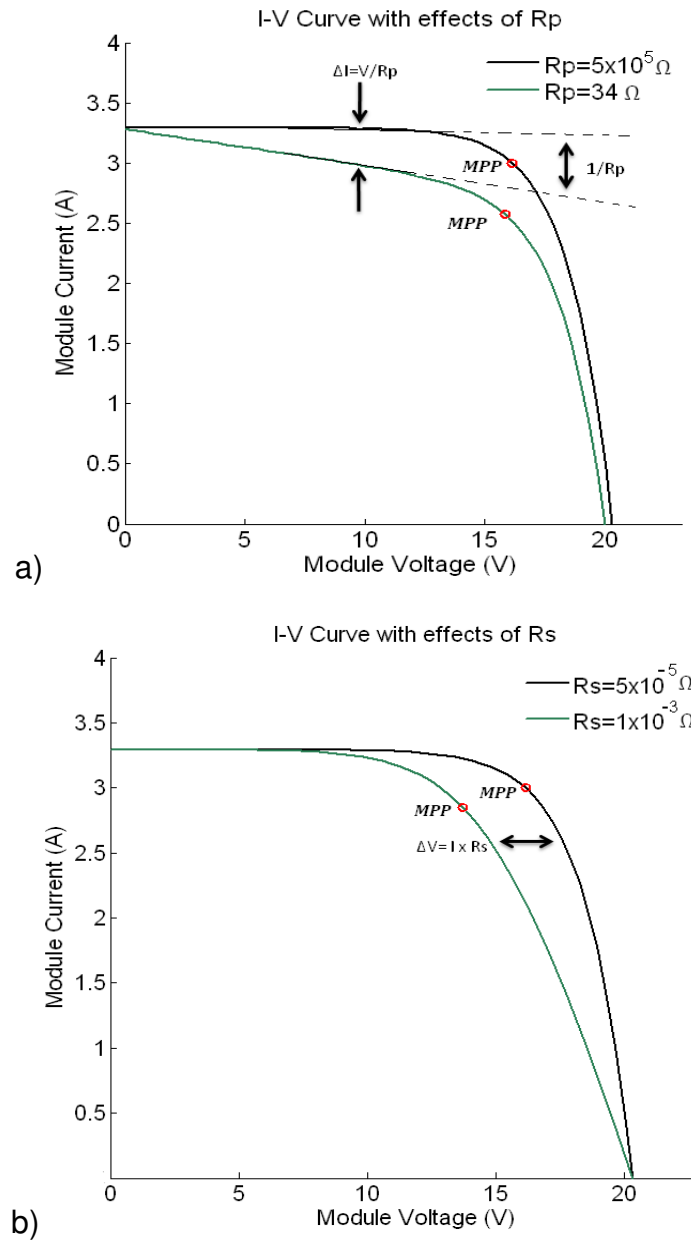


Figure 2.5 Effects of R_p and R_s over the I-V Curve

- PV Panel Configurations

Multiple solar cells are connected in series and parallel to form a PV array or a panel. The number of cells in a series string determines the voltage value a panel can generate and that connected in parallel provides the current which can be extracted from the panel (Figure 2.6) In a series configuration of N_s cells the voltage level is determined as $N_s \times 0.6$ volts, assuming the threshold voltage of each solar cell that is connected in the string is 0.6 V. On the other hand, the parallel connection of N_p such strings deliver the current level equal to $N_p \times I_c$.

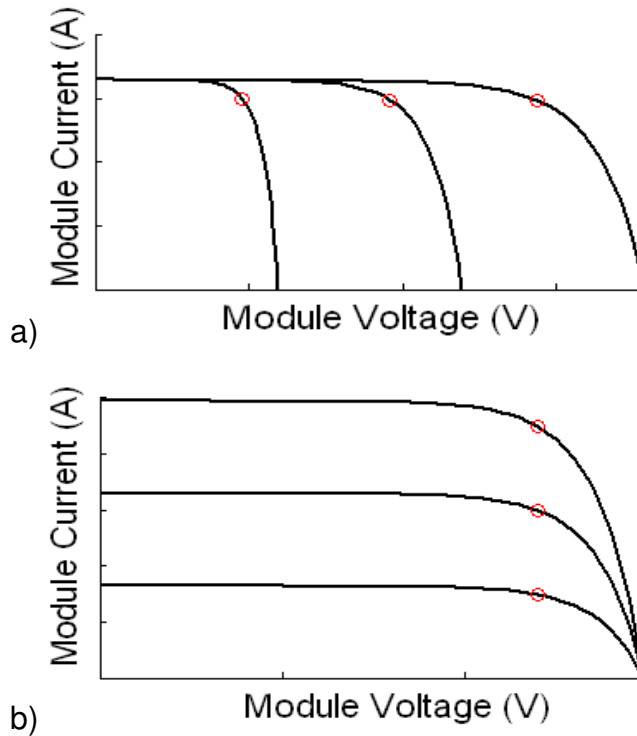


Figure 2.6 a) Solar cells in series b) Solar cells in parallel

Thus the model in equation 2-4 can be extended to represent a PV array with N_s cells connected in series and N_p cells in parallel, therefore we have

$$I_c \left(1 + \frac{R_{sT}}{R_{shT}} \right) = N_p I_{sc} - N_p I_o \left[e^{\left\{ \frac{q}{AkT_{cell}} \left(\frac{V_d}{N_s} + R_{sT} I_c \right) \right\}} - 1 \right] - \frac{V_d / N_s}{R_{shT}}$$

where the total series resistance R_{sT} is given by $R_{sT} = \frac{N_s}{N_p} \times R_s$ and total parallel resistance R_{shT} can be calculated by $R_{shT} = \frac{N_p}{N_s} \times R_p$ [21].

Similarly for Bishop model (equation 2-6) we have equation for a PV panel of multiple cells given by

$$I_c \left(1 + \frac{R_{sT}}{R_{shT}} \right) = N_p I_{sc} - N_p I_o \left[e^{\left\{ \frac{qV_j}{AkT_{cell}} \right\}} - 1 \right] - \frac{V_j}{R_{shT}} \left\{ 1 + a \left(1 - \frac{V_j}{V_{br}} \right)^{-m} \right\}$$

2-10

2.2 Numerical Methods for Photovoltaic Cell Simulation

Various computer programs have been developed to simulate photovoltaic cells including those using computer software packages such as PSPICE [10], [12], [28]–[30], PSIM [12], [31], [32], and Matlab [7], [33], This research is based on the Matlab environment, since it is considered one of the most convenient tools for solving equations.

2.2.1 The Newtown-Raphson Iterative method

Computer programs for simulating PV cells should be able to produce their I-V characteristic curves under any irradiance and temperature conditions accurately and efficiently. As already shown, model equation 2-4 expresses photovoltaic cell output current I_c . Clearly this is a non-linear equation due to the use of the exponential function for diode current. Also I_c is not expressed explicitly as a function of terminal voltage V_t . Assuming V_t is initially given; the evaluation of I_c should therefore be solved by an iterative process. For this the Newton-Raphson method was selected, for its simplicity and speed of convergence [10], [22], [24], [25], [34]–[36].

The algorithm is implemented by, firstly, expressing equation 2-4 for the PV cell current as

$$f(I_c) = I_c \left(1 + \frac{R_s}{R_p} \right) - I_{sc} + I_o \left[e^{\left\{ \frac{q}{AkT_{cell}} (V_j + R_s I_c) \right\}} - 1 \right] + \frac{V_d}{R_p}$$

2-11

and its derivative $f'(I_c)$ are formulated as

$$f'(I_c) = 1 + \frac{R_s}{R_p} + \frac{qR_s}{AkT_{cell}} I_o \left[e^{\left\{ \frac{q}{AkT_{cell}} (V_j + R_s I_c) \right\}} - 1 \right]$$

2-12

According to the Newton-Raphson algorithm, the current I_c corresponding to any valid terminal voltage value can be obtained iteratively by

$$I_c(n+1) = I_c(n) - \frac{f(I_c(n))}{f'(I_c(n))}$$

2-13

The method starts with an initial estimate of the root $I_c(0)$ and produces successive approximated roots $I_c(1)$, $I_c(2)$, $I_c(n)$, $I_c(n+1)$, ... using equation 2-13. This algorithm relies on the initial estimated root value being sufficiently close to the solution; the next value generated from the previous one would be closer to the solution and the algorithm terminates when successive estimates are close enough according to a defined accuracy. In practice this process takes from 2 to 4 cycles to yield an acceptable accuracy in the estimated I_c for each voltage value. The method has been shown to be reliable when the starting value is set close enough to the final solution. In addition to avoid falling into non-convergent iteration, a maximum number of loops can be set to terminate the iteration. Figure 2.7 shows the I-V and P-V characteristic curves produced by the above described simulation method for a single PV cell with parameters given in Table 2-1.

Parameter	Value
Ambient Temperature (Celsius)	20
Solar insolation (mW/cm ²)	1000
Cell short circuit current (Amps)	3.3
Open Circuit Voltage (Volts)	0.6
Number of Series Cells	1
Number of Parallel Cells	1

Table 2-1 Single solar cell parameters

The main drawback of this method is the high computational cost. For each chosen output voltage, the iterative method required for estimating its corresponding current value is tedious and inefficient. The situation is exacerbated when dealing with a PV plant consisting of multiple PV panels, and each is under different light and temperature levels. The fact that this algorithm requires at least 2 to 4 iterations to define one operating point of one PV panel may make the simulation process too long to be practical.

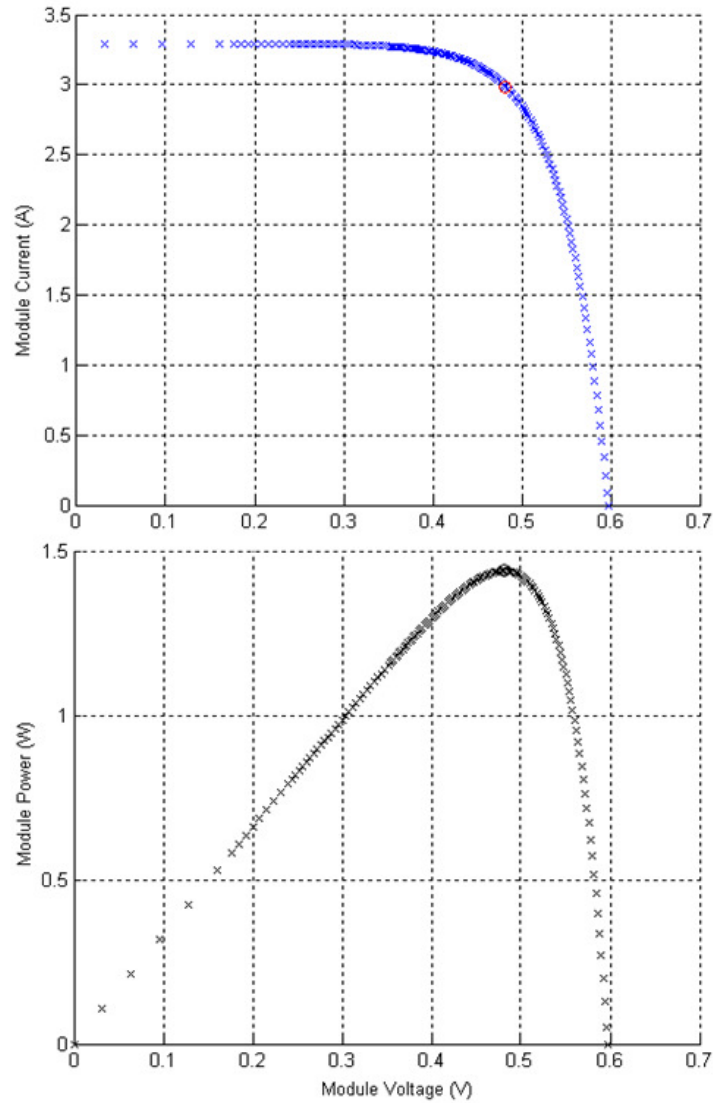


Figure 2.7 I-V and P-V Characteristic curve obtained by iterative process

2.2.2 Bishop's proposed model

With the model equation 2-3, Bishop proposed a method which avoids iteration. Instead of starting from the PV cell/panel terminal voltage, V_t . The method recognises that the cell junction voltage $V_j = V_t + R_s \times I_c$ and it determines directly the diode leakage and shunt currents, and hence the cell terminal current I_c , without any iteration process. This simplifies the computational process and hence shortens the computing time. V_j can be set corresponding to any specific set of sun

radiation and temperature values. For simulating a complete I-V characteristic curve of a PV cell the procedure below is followed:

1. Set V_j in equation 2-5 initially as the value of V_{br} ,
2. Calculate the value of I_{shunt} using equation 2-5,
3. Calculate diode current I_{sc} and I_d , using 2-1 and 2-2,
4. Calculate the total output current I_c using equation 2-6,
5. Evaluate value of terminal voltage $V_t = V_j - R_s \times I_c$
6. Increase V_j by a small value ΔV_j , and repeat the procedure from 2 above
7. Stop until V_j is above the threshold level and estimated I_c is near 0 Amp.

Using the above described procedure the I-V characteristic curve for a typical PV cell is computed as shown in Figure 2.8. The cell parameters are given in Table 2-1.

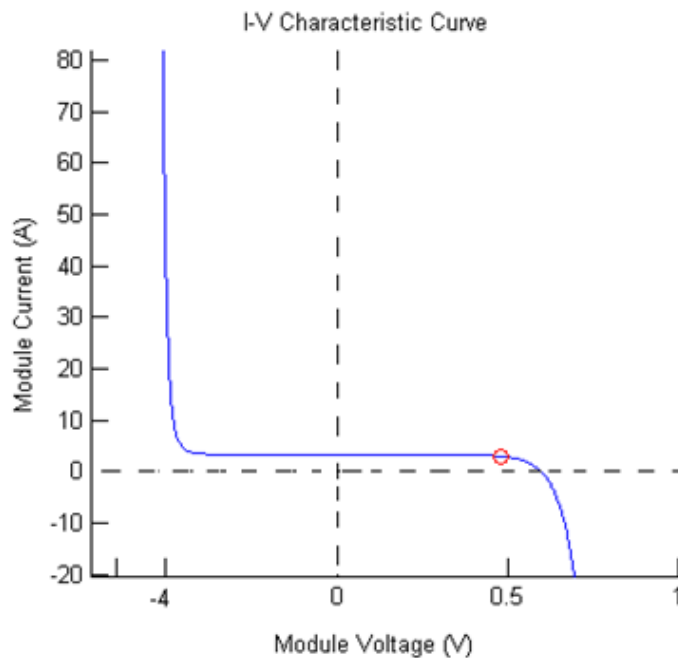


Figure 2.8 I-V characteristic curve with Bishop's equations

Figure 2.9 shows I-V and P-V characteristic curves of the same cell when the starting value for $V_j = 0V$, and the endpoint is when $I_c = 0A$. Comparing these curves in Figure 2.9 with those in Figure 2.7, there are little differences in shape and values, the peak power values differ only a negligible 0.001 Watts.

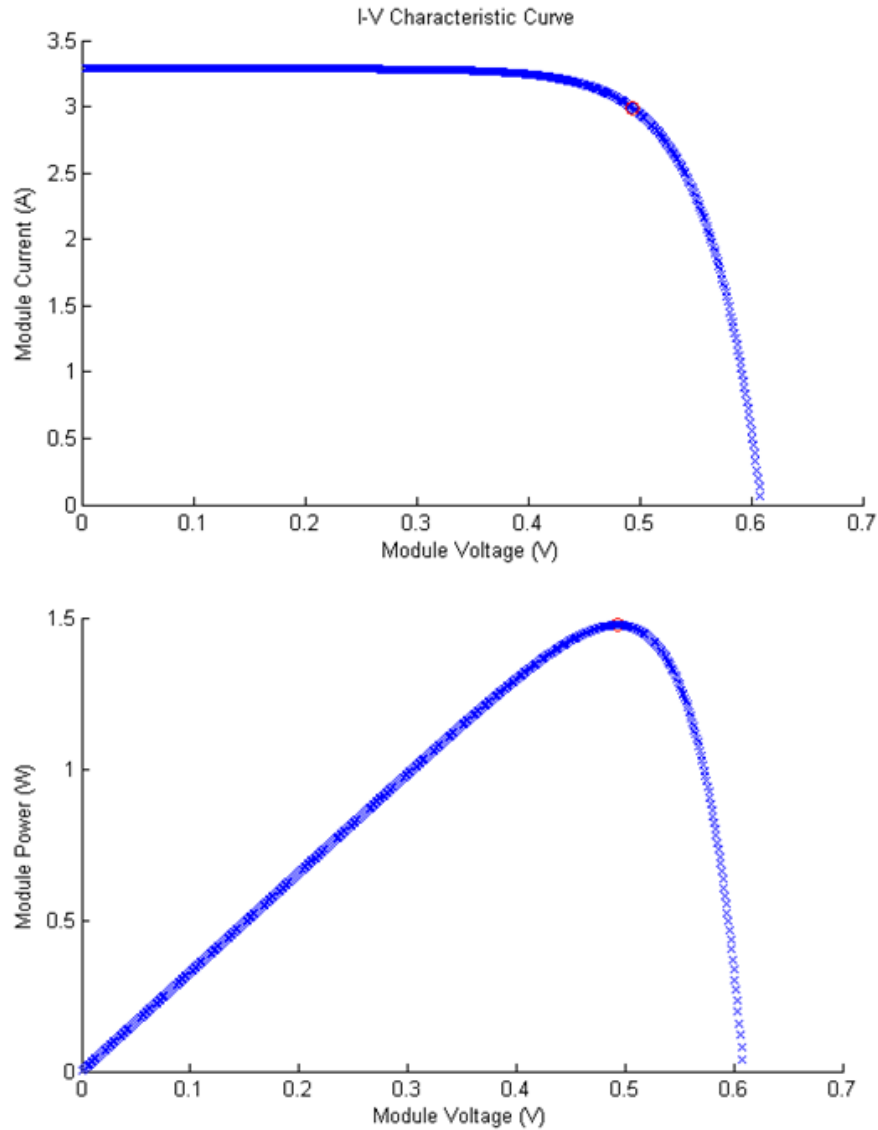


Figure 2.9 I-V and P-V Characteristic curve obtained by Bishop Model

2.3 PV Panels under Partial Shading Conditions

2.3.1 Effects of Light and Temperature to PV panel output power

The level of Light Irradiance “ H ” in mW/cm^2 or “ G ” in percentage of irradiation (representing in laboratory conditions $100\% = 367\text{mW}/\text{cm}^2$), plays the main role in photovoltaic power output and it can be considered linearly related to the short circuit current I_{sc} . The average power produced by a PV panel depends greatly on the average intensity of sunlight available throughout the day. Both the voltage and current at the maximum power operational point decrease when at lower irradiance levels as shown in Figure 2.10.

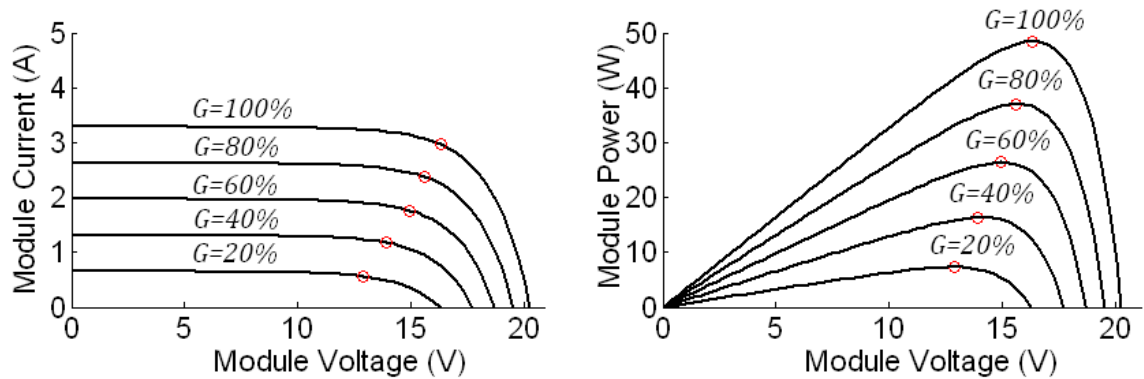


Figure 2.10 PV curve simulation with different sunlight proportion

The temperature of the PV panel also affects the power harnessed from it. Figure 2.11 shows the example of a PV panel simulation at the same irradiance level; from low to high temperatures the short circuit current varies only slightly whereas the open circuit voltage decreases markedly at higher temperatures, as does the power available from the panel.

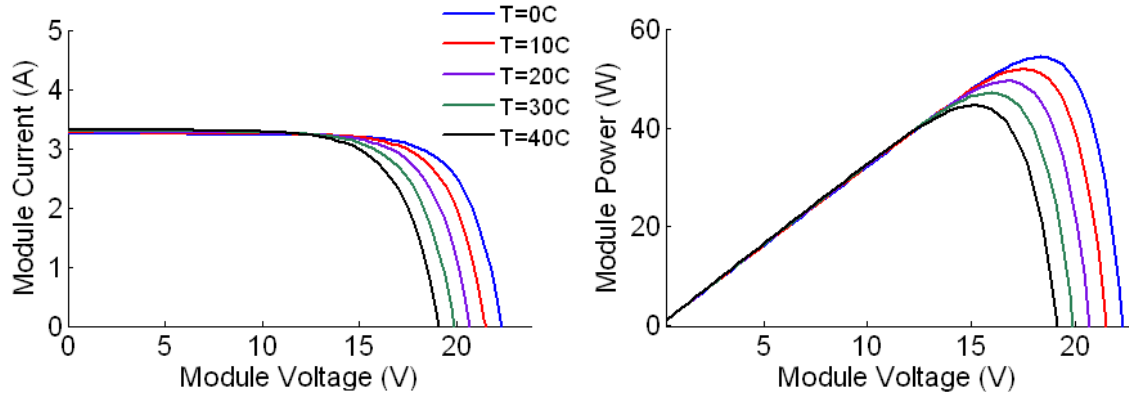


Figure 2.11 PV curve simulation with different temperature

2.3.2 Causes and Consequences of Partial Shading

It is well known that PV cells connected in a series chain should match well in their features. This is due to that operating points of cells are set by the load across the string, and a series string forces all cells passing the same current. Slight difference in cell characteristics leads to cells operating at different voltage points. This variation of operating points introduces losses, reducing panel performance. The level of solar irradiation striking on a PV panel may not be equal across the panel surface due to disturbance caused by clouds, physical objects such as, trees, leaves, birds, or dust. Shadows on a section of a panel causes mismatch characteristics of the PV cells and a disproportionate reduction of the power that the panel can actually harvest. Figure 2.12 displays the problem of a single solar cell being shaded in a PV chain (shown on the right-hand-side) compared to that with uniform light condition (on the left-hand-side).

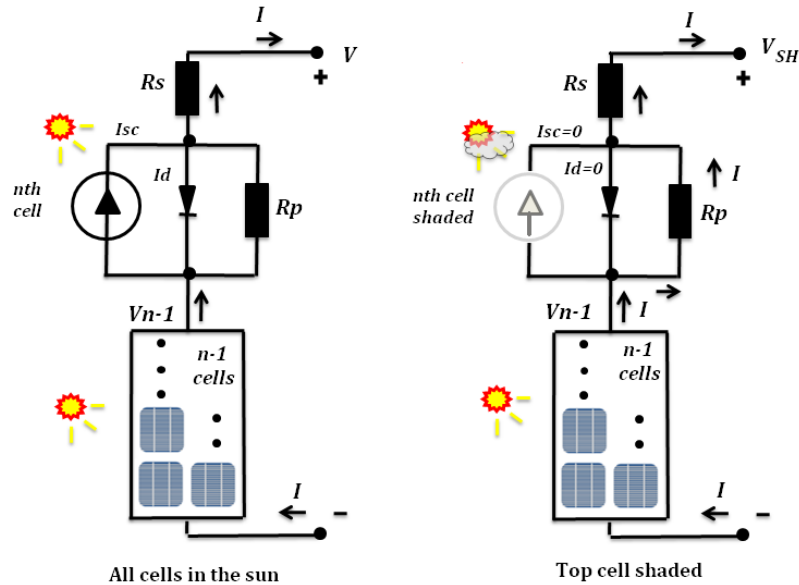


Figure 2.12 Comparison of string of cells in full sun and in partial shading

Since the current produced by a solar cell is proportional to the irradiation captured by it, the generated power from the right-hand-side string could be at a lower level than that at the left-hand-side one.

The shadow causes a significant mismatching than inherent cell/panel characteristic differences. The load current flowing through the string may exceed the short-circuit current of shaded cells, forcing them becoming reverse biased. The power dissipated in these cells then increases and may lead to panel 'hotspots'. This can be illustrated by the following example.

A PV module with 36 cells, and 35 of them are under uniform irradiation of 1000W/m^2 , operating at P_1 , but one is shaded with irradiance reduced to 400W/m^2 . If the current through all cells follows the short circuit current of the shaded cell, shown in Figure 2.12, the total voltage V_t of the fully irradiated cells and the shaded cell is

$$V_t = V_{SH}(I) + [35 * V_f(I)] ,$$

where $V_f(I)$ and $V_{SH}(I)$ are respectively the voltage of fully irradiated cells and that of the shaded one.

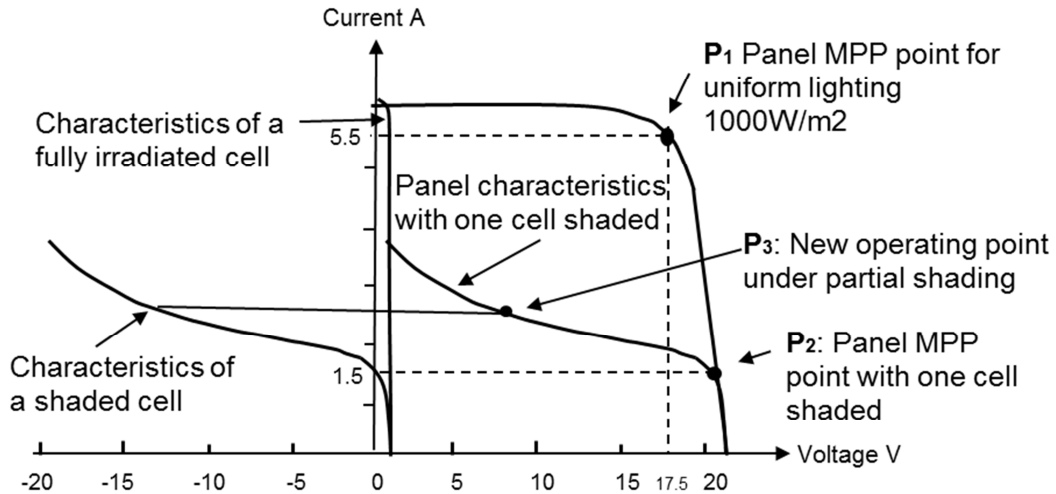


Figure 2.13 Example of a PV panel under partial shading

Clearly the maximum panel power decreases significantly from P_1 to P_2 , though only one cell out of 36 is inactive. On the other hand, the panel may operate at high current at point P_3 in Figure 2.13. Increasing the current leads to the shaded cell having negative (reverse) voltage, so it becomes a load. The output power from the panel is now near zero, as it is consumed by the shaded cell. This dissipation of power can cause damages in the cell material, as well as the module encapsulation. Using the equivalent circuit model to analyse the situation, the equivalent diode in the shaded cell is in reverse bias, so the current must flow through the resistance R_p and R_s . The large value of R_p will transform it into the principal consumer of power produced in the string. The effect may lead to physical damage of this cell which is known as a “hotspot” [37], [38].

2.3.3 The use of Bypass Diode for Partial Shading

To solve the problem of partial shading, bypass diodes are integrated in parallel to the modules, usually with 18-24 cells per diode. The bypass diode switches as soon as a small negative voltage of about $-0.7V$ is applied, depending on the type of diode. This negative voltage occurs if the voltage of the shaded cell is equal to the sum of the voltage of the irradiated cells plus that of the bypass diode.

An example of 2 solar cells connected in series, each wired in parallel with a bypass diode and the system connected to the load is as shown in Figure 2.14, the first solar cell from the top can be considered as being irradiated by the light of the sun at 100%, whereas the second one is lit at a variable light levels generating a partial shading condition in the system. The I-V and P-V characteristic curves of two panel system with bypass diode are shown in Figure 2.15. The shaded string will produce the amount of power just in proportional to the light levels, causing a step down shape in the characteristic curve.

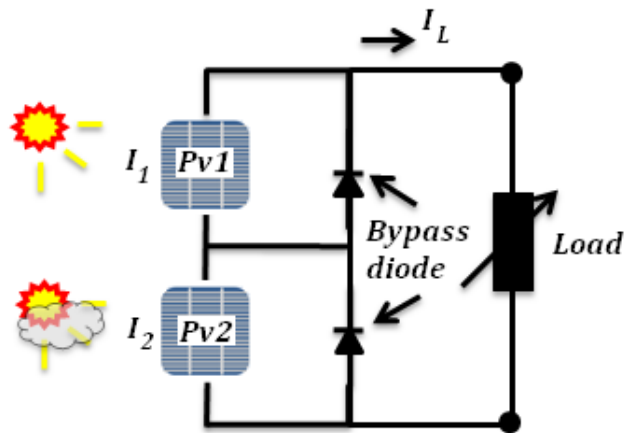


Figure 2.14 Two solar cells + diode connected in series under partial shading

The use of the bypass diode is the simplest but not the most efficient solution due to the loss of the capability of harvesting energy from the shaded PV Panel. When a shadow is cast over a panel, its associated bypass diode will conduct, therefore, bypassing the current flowing through it. This effectively protects the shaded panel, however, prevents it from generating any power.

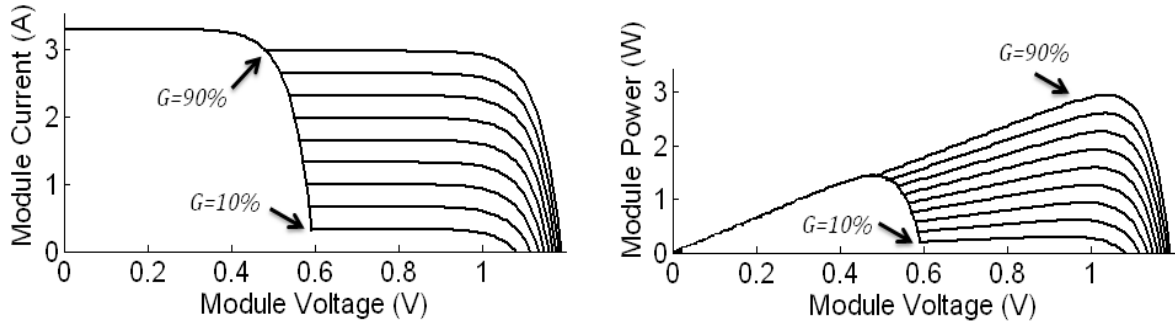


Figure 2.15 I-V curve with bypass diodes under different irradiance level

2.4 Analysis of a photovoltaic panel for experimental setup

To study the practical effect of partial shading, developing new PV panel + converter system configurations and control schemes, practical solar laboratory has been set up in the School of Electronic and Electrical Engineering, at the University of Leeds.

One of the most important equipment in this lab is the controllable artificial sunlight emulator. The main component of this, provided by “Showtec Sunstrip” [39], consists of 4 light bars, each bar is fitted with ten MR16, 12V/75W halogen lamps. The power supply for these light bars is controlled by a 6 channel DMX Dimmer Pack which can adjust the load voltages linearly, emulating different sun irradiation levels. Three sunlight emulators are installed to light three identical PV modules called Sunsei SE-6000 PV modules [40] which can be connected either in series or parallel. A picture of them with controllable solar simulators is shown in Figure 2.16.

In addition to having sunlight emulators, the temperature of the PV modules must be controllable, so a ventilation system is installed in the lab around the PV panels and light emulators. This enables adjusting the temperature of the PV modules in a wide range from 25°C to 70°C, simulating different combinations of light and

temperature levels. It also helps to dissipate the heat generated by the sunlight emulator due to the number of lamps concentrated in this installation.



Figure 2.16 Solar Setup

2.4.1 I-V Characteristic Curves of the PV panels

To obtain the I-V curves the Sunsei PV panel mentioned above is connected in series to a variable resistor functioning as the load of the system as shown in Figure 2.17. Various weather conditions are set; i.e. the light irradiancies are 30%, 60% and 100% for temperatures of 25°C and 40°C respectively. The load resistor is adjusted from $R_L \approx 0\Omega$ which is the starting point of the I-V curve labelled as short circuit current " I_{sc} " and increased until the current given by the PV panel equals zero, hence reaching the point of "Open circuit voltage". Two sets of I-V curves for two different temperature values (25°C and 40°C) each having three light levels as 30%, 60% and 100% are shown in Figure 2.19. As expected, these curves show clearly that the short circuit current increases as irradiation level becomes higher. Also for the same light levels when temperature is higher the open circuit voltage reduces, hence the power generated is lower.

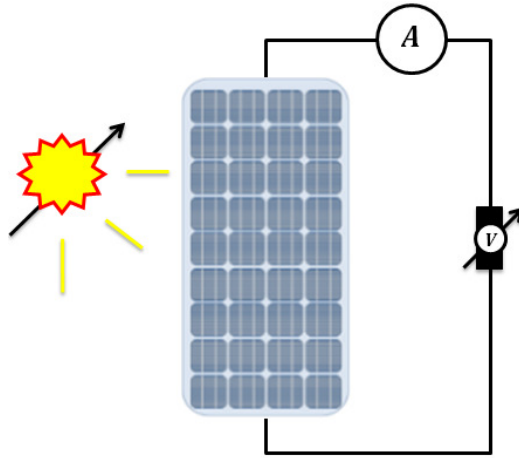
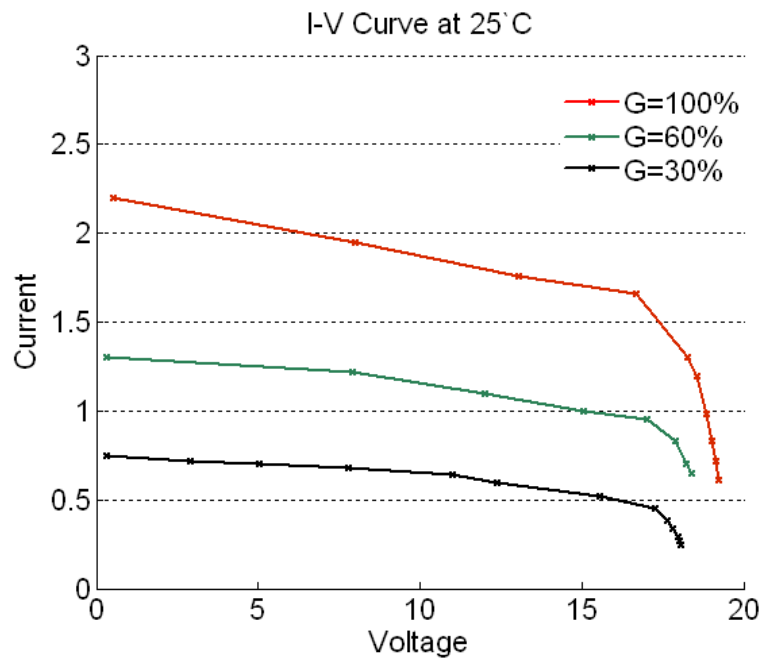


Figure 2.17 PV connection to extract the I-V Curve



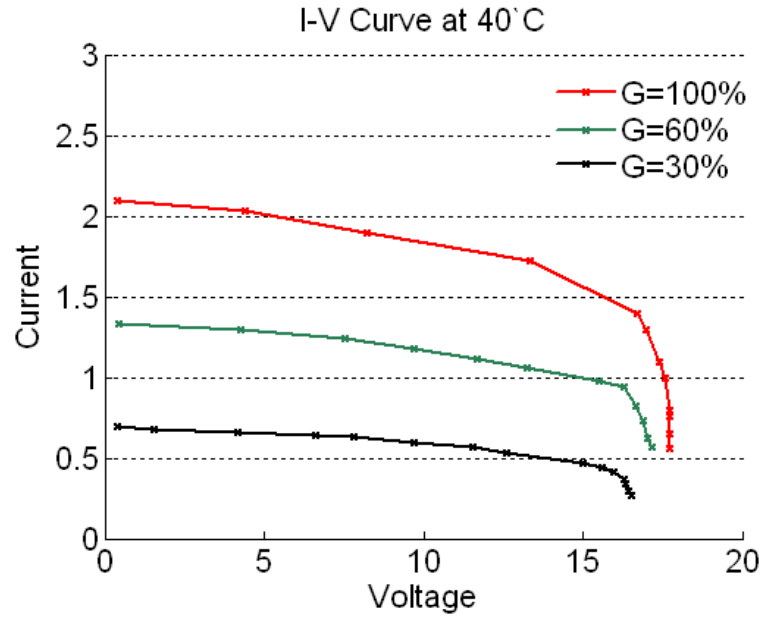


Figure 2.18 IV Curve from the PV installation

2.4.2 Typical I-V and P-V characteristics of PV panels under partial shading

As been discussed in Section 2.3.2 under the partial shading conditions, the I-V and P-V curves for “n” serially connected PV panels could be divided into “n” number of local maximum power points. As shown in Figure 2.19, this is the P-V curve for two panel unit which shows the local and a global maximum power point. Measurement of the P-V curves for three PV panel wired in series under uneven light levels has been carried out.

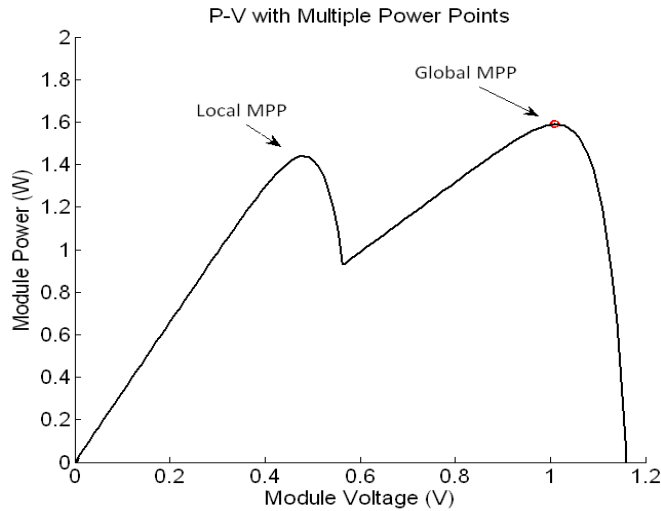


Figure 2.19 Local and Global MPP

2.4.3 Three PV panels under partial shading conditions with Bypass Diode

The three PV modules are the ones given previously and are chained in series, they all equipped with a bypass diode. Three sunlight emulators were used. The specific light levels set for the test were such that the intensity on PV_1 varies in steps of 30% while that on PV_2 is irradiated at 30% while PV_3 is maintained 100%, these different cases are listed in Table 2-2. Note in this test the 100% light level corresponds to 505 mW/cm^2 solar irradiation power. This is necessary to reduce the heat generated from the three fully operating emulators which generate considerable heat causing significant ambient temperature increase.

Case	G_1	G_2	G_3
1	100%	30%	100%
2	70%	30%	100%
3	40%	30%	100%
4	20%	30%	100%

Table 2-2 Different irradiance cases

The P-V characteristic curves for all these lighting conditions are grouped in a set of four and are plotted in the diagram shown in Figure 2.20. As can be seen nearly all curves have three local peak power points, except the ones giving the highest output power for the conditions that two of the three light levels are the same. The challenges for these operating conditions are to control the output load such that the maximum power generation can be obtained which are the aims of this work.

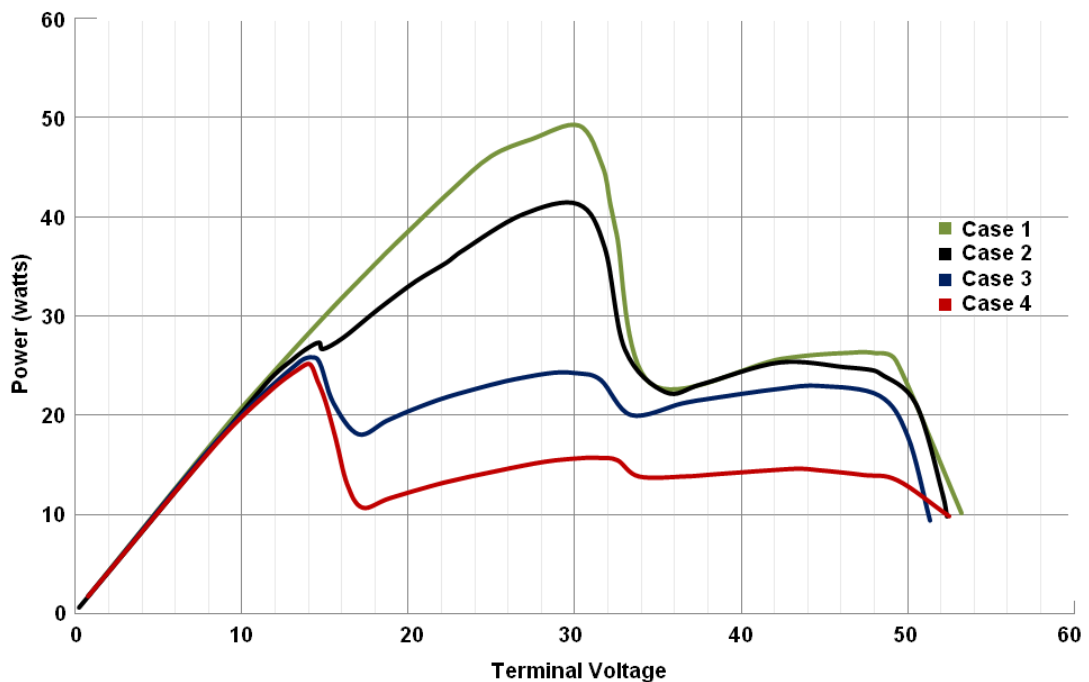


Figure 2.20 Bypass diode + three PV panels under uneven irradiance

2.5 Integrated Converter PV Unit for Partial Shading

Solutions for overcoming partial shading issues have been investigated by many researchers in recent years [41]–[44]. The use of converters avoids the creation of multiple local power points which are created by the Bypass Diode [30]. The electrical architectures used to harness the power from the solar modules may vary depending on the end user. Since PV installations can be present in a standard house or a “Photovoltaic Farm”, these plants are divided by Centralized and

Distributed [45]. The evolution to a balanced segmentation of these two markets has been present since 2012 (Figure 2.21). Distributed installation changed in a faster rate with several countries deciding to discontinue the support for utility-scale PV in Europe; nevertheless the Photovoltaic installations maintain the exponential growth over the past years [1].

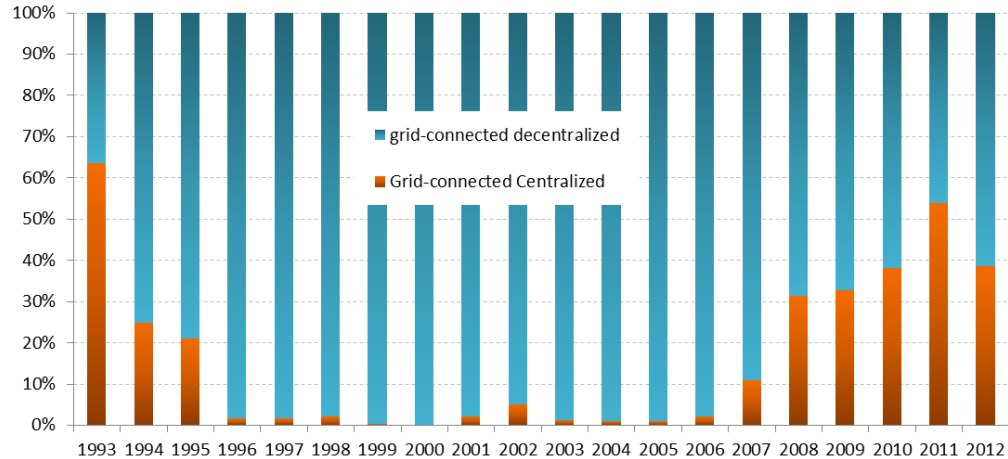


Figure 2.21 Evolution of Grid connected PV Market Segmentation [1]

The Power Conversion architectures have evolved from a Central configuration to a Multi-string configuration over the years, these can be listed as:

- Central Inverters

The Central inverters indicated in Figure 2.22(a) use one converter with multiple outputs and different voltage values and load regulation levels by each bus line. PV modules are distributed in string connections, each one generating enough voltage to evade further amplification. The principal advantage of this configuration is the concentration of all the process in one inverter. Nevertheless, intrinsic drawbacks are presented such as the need of high voltage DC cables to wire the solar

modules and the inverter, power losses to common MPPT techniques and module mismatch, representing a limitation of adaptation to new technologies [42].

- String Inverters

The string inverters presented in Figure 2.22(b) are just a simplified version of the central inverters dividing each string and inverter into one phase connection. This configuration, as well as the Central, needs enough level of voltage to avoid amplification. The major advantage over the central inverter is that now each string has an individual MPPT. However, the maximum power point is oriented for all the string and not to the individual PV panel [41].

- Multi-String Inverters & Module Integrated Inverters

Multi-string inverter Figure 2.22(c) is a further derivation of the String Inverter where uses multiple converters away from the load in such configuration that voltage and current levels can be combined to satisfy the load requirements. Although the combinations can be rated for high voltage solutions, the strings can implement low power algorithms to find the maximum power point. Each string is connected to a dc/ac converter and further connected to an inverter. Since each string is independent of each other, individual controls are applied to the strings. Further enlargements can be achieved since new dc/dc strings are just connected to the existing inverter. By the other hand, the module oriented configuration gives the case where a PV panel is directly connected to an inverter, eliminating any high voltage DC wiring. Although, this as a simple solution, the main challenge for the designer is to develop an inverter capable to amplify low voltages to an appropriated level for the grid and maintain a high efficiency [41].

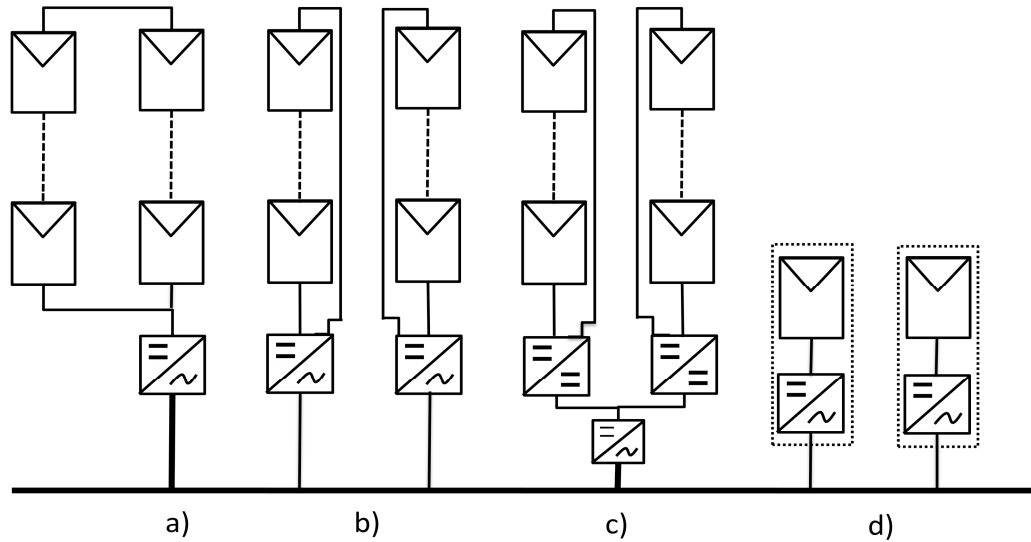


Figure 2.22 Overview of PV Inverters (a) Central Inverter, (b)String Inverter, (c)Multi-string Inverter, (d)Module Integrated Inverters

In recent years, a new configuration presented by Walker et al. in [44] introduces the Bypass dc-dc Module Integrated Converter configuration where bidirectional converters are connected as in Figure 2.23. The converter wiring configuration is referred as “bypass” in each pair of PV panels, allowing achieve the individual maximum power point and monitoring. The bypass configuration acts as power optimizer of each PV module since is directly connected with the DC/DC converter, contrary to the case where PV strings are connected in series to the central inverter. The bypass configuration aids the solar module to achieve a global maximum power point avoiding the lower local power points produced in a PV installation by partial shading conditions. Since Central inverters are already deeply introduced in the market, the bypass converter can be helpful in PV installations that wish to improve the power production.

A thorough analysis and explanation of this configuration will be given in the following chapters since this report will be concentrated in the “bypass” configuration of power conversion.

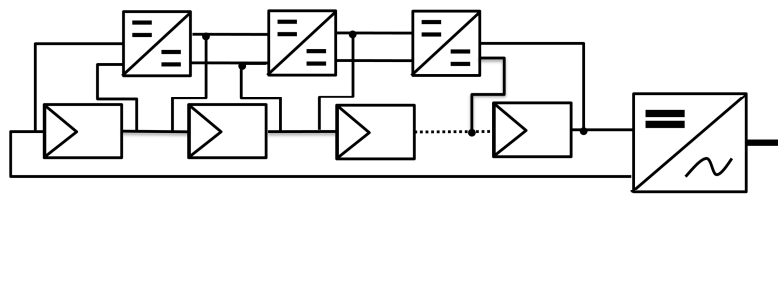


Figure 2.23 Bypass dc-dc Module Integrated Converter

2.6 Summary

This chapter presents the modelling of photovoltaic cell and panels. A comparison of two different models has been done with the purpose to optimize computerized simulation of photovoltaic systems. Bishop's PV model is chosen to compute each point of current and voltage of the IV characteristic curve. Analysis of the photovoltaic model shows the direct dependency of atmospheric conditions.

The chapter also described the operating condition of uneven light level on a PV system consisting of multiple panels/modules connected in series. The bypass diode is used as a simple solution of the partial shading. However, the disadvantages of this approach lie in the appearance of multiple power peaks in the P-V curve, creating the necessity of exploring other solutions for the "partial shading" issue.

The chapter reviewed the current development in PV + converter topologies for overcoming partial shading problems. In addition experimental tests and results on PV modules under partial shading conditions have been presented.

Chapter 3

Analysis of the Bidirectional Ćuk Converter as a PV Converter

The well-known DC-DC converters such as buck and boost converters are power electronic circuits composed of only a few components and have been used in photovoltaic generation systems. Many other converter topologies have been proposed over the past decades [37], [43], [46]–[55], even though most of them are the combinations of the two basic circuits; the buck converter [50], [56] which converts the input voltage to a lower output voltage and the boost converter [35], [57], capable of achieving an output voltage higher than the input.

An example of these combinations is the buck-boost converter which combines the features of both topologies [35], [50], [57]–[59] of stepping down (for $K < 0.5$) and stepping up (for $K > 0.5$) of the input voltage. However, there are drawbacks in their designs which can be mentioned as follows. The buck converter presents a pulsating input current, while the boost converter has a pulsating output current which is responsible for a high output voltage ripple. Therefore the buck-boost topology, being a combination of these two, has pulsating current at both input and output ends [48], [60].

The Ćuk converter, first introduced by Slobodan Ćuk [48], was developed to serve as an improved solution to the above. Having the advantages of the basic boost and buck converters such as the flexibility in step-up/step-down the voltage, but without the shortcomings of producing high current ripples, this topology has been adapted by many researchers [5], [28], [29], [35], [37], [42], [43], [47], [61]–[90]. This chapter presents a thorough investigation of the Ćuk converter and its dynamical behaviour. Moreover, the integration of this converter with photovoltaic

panels makes it essential for it to work with the fluctuating voltage or current levels imposed on a PV installation by atmospheric conditions and shading effects. The topology is thus analysed as a photovoltaic converter.

3.1 Ćuk Converter Circuit

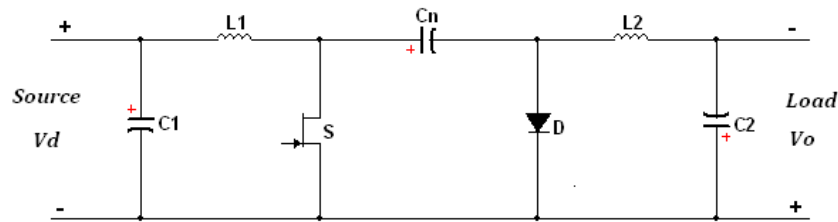


Figure 3.1 Basic Ćuk Converter

The basic circuit of a Ćuk converter [48], [91], as shown in Figure 3.1, was developed to give a simple structure but offers the optimal harmonic performance at both input and output terminals. It is composed mainly of two Inductors denoted L_1 , L_2 , a switch S , a diode D and the energy transfer capacitor. C_n It is, in fact, the combination of a boost converter as the input and a buck converter as the output connected in cascade, avoiding the pulsating currents mentioned before. Additionally, filtering capacitors can be added in shunt at the input and output terminals to reduce voltage ripples due to switching.

Capacitor C_n is the main element in this circuit for storing and transferring energy from the input source to the output load. From the circuit diagram it is clear that at the steady state, since mean voltages across both input and output inductors are zero, $V_{C_n} = V_d + V_o$ namely V_{C_n} is greater than both input and output voltages. Also the polarities between input and output terminals are reversed.

3.2 Operation Principle

3.2.1 Circuit Analysis

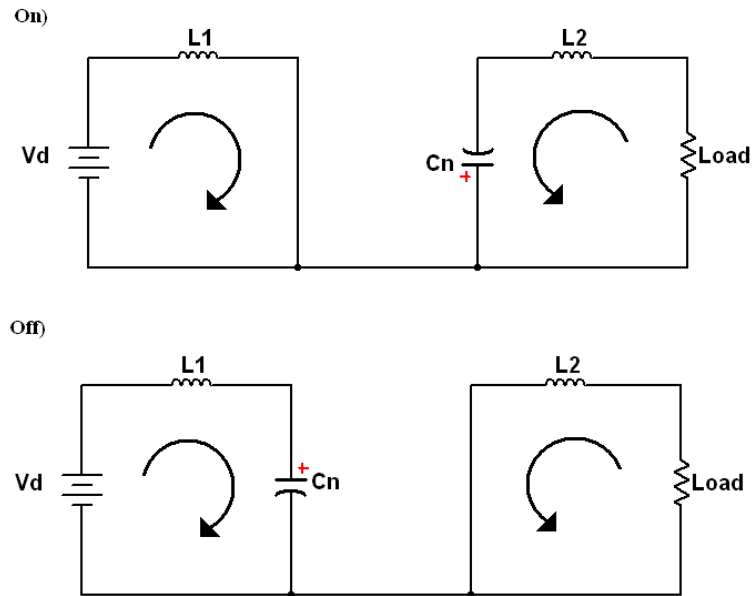


Figure 3.2 Switching On-State and Off-State of the Ćuk converter

The circuit configurations for both the on and off states of the switch are shown in Figure 3.2. In the on-state, the input voltage is applied directly across the inductor L_1 which is being charged, also the converter input current I_{L_1} increases. On the other hand the capacitor voltage V_{C_n} , having the polarity as shown in the diagram, its positive end is connected to the negative of the input voltage source hence reverse biases the diode and can only form the circuit with the output terminal. Since V_{C_n} is greater than the load output voltage V_O , C_n discharges its stored energy (charged during switching on-state) to the load and L_2 through the switch. Inductor current, also the load current, I_{L_2} increases. The waveforms of I_{L_1} , I_{L_2} and the voltage across them during switching on-state are shown in Figure 3.3(a).

On the other hand, at off-state, the capacitor C_n is switched over to the input source V_d side through L_1 and forward biased diode, so it is charged through the diode by energy from both input source and that stored in L_1 . Since $V_{Cn} > V_d$, the capacitor charging current, also the input current, I_{L1} decreases as displayed in Figure 3.3(a). Meanwhile at the output side inductor L_2 discharges its stored energy (during switching on-state) to the load, so current I_{L2} also decreases as shown in Figure 3.3(a). Note the waveforms shown in Figure 3.3(b) are the current through and voltage across C_n with the assumption that the currents I_{L1} and I_{L2} are ripple free.

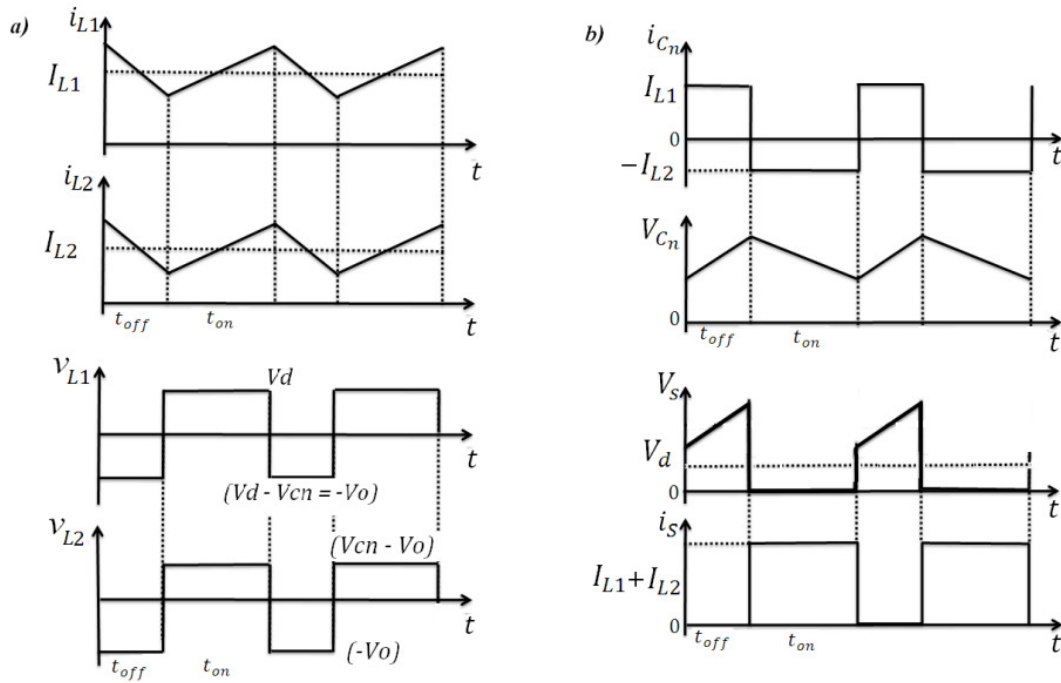


Figure 3.3 Ćuk converter waveforms at On/Off State a) inductor currents and voltages, b) C_n current and voltage, Switch voltage and current.

At the steady state, denoting switching period as T_s and switch duty ratio k , the charges delivered cycle to the capacitor C_n during switching off-state is equal to $I_{L1}(1 - K)T_s$. However, during the on-state the charges in capacitor C_n is drained

by $I_{L2}KT_s$. Since in a lossless converter the net flow of charge into the capacitor must be zero, and hence the relationship between the inductor currents is:

$$I_{L1}(1 - K)T_s + (-I_{L2})KT_s = 0$$

3-1

So

$$\left| \frac{I_{L2}}{I_{L1}} \right| = \left| \frac{I_o}{I_d} \right| = \frac{1 - K}{K}$$

3-2

So, for an ideal converter the power relationship will be $P_o = V_d I_{L1} = -V_o I_{L2} = P_d$, so we have the voltage ratio given by

$$\left| \frac{V_o}{V_d} \right| = \frac{K}{1 - K}$$

3-3

An alternative way to derive the same relationship is through voltage analysis. In the steady state, the mean voltage across either inductor must be zero. Since C_n is large the voltage V_{C_n} can be assumed constant, so we have the average voltage across the inductor L_1 over one complete cycle given as:

$$V_d KT_s + (V_d - V_{C_n})(1 - K)T_s = 0$$

This leads to

$$V_{C_n} = \frac{1}{1 - K} V_d$$

Similarly that for L_2 is

$$(V_{C_n} - V_o)KT_s + (-V_o)(1 - K)T_s = 0$$

So we have

$$V_{C_n} = \frac{1}{K} V_o$$

Equating the above two equations gives the same voltage relationship as Eq 3-3

3.2.2 Analysis of Components Selection in a Photovoltaic Converter

Considering for the moment only steady state operation, selection of component values can be based on considerations of the magnitudes of the ripples in the inductor currents, in the voltage across the energy transfer capacitor C_n , and that in the voltage ripples at the source and load ends. The latter are determined by the additional filter capacitors fitted at the both terminals. The rated values of the input and output voltages, currents and the switching frequency are assumed to be known for a determinate application, and hence it is possible to calculate the maximum acceptable ripple in any current or voltage.

Output Filter:

For the output inductor L_2 [35], at switch off-state we have

$$L_2 = \frac{V_o (1 - K)}{\Delta i_{L_2} f}$$

3-4

where Δi_{L_2} is the peak-to-peak variation in the current flowing through the output inductor and f is the switching frequency. This equation contains only the change in inductor current during the on state caused by the mean values of the transfer capacitor voltage and the load voltage. Both of these voltages have fluctuations which are assumed to be small compared to their mean values, and hence are neglected in the above equation.

Now consider the load voltage fluctuation, which is caused by the fluctuation of the inductor current flows through the output filter capacitor. Between the on and off states, the filter capacitor is charged and discharged, and the changes of charge Δq_o , cause the fluctuation of the output voltage (see Figure 3.3). The voltage ripple is expressed as [35],

$$\Delta v_o = \frac{\Delta q_o}{C_2}$$

3-5

Figure 3.4 explains the charge change obtained by integrating the area under the output current curve, which is approximated as triangular.

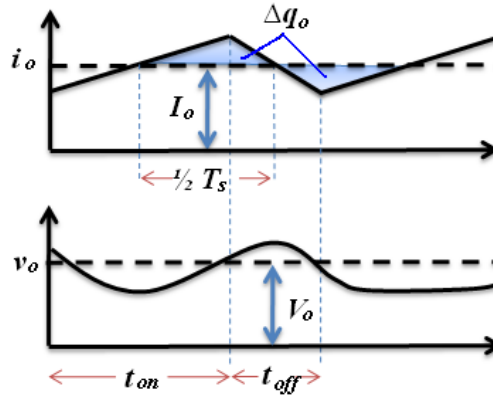


Figure 3.4 Output current and voltage waveforms for the Ćuk Converter

The capacitor accumulates charge Δq_o during charging state shown by the shaded area in Figure 3.4 equals that when the capacitor discharges and can be approximated as

$$\Delta q_o = \frac{1}{2} \frac{T_s}{2} \frac{\Delta i_{L2}}{2} = \frac{T_s \Delta i_{L2}}{8}$$

Substituting Δi_{L2} by equation 3-4, we have output ripple voltage expressed as

$$\Delta v_o = \frac{V_o(1-K)T_s}{8C_2 L_2 f}$$

Thus the capacitance value can be expressed as

$$C_2 = \frac{V_o(1-K)}{8 \Delta v_o L_2 f^2}$$

3-6

where Δi_{L2} and Δv_o are the desired output current and voltage ripples, respectively. Since the circuit is input-output symmetrical, the above analysis is applicable to input current and voltage inductor and capacitor.

From the above it is clear that the voltage ripples at both input and output ends can be minimised by selecting the corner frequency of the second order L-C low-pass filter which is expressed as

$$f_c = \frac{1}{2\pi\sqrt{L_2C_2}}$$

This is much lower than the switching frequency f and is independent of the input and output power, so long as the converter operates in continuous-conduction mode.

Energy Transfer Capacitor C_n :

Assuming the mean input current I_{L1} is constant, and at switching on-state, $V_{L1} = 0$ so capacitor C_n can be written as:

$$C_n = \frac{I_{L1} K}{\Delta v_{Cn} f}$$

3-7

Here Δv_{Cn} is the peak to peak fluctuation in the voltage across the capacitor C_n which has to be sufficiently large, so that the ripple voltage can be small.

In the particular application of the converter described in this work, it is not being used to feed power to a constant voltage bus, but is used to divert variable amounts of power between two PV panels of nominally identical features which are equally likely to be shaded. Hence the converter used for this power flow control would naturally be made completely symmetrical. This property allows a number of simplifying assumptions to be made in order to choose the component values of the converter, which are listed below:

- The ratings of Input voltage and output voltage are in the same range,
- The inductance values and current ratings of the input and output inductors are the same,
- The capacitance values of the input/output filter capacitors and voltage ratings are the same,

- For the calculation of the ripple a duty cycle near 50% is assumed, and finally
- The converter is lossless; so switches are considered ideal.

3.3 Bidirectional Ćuk Converter with photovoltaic application

The Ćuk converter has been used in photovoltaic applications such as Isolated topology to improve transmission efficiency[62], using control techniques to improve reliability in PV applications [64], simulation and Implementation of advance MPPT techniques [73], [75], due to its advantages previously mentioned. This converter is now used as a possible solution to the PV partial shading conditions in order to achieve the maximum power generation. Figure 3.5 shows the proposed circuit diagram to use a bidirectional Ćuk converter for the power control of two PV panels; i.e. the basic converter-PV integrated module. Configuration of the system for this basic unit to obtain maximum power generation is given in 3.6.

3.3.1 Bidirectional Ćuk Converter

For the basic Ćuk converter circuit described above, when another switch and diode are connected in parallel on either side of the capacitor C_n and in reverse polarity to the original pair shown in Figure 3.1, the result is a bidirectional Ćuk converter. Such a circuit allows power transfer from either left to right or vice versa. Thus when an input source voltage is connected on the left hand terminals, switch-diode pair S_1 and D_2 are active, enabling power flow from left input to right output with voltage relationship as given by equation 3-3

On the other hand, if the input source is on the right-hand side, the active switch/diode pair is S_2 and D_1 as before. In general a power source is defined as a device which can produce power and has a non-zero open circuit voltage, while a load cannot generate voltage by itself but has a defined voltage and current relationship [92].

3.3.2 Application of a bidirectional Ćuk converter with two PV panels

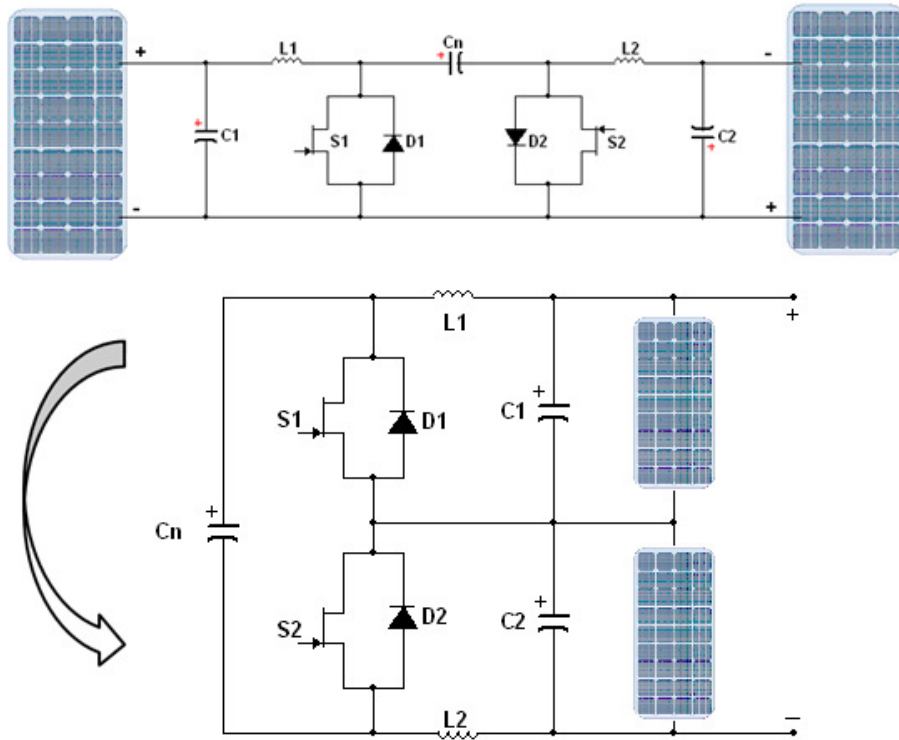


Figure 3.5 Interconnection of two PV Panels with the Bidirectional Ćuk Converter

When the Bidirectional Ćuk Converter above is applied to control a PV power generator consisting of two panels, its connection to them is as shown in Figure 3.5(a). i.e. one PV panel is wired on the left-hand side terminals, and the other is on the right-hand side. It will be assumed that the two PV panels have nominally identical features and are equally likely to be shaded. To form a complete system capable of extracting all the available power generated by both panels, a load resistor or a terminal converter may be required. This could be either step-up or step-down, dc-dc or dc-ac converter depending on the load. As shown in Figure 3.6, in this work a dc-dc step-up converter is used. The input terminals of this converter are connected to the positive node of PV_1 and the negative node of PV_2 .

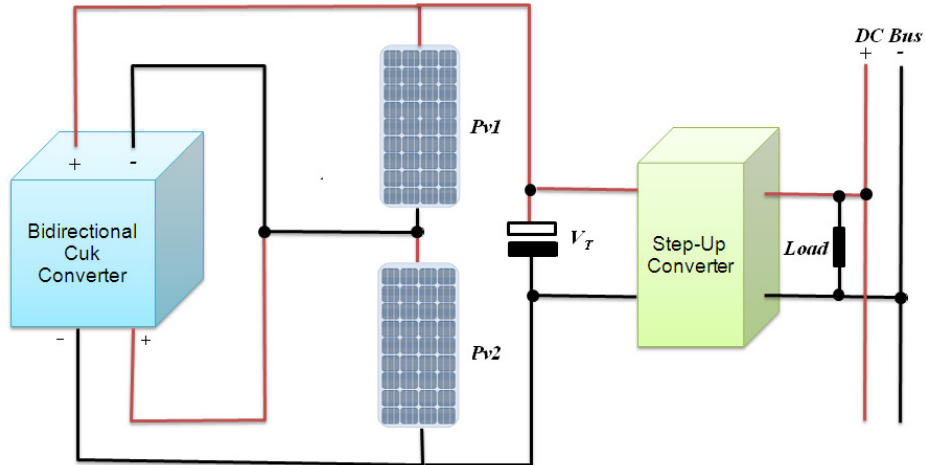


Figure 3.6 Integrated Photovoltaic Converter connected to a DC Bus

If there is no mismatching in the operating conditions of the two panels, the interconnection of PV_1 and PV_2 will behave as if they were a serially connected PV panels and the current will flow equally through the two photovoltaic panels. The bi-directional converter between them is idle, and its switch drivers are turned off.

However, with mismatching between two PV panels operating conditions, due to shading, power generated by two panels would be different, and the bi-directional converter needs to be controlled actively. Note the power difference due to mismatching of PV panel characteristics is not considered.

Sun Irradiation	G_1	G_2	Active components	Duty ratio
No Mismatch	Same	Same	---	---
Mismatch	High	Low	S_1-D_2	K_1
Mismatch	Low	High	S_2-D_1	K_2

Table 3-1 Switch/Diode Bidirectional behaviour

3.4 Operations under Uneven Solar irradiation

3.4.1 Case when Irradiation over PV₁ is greater than PV₂

When irradiation on PV₁ is higher than that on PV₂, the power available from the former is naturally higher [2], [59]. The set of switch and diode pair S₁ and D₂ should be activated by the controller as shown in Table 3-1. This provides an additional path for the current from PV₁ to flow without being consumed by the shaded panel which may become a load hence causing hotspot effect in the system [68].

As shown in Figure 3.7, the effect of activating S₁ and D₂ is that PV₁ becomes the voltage source of the bidirectional Ćuk converter. The converter output current is superimposed to the current from PV₂ and supplied to the output load. The key to this action is the sign inversion between the input and output currents of the converter. This means that positive current diverted from one of the terminals of PV₁ is added to the positive terminal current of PV₂.

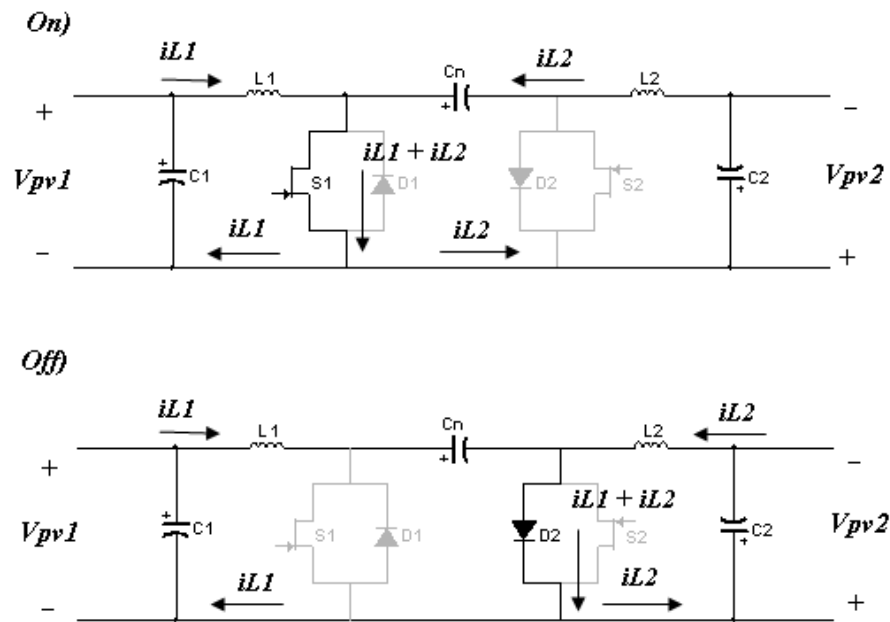


Figure 3.7 Switch Stage of the Ćuk Converter with $G_1 > G_2$

3.4.2 Case when irradiation over PV₂ is greater than PV₁

This situation is opposite to the previous case and is caused mainly by the irradiation on P_{v2} being higher than that on P_{v1} ; the power that can be extracted from the former is naturally higher. The switch and diode pair, S_2 and D_1 , will be made active as shown in Table 3-1; the effect is that P_{v2} now becomes the power source for the converter. The current flow in the circuit under this condition is as shown in Figure 3.8.

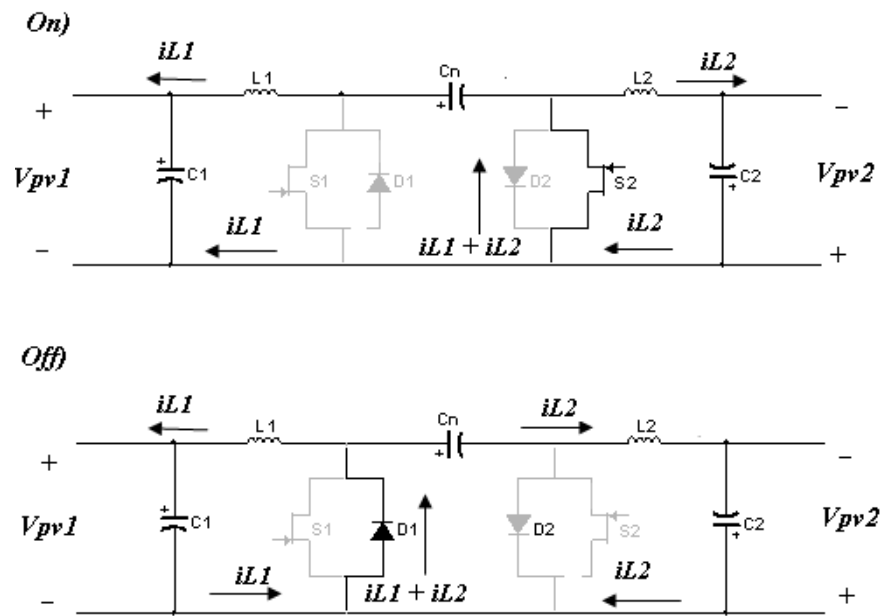


Figure 3.8 Switch Stage of the Ćuk Converter with $G_2 > G_1$

3.4.3 Power Flow Analysis

In continuous conduction mode, the total power, P_T harvested by the system at steady state can be expressed as

$$P_T = V_T I_T$$

3-8

Assuming both panels are physically identical with the same current/voltage ratings, the inductors currents are assumed to be continuous and capacitor

voltages be constant and ripple free, Eq. 3-8 can be re-written in terms of voltages across P_{v1} and P_{v2} and total current as

$$P_T = (V_{PV1} + V_{PV2})I_T \quad 3-9$$

where V_{PV1} and V_{PV2} are the terminal voltages of the photovoltaic panels P_{v1} and P_{v2} respectively in volts, V_T is the total output voltage (volts) and I_T is the total output current in amperes and also the current flowing through both panels.

However if P_{v2} is now shaded and P_{v1} is assumed generating higher power with current I_{PV1} , hence taken as the input source, switch pair S_1 - D_2 is active, the total current I_T can be calculated by:

$$I_T = I_{PV1} - I_{L1} \quad 3-10$$

or

$$I_T = I_{PV2} + I_{L2} \quad 3-11$$

Where I_{L1} and I_{L2} respectively are the currents flowing through inductors L_1 and L_2 . Furthermore, for a Bidirectional Ćuk converter, from equation 3-3, the voltage relation with the duty ratio can be formulated by

$$V_{PV2} = \frac{K_1}{1 - K_1} V_{PV1} \quad 3-12$$

On the other hand If P_{v1} is shaded, hence becoming the output end and P_{v2} is the input source, S_2 - D_1 is active, the relationship is given as:

$$V_{PV1} = \frac{K_2}{1 - K_2} V_{PV2}$$

3-13

The inductor current relation with the duty cycle can be adapted from equation 3-2, hence we have

$$\frac{I_{L2}}{I_{L1}} = \frac{1 - K1}{K1} = \frac{K2}{1 - K2}$$

3-14

Therefore, replacing equation 3-14 in 3-11 gives

$$I_{L1} = (I_T - I_{PV2}) \left(\frac{K1}{1 - K1} \right)$$

3-15

and equation 3-15 in 3-10

$$I_T = I_{PV1}(1 - K1) + I_{PV2}K1$$

3-16

In addition, the system overall power can be expressed by substituting equations 3-12 and 3-16 in 3-9

$$P_T = \left\{ V_{PV1} + V_{PV1} \left(\frac{K1}{1 - K1} \right) \right\} \{ I_{PV1}(1 - K1) + I_{PV2}K1 \}$$

3-17

hence,

$$P_T = V_{PV1}I_{PV1} + V_{PV1} \left(\frac{K1}{1 - K1} \right) I_{PV2}$$

3-18

With the analysis of equation 3-18, it can be concluded that by varying the K_1 value, the power produced by the shaded panel P_{V2} will also vary.

- If $K_1=0$: P_{V2} is effectively shorted by a bypass diode and is not producing power; therefore, the total output power is exclusively produced by P_{V1} .

- If $0 < K_1 < 1$: The power produced by P_{V2} will vary adding the power to the system output

3.5 Integrated-converters with three PV Panels

In the case of having the third PV panel connected in series to the system, the second Bidirectional Ćuk Converter is needed and wired across the second and third PV panels, the configuration of the circuit is shown in Figure 3.9. Such a case follows a new set of rules for the activation of specific switches depending on differences of solar irradiation levels on each of the three panels.

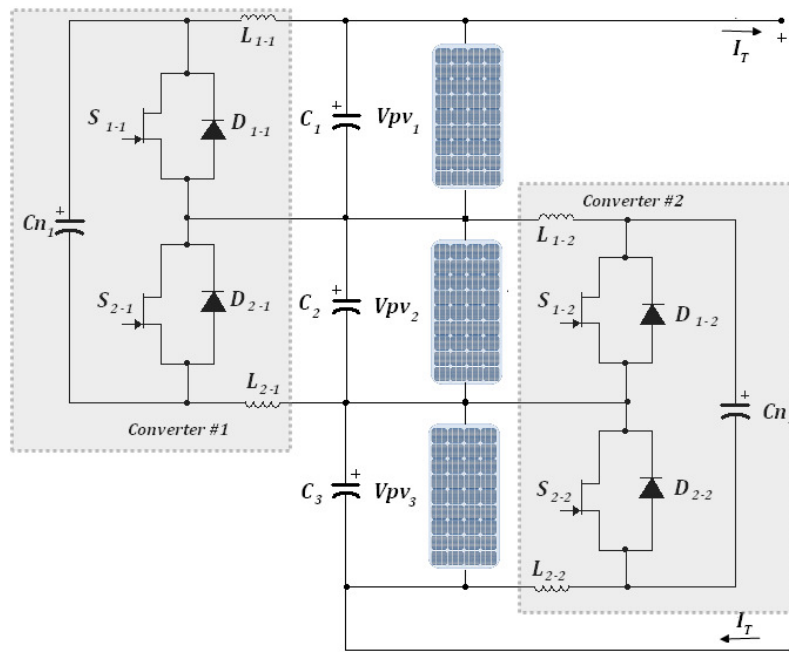


Figure 3.9 Configuration for three Solar Panel System

As stated before in the two panel case when the levels of solar light on three panels are the same, the current generated on each panel should ideally be the same; hence both converters are idle. However when the light levels are different one or both bidirectional converters would be active. In each converter circuit, the pair of switch and diode set being active depends on the levels of solar irradiance

on the two PV panels connected on the converter's two terminals. Considering all light pattern combinations possibly, we can list 4 different scenarios where the two pairs of switch and diode are active (Table 3-2). Correct determination of which of the two panels for a converter should act as its input or output can harness the maximum power generated from this PV system.

The operation modes for the two converters are determined based on the following analysis. Assuming switch pair $S_{1.1} - D_{2.1}$ in converter 1 is active, the current flowing through $L_{1.1}$ is

$$I_{pv1} - I_T > 0 \quad 3-19$$

This implies that current generated by PV 1 is higher than that flowing through the three serially linked panels, hence expressing in power and voltage terms we have

$$\frac{P_{pv1}}{V_{pv1}} > \frac{P_{pv1} + P_{pv2} + P_{pv3}}{V_{pv1} + V_{pv2} + V_{pv3}} \quad 3-20$$

Re-arranging the inequality formula 3-20 gives

$$\frac{V_{pv1} + V_{pv2} + V_{pv3}}{V_{pv1}} > \frac{P_{pv1} + P_{pv2} + P_{pv3}}{P_{pv1}} \quad 3-21$$

Observing I-V characteristic curves of a PV panel, it is evident that the changes of voltage corresponding to the changes of the maximum power points due to light level variations are not significant [5]. Thus it is adequate to assume that the three panels have the same average voltage, so formula 3-21 can be written as

$$3P_{pv1} > P_{pv1} + P_{pv2} + P_{pv3}$$

As mentioned before, power is assumed to be directly proportional to solar irradiance, G , so we write

$$3G_1 > G_1 + G_2 + G_3$$

$$\frac{G_2 + G_3}{2} < G_1$$

3-22

Formula 3-22 expresses the relationship of three solar irradiances respectively to three different panels when $S_{1.1} - D_{2.1}$ are active. The same analysis can be applied to the situation when switch and diode pair, $S_{2.1} - D_{1.1}$, is active, in this case the current flowing through $L_{1.1}$, is in reverse direction to the previous condition so it follows that

$$I_{pv1} - I_T < 0$$

3-23

hence

$$\frac{G_2 + G_3}{2} > G_1$$

3-24

While converter #1 analysis above is based upon the current flowing from/to $L_{1.1}$, converter #2 is now analyzed according to the current flowing from/to inductor $L_{2.2}$. The switch pair $S_{1.2} - D_{2.2}$ is activated if the light conditions $\frac{G_1 + G_2}{2} > G_3$ occurs. On the other hand, switch pair $S_{1.2} - D_{2.2}$ will be activated when $\frac{G_1 + G_2}{2} < G_3$. With these four light conditions and four operating modes a set of switch combinations are assembled as shown in Table 3-2.

Mode	Active Pair Switch and Diode		Unit 1		Unit 2		Light Conditions
	Converter #1	Converter #2	Input	Output	Input	Output	
1	$S_{1.1} - D_{2.1}$	$S_{2.2} - D_{1.2}$	PV_1	PV_2	PV_3	PV_2	$\frac{G_2 + G_3}{2} < G_1$ and $\frac{G_1 + G_2}{2} < G_3$
2	$S_{2.1} - D_{1.1}$	$S_{1.2} - D_{2.2}$	PV_2	PV_1	PV_2	PV_3	$\frac{G_2 + G_3}{2} > G_1$ and $\frac{G_1 + G_2}{2} > G_3$
3	$S_{1.1} - D_{2.1}$	$S_{1.2} - D_{2.2}$	PV_1	PV_2	PV_2	PV_3	$\frac{G_2 + G_3}{2} < G_1$ and $\frac{G_1 + G_2}{2} > G_3$
4	$S_{2.1} - D_{1.1}$	$S_{2.2} - D_{1.2}$	PV_2	PV_1	PV_3	PV_2	$\frac{G_2 + G_3}{2} > G_1$ and $\frac{G_1 + G_2}{2} < G_3$

Table 3-2 Three Panel Case switching configuration

3.6 Converter components design

The converter design should be based on parameters of the power source and load. In this case, the PV panels given in subsection 2.2 are taken as the sources of the system. Such PV Panels can generate an average voltage of up to 20 volts and current of 3.3 amps under optimal lighting and temperature conditions. A maximum ripple of 5% is chosen as acceptable for current and voltage.

Current ripple can be calculated to be $\Delta i = 165mA$ and duty cycle is considered to be 50% with a switching frequency of 20 kHz. With equation 3-4 the value of inductor L_2 can be expressed as

$$L_2 = \frac{V_o (1 - K)}{\Delta i_{L2} f} = \frac{20volts * 0.5}{165mA * 20kHz} = 3.03mH$$

Applying the same principle for voltage ripple on the converter capacitors, C_1 and C_2 are obtained for $\Delta v = 1V$ as:

$$C_{1-2} = \frac{I_L(1-k)}{8\Delta v f} = \frac{3.3A * 0.5}{8 * 1V * 20 kHz} = 10.3\mu F$$

Thus, C_n is obtained by

$$C_n = \frac{I_L(1-k)}{f * \Delta V} = \frac{3.3A * 0.5}{20 kHz * 1V} = 82.5\mu F$$

Although capacitance values are important for this implementation and higher value of the capacitor would incur a slowing down of the step response, the system itself does not operate in a time critical application, and hence flexibility in choosing capacitors can be allowed.

3.7 Discontinuous Conduction Mode (DCM)

Since the Ćuk Bidirectional Converter works with both input and output connected to solar modules, is important avoid the discontinuous conduction mode knowing when the converter follows from CCM to DCM.

There are two scenarios where the converter can go into the DCM [90] :

- If both PV panels are equally irradiated and the converter is forced to work normally, the power that is transferred from one circuit end to another is a small fraction of the converter ratings; the average inductor current will then become lower than half peak to peak inductor current forcing the converter to work in Discontinuous Diode Conduction Mode (DDCM).
- If the case when one of the PV panels is fully irradiated while the other is without irradiation happens, the converter has to shuffle a large amount of current which may lead to full discharging of energy stored in the transfer capacitor C_n , consequently the capacitor voltage goes to zero before the completion of On time which results in Discontinuous Capacitor Voltage Mode (DVCM).

Both parameters are taken into consideration designing the activation algorithm in subchapter 5.2.1.2 to avoid DCM in the Ćuk Bidirectional Converter integrated with PV panels.

3.8 Summaries

This chapter presented a module integrated PV-converter unit using the Ćuk Bidirectional Converter. The circuit and operation principle of the basic Ćuk converter were described, and its output to input voltage and current relationships were derived. The main advantage of the Ćuk converter compared to other DC-DC converter topologies is that it gives low current ripples in both input and output ends [48]. The Bidirectional Ćuk Converter topology is considered to be a solution for the control of PV power generators when the panels in the installation are under different solar irradiance. The module integrated PV converter unit is formed by wiring two PV panels respectively to the converter's two terminals. Principles of power flow control in such a unit were described. Multiple of Such units can be connected in series for generating higher voltage output. Configuration of a system having three solar panels and two Bidirectional Ćuk Converters was shown and explained.

A switching scheme was necessary for the control of power flow in the three solar panel system. The aim of such a scheme is to find the maximum power point based upon the irradiance on each panel. For this, selection rules dependent on the relative levels of panel irradiances were developed and summarised.

Chapter 4

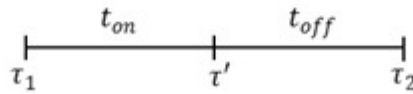
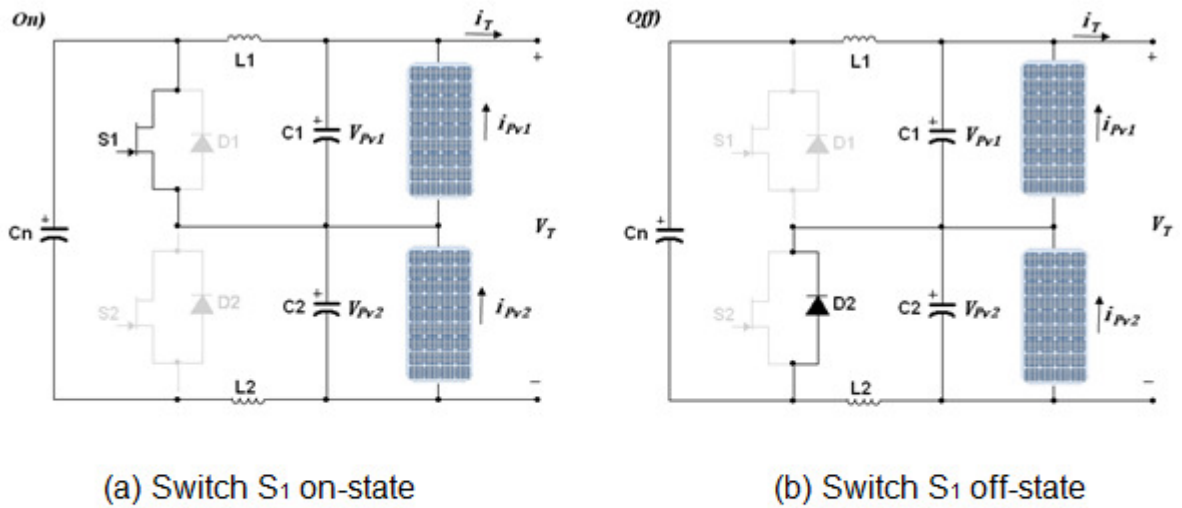
Ćuk Converter Transfer Functions Using State-Space Averaging

As described in the previous chapter, one of the objectives in this work is to obtain the optimal control of the integrated converter-PV module for maximum power generation under uneven lighting conditions. To design the control scheme and evaluate its performance it is necessary to study the dynamic behaviour of the Ćuk converter and its integration with the PV panels. This requires developing mathematical models expressing the relationships between the converter input and output variables. This chapter presents the development of transfer functions for system comprised of a Ćuk bi-directional converter with two PV panels. This is through, firstly, deriving the state-space equations for different converter operating states in a continuous-conduction mode. State-variable averaging technique over the switching period and small signal perturbations are then applied in order to lead to transfer function derivation using procedure previously stated by Slobodan Ćuk et al. in [50], [56], [60], [91]. Moreover, a thorough analysis to the transfer functions is performed by step and frequency response when the solar modules are under the effects of partial shading. Transfer functions step responses are contrasted with a Simulink model.

4.1 State-Space Equations for Ćuk Converter

The analysis below considers the operation when S_1 and D_2 are active, and their states are according to the duty ratio set by the PWM signal represented in Figure 4.1. As a rule, the number of state variables is equal to the number of energy

storage components in the circuit. In this case they are the voltages across the capacitors C_n , C_1 and C_2 , the latter two are also the terminal voltages of V_{Pv1} and V_{Pv2} , the current flowing through the inductors L_1 and L_2 , thus forming a state vector $x = [i_{L1}; i_{L2}; V_{Pv1}; V_{Pv2}; V_{Cn}]$.



(c) Switching abbreviations

Figure 4.1 Switch State Analysis

- Switching on State:

When switch S_1 is turned on as shown in Figure 4.1(a), the state equations for all the state variables are given below:

The rate of change of current through inductor L_1 is expressed as

$$\frac{di_{L1}(t)}{dt} = \frac{V_{Pv1}}{L_1},$$

that for L_2 is given as

$$\frac{di_{L2}(t)}{dt} = \frac{V_{Cn}}{L_2} - \frac{V_{Pv2}}{L_2}.$$

The rate of change of PV₁ input voltage is given as

$$\frac{dV_{Pv1}(t)}{dt} = \frac{i_{Pv1}}{C_1} - \frac{i_T}{C_1} - \frac{i_{L1}}{C_1},$$

, and the variation rate of V_{pv2} is

$$\frac{dV_{Pv2}(t)}{dt} = \frac{i_{L2}}{C_2} - \frac{i_T}{C_2} + \frac{i_{Pv2}}{C_2}.$$

Then rate of change of V_{cn} is

$$\frac{dV_{Cn}(t)}{dt} = -\frac{i_{L2}}{C_n}$$

4-1

Writing the above equation using state vector form we have

$$\dot{x} = \mathbf{A}_{on}x + \mathbf{B}i_T + \mathbf{Q}_1i_{Pv1} + \mathbf{Q}_2i_{Pv2}$$

4-2

$$\text{where } x = \begin{bmatrix} i_{L1} \\ i_{L2} \\ V_{Pv1} \\ V_{Pv2} \\ V_{Cn} \end{bmatrix}, \mathbf{A}_{on} = \begin{bmatrix} 0 & 0 & 1/L_1 & 0 & 0 \\ 0 & 0 & 0 & -1/L_2 & 1/L_2 \\ -1/C_1 & 0 & 0 & 0 & 0 \\ 0 & 1/C_2 & 0 & 0 & 0 \\ 0 & -1/C_n & 0 & 0 & 0 \end{bmatrix}, \mathbf{B} = \begin{bmatrix} 0 \\ 0 \\ -1/C_1 \\ -1/C_2 \\ 0 \end{bmatrix},$$

$$\mathbf{Q}_1 = \begin{bmatrix} 0 \\ 0 \\ -1/C_1 \\ 0 \\ 0 \end{bmatrix} \text{ and } \mathbf{Q}_2 = \begin{bmatrix} 0 \\ 0 \\ 0 \\ 1/C_2 \\ 0 \end{bmatrix}.$$

If the switching frequency is sufficiently high, the elements in x are changing linearly with time. Hence, the rate of change of the state variables can be approximated as

$$\dot{x} \approx \frac{x(\tau') - x(\tau_1)}{t_{on}},$$

4-3

where τ_1 denotes the time to turn on S_1 while τ' is the end of turn on time, and $t_{on} = \tau' - \tau_1$, substituting this into equation 4-2, we have

$$x(\tau') = (\mathbf{I} + \mathbf{A}_{on}t_{on})x(\tau_1) + (\mathbf{B}i_T + \mathbf{Q}_1i_{Pv1} + \mathbf{Q}_2i_{Pv2})t_{on},$$

4-4

where \mathbf{I} is the unity matrix.

- Switching off State:

When the switch is turned off (Figure 4.1b), the mathematical representations of the components are:

$$\frac{di_{L1}(t)}{dt} = \frac{V_{Pv1}}{L_1} - \frac{V_{Cn}}{L_1}$$

$$\frac{di_{L2}(t)}{dt} = -\frac{V_{Pv2}}{L_2}$$

$$\frac{dV_{Pv1}(t)}{dt} = \frac{i_{Pv1}}{C_1} - \frac{i_T}{C_1} - \frac{i_{L1}}{C_1}$$

$$\frac{dV_{Pv2}(t)}{dt} = \frac{i_{L2}}{C_2} - \frac{i_T}{C_2} + \frac{i_{Pv2}}{C_2}$$

$$\frac{dV_{Cn}(t)}{dt} = -\frac{i_{L1}}{C_n}$$

4-5

Similarly using state variable representation we write the above state-space equations as

$$\dot{x} = \mathbf{A}_{off}x + \mathbf{B}i_T + \mathbf{Q}_1i_{Pv1} + \mathbf{Q}_2i_{Pv2},$$

4-6

$$\text{where } \mathbf{A}_{off} = \begin{bmatrix} 0 & 0 & 1/L_1 & 0 & -1/L_1 \\ 0 & 0 & 0 & -1/L_2 & 0 \\ -1/C_1 & 0 & 0 & 0 & 0 \\ 0 & 1/C_2 & 0 & 0 & 0 \\ 1/C_n & 0 & 0 & 0 & 0 \end{bmatrix}.$$

If the switching period is sufficiently short, the elements in x are changing linearly with time. Hence, we have

$$\dot{x} \approx \frac{x(\tau_2) - x(\tau')}{t_{off}},$$

4-7

where τ_2 denotes the end of turn off time $t_{off} = \tau_2 - \tau'$. Substituting this into equation 4-6, we have

$$x(\tau_2) = (\mathbf{I} + \mathbf{A}_{off}t_{off})x(\tau') + (\mathbf{B}i_T + \mathbf{Q}_1i_{pv1} + \mathbf{Q}_2i_{pv2})t_{off}$$

4-8

Eliminating $x(\tau')$ by substituting Equation 4-4 into Equation 4-8 gives

$$\begin{aligned} x(\tau_2) = & (\mathbf{I} + \mathbf{A}_{off}t_{off})(\mathbf{I} + \mathbf{A}_{on}t_{on})x(\tau_1) \\ & + (\mathbf{I} + \mathbf{A}_{off}t_{off})(\mathbf{B}i_T + \mathbf{Q}_1i_{pv1} + \mathbf{Q}_2i_{pv2})t_{on} \\ & + (\mathbf{B}i_T + \mathbf{Q}_1i_{pv1} + \mathbf{Q}_2i_{pv2})t_{off} \end{aligned}$$

4-9

When the switching frequency is sufficiently high, $t_{on}t_{off}$, t_{on}^2 and t_{off}^2 are significantly smaller than any products of two passive L and C components. Hence, equation 4-9 can be re-written as

$$x(\tau_2) = (\mathbf{I} + \mathbf{A}_{off}(1-k)T_s + \mathbf{A}_{on}kT_s)x(\tau_1) + (\mathbf{B}i_T + \mathbf{Q}_1i_{pv1} + \mathbf{Q}_2i_{pv2})T_s$$

4-10

where $(1 - k)T_s = t_{off}$, $kT_s = t_{on}$ and $T_s = t_{on} + t_{off}$, and

Therefore, the averaged state-space model for the converter is given by

$$\dot{x}_{Av} \approx \frac{x(\tau_2) - x(\tau_1)}{T_s}$$

or

$$\dot{x}_{Av} = \mathbf{A}_T x + \mathbf{B}i_T + \mathbf{Q}_1 i_{pv1} + \mathbf{Q}_2 i_{pv2}$$

4-11

where $\mathbf{A}_T = \mathbf{A}_{on}k + \mathbf{A}_{off}(1 - k)$

$$\text{hence, } \mathbf{A}_T = \begin{bmatrix} 0 & 0 & 1/L_1 & 0 & -\frac{(1-k)}{L_1} \\ 0 & 0 & 0 & -1/L_2 & k/L_2 \\ -1/C_1 & 0 & 0 & 0 & 0 \\ 0 & 1/C_2 & 0 & 0 & 0 \\ \frac{(1-k)}{C_n} & -k/C_n & 0 & 0 & 0 \end{bmatrix}$$

4.2 Introducing Small ac Perturbation Signals

By introducing small ac perturbation signals, denoted by the symbol “ $\hat{\cdot}$ ” in the above averaged state-space variables, we have:

$$x = X + \hat{x}$$

$$k = K + \hat{k}$$

$$i_{pv1} = I_{pv1} + \hat{i}_{pv1}$$

$$i_{pv2} = I_{pv2} + \hat{i}_{pv2}$$

$$i_T = I_T + \hat{i}_T$$

4-12

Then, after derivations (see Appendix A) equation 4-11 can be expressed as

$$\hat{\dot{x}} = \mathbf{A}_{sm}\hat{x} + \mathbf{B}\hat{i}_T + \mathbf{Q}_1\hat{i}_{pv1} + \mathbf{Q}_2\hat{i}_{pv2} + \mathbf{J}\hat{k}$$

4-13

$$\text{where } \mathbf{A}_{sm} = \begin{bmatrix} 0 & 0 & 1/L_1 & 0 & -\frac{(1-K)}{L_1} \\ 0 & 0 & 0 & -1/L_2 & K/L_2 \\ -1/C_1 & 0 & 0 & 0 & 0 \\ 0 & 1/C_2 & 0 & 0 & 0 \\ \frac{(1-K)}{C_n} & -K/C_n & 0 & 0 & 0 \end{bmatrix} \text{ and } \mathbf{J} = \begin{bmatrix} \frac{V_{pv1}+V_{pv2}}{L_1} \\ \frac{V_{pv1}+V_{pv2}}{L_2} \\ 0 \\ 0 \\ \frac{I_{pv2}-I_{pv1}}{C_n} \end{bmatrix}$$

Under a specific weather conditions, \hat{i}_{pv1} and \hat{i}_{pv2} vary according to its respective I-V characteristics and its normal operating range, thus they are expressed as

$$\hat{i}_{pv1} = -\frac{\hat{v}_{pv1}}{R_{pv1}} \text{ and } \hat{i}_{pv2} = -\frac{\hat{v}_{pv2}}{R_{pv2}},$$

4-14

where R_{pv1} and R_{pv2} are the slopes dV/dI of the I – V characteristic at their respective steady state points and are always varying.

Eliminating the terms with \hat{i}_{pv1} and \hat{i}_{pv2} by substituting Equation 4-14 into Equation 4-13, we obtain

$$\hat{\dot{x}} = \mathbf{A}^*_{sm}\hat{x} + \mathbf{B}\hat{i}_T + \mathbf{J}\hat{k}$$

4-15

$$\text{where } \mathbf{A}^*_{sm} = \begin{bmatrix} 0 & 0 & 1/L_1 & 0 & -\frac{(1-K)}{L_1} \\ 0 & 0 & 0 & -1/L_2 & K/L_2 \\ -1/C_1 & 0 & -\frac{1}{R_{pv1}C_1} & 0 & 0 \\ 0 & 1/C_2 & 0 & -\frac{1}{R_{pv2}C_2} & 0 \\ \frac{(1-K)}{C_n} & -K/C_n & 0 & 0 & 0 \end{bmatrix}$$

$$\text{and } \mathbf{J} = \begin{bmatrix} \frac{V_{Pv1} + V_{Pv2}}{L_1} \\ \frac{V_{Pv1} + V_{Pv2}}{L_2} \\ 0 \\ 0 \\ \frac{V_{Pv2}}{R_{Pv2}C_n} - \frac{V_{Pv1}}{R_{Pv1}C_n} \end{bmatrix}$$

The small-signal equation for the voltage across PV_1 is given as

$$\hat{v}_{Pv1} = \mathbf{Z}_1 \hat{\mathbf{x}}, \quad 4-16$$

where $\mathbf{Z}_1 = [0 \ 0 \ 1 \ 0 \ 0]$. Therefore, the small-signal equation for the voltage across PV_2 is given as

$$\hat{v}_{Pv2} = \mathbf{Z}_2 \hat{\mathbf{x}}, \quad 4-17$$

where $\mathbf{Z}_2 = [0 \ 0 \ 0 \ 1 \ 0]$.

4.3 Transformation of ac Equations to Transfer Functions

The above analysis assumes that the Ćuk converter works as a bypass DC/DC module for two PV panels hence it is taken as the first stage power conversion device. This is used to connect to the load and/or to a DC-bus [44]. Its power rating is higher than the inner Ćuk converter, so it has a slower dynamic and its controller sampling period is generally longer. Since it is assumed to be in steady state, the terminal current ripple \hat{i}_T is supposed as near zero. Taking the duty ratio as the control variable and the voltage across PV_1 as the controlled variable, the transfer function between them is:

$$G_{k1}(s) = \frac{\hat{v}_{Pv1}(s)}{\hat{k}(s)} = \mathbf{Z}_1 (s\mathbf{I} - \mathbf{A}^*_{sm})^{-1} \mathbf{J} = - \frac{\beta_3 s^3 + \beta_2 s^2 + \beta_1 s + \beta_0}{\alpha_5 s^5 + \alpha_4 s^4 + \alpha_3 s^3 + \alpha_2 s^2 + \alpha_1 s + \alpha_0} V_T$$

where

$$\alpha_5 = (CL)^2 C_n$$

$$\alpha_4 = CC_n L^2 \left(\frac{1}{R_{pv1}} + \frac{1}{R_{pv2}} \right)$$

$$\alpha_3 = C_n L \left(2C + \frac{L}{R_{pv1} R_{pv2}} \right)$$

$$\alpha_2 = L(C_n + CK^2 + C(1-K)^2) \left(\frac{1}{R_{pv1}} + \frac{1}{R_{pv2}} \right)$$

$$\alpha_1 = C_n + (K^2 + (1-K)^2) \left(C + \frac{L}{R_{pv1} R_{pv2}} \right)$$

$$\alpha_0 = \frac{(1-K)^2}{R_{pv1}} + \frac{K^2}{R_{pv2}}$$

and

$$\beta_3 = CC_n L$$

$$\beta_2 = \frac{C_n L}{R_{pv2}} + CL(1-K) \left(\frac{(1-K)}{R_{pv1}} - \frac{K}{R_{pv2}} \right)$$

$$\beta_1 = C_n + CK + \frac{L(1-K)}{R_{pv2}} \left(\frac{(1-K)}{R_{pv1}} - \frac{K}{R_{pv2}} \right)$$

$$\beta_0 = \frac{(1-K)^2}{R_{pv1}} + \frac{K^2}{R_{pv2}}$$

With the voltage across PV₂ as the controlled variable, the transfer function between this and the duty ratio \hat{k} is:

$$G_{k2}(s) = \frac{\hat{v}_{pv2}(s)}{\hat{k}(s)} = \mathbf{Z}_2(s\mathbf{I} - \mathbf{A}^*_{sm})^{-1}\mathbf{J} = \frac{\gamma_3 s^3 + \gamma_2 s^2 + \gamma_1 s + \gamma_0}{\alpha_5 s^5 + \alpha_4 s^4 + \alpha_3 s^3 + \alpha_2 s^2 + \alpha_1 s + \alpha_0} V_T$$

where

$$\gamma_3 = CC_nL$$

$$\gamma_2 = \frac{C_nL}{R_{Pv1}} + CLK \left(\frac{K}{R_{Pv2}} - \frac{(1-K)}{R_{Pv1}} \right)$$

$$\gamma_1 = C_n + C(1-K) + \frac{LK}{R_{Pv1}} \left(\frac{K}{R_{Pv2}} - \frac{(1-K)}{R_{Pv1}} \right)$$

$$\gamma_0 = \frac{(1-K)^2}{R_{Pv1}} + \frac{K^2}{R_{Pv2}}$$

4.4 Verification of Analysis and Simulation Verification of the Two Transfer functions

Note that the above two transfer functions are derived for the condition when S_1 and D_2 are in operation. Both are nonlinear functions of duty ratio K , dependent on their terminal voltage V_T , and they necessarily have the same denominator. The two numerators are also in the same form except that K in one is replaced by $1-K$ in the other. Under the condition that the operating points of two panels are the same, so that $R_{PV1}=R_{PV2}$, and $K=0.5$ the two transfer functions are identical. This is expected from the symmetry of the Ćuk converter circuit. In practice, this is the case when the irradiations on both PV panels are the same, and the Ćuk converter is switching but inactive. However when the light levels on the two panels are different the two transfer functions would not be the same since K is not 0.5; also, more importantly, the panel's internal resistances R_{PV1} and R_{PV2} may be very different.

To verify this point an example system of two PV panels with the bidirectional Ćuk converter configured as that described in Section 3.5 is simulated, and R_{pv1} and R_{pv2} values at operating points around their MPPs are calculated. These are listed in the table in Appendix B. The step response of a Simulink model of the integrated converter is compared with transfer function step responses

The transfer function simulation assumes that PV₁ is at 100% solar irradiance and PV₂ being partially shaded with 50%. The table shows that we have $R_{Pv2} > R_{Pv1}$ at all operating points listed. Figure 4.2 shows the I-V characteristic curves of these two PV panels under the given uneven light levels. It would be expected that the slope resistance would be greater at low light levels, and that this would also give less damping of the responses. This is found to be correct. In particular, when $K=0.475$ near their MPP points, $R_{PV1}= 6.32 \Omega$ while $R_{PV2} = 12.25\Omega$. When $K=0.55$, the difference between them is even more significant with $R_{PV1}=4.69\Omega$ and $R_{PV2}=90.79\Omega$. Consequently the two transfer functions present qualitatively different features. Observing $G_{k1}(s)$ in Equation 4-18, β_0 and β_3 are always positive, but β_1 and β_2 may change their polarity according to the R_{PV1} and R_{PV2} values. For the stated operating condition $R_{Pv2} > R_{Pv1}$ they are positive. Thus all β factors are positive, $G_{k1}(s)$ has, at least, no right-hand-side zeros. On the other hand, $G_{k2}(s)$ in Equation 4-19 shows a different feature to $G_{k1}(s)$ because the formulas for γ_1 and γ_2 , the two counterpart parameters to β_1 and β_2 , show that these may become negative as the other terms in their expressions are comparatively small. Consequently, depending on the PV panel operating points, zeros for $G_{k2}(s)$ may move to the right-hand-side of the s-plane and hence may present a non-minimum phase characteristic. As the system has structural symmetry, the situation simply reverses with the opposite irradiation unbalance.

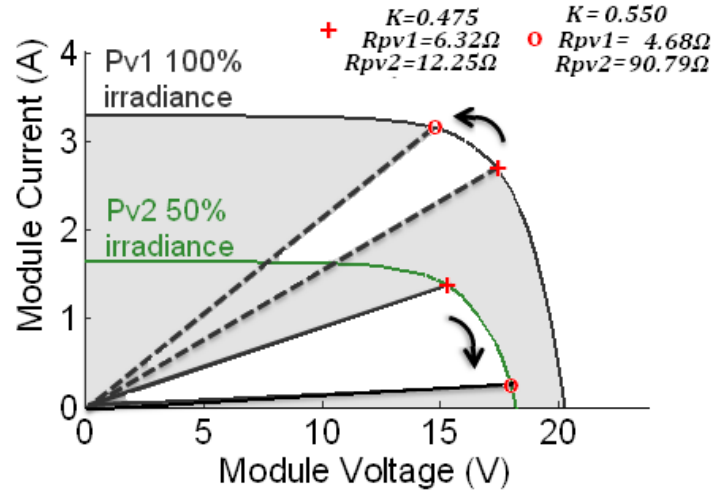


Figure 4.2 I-V characteristic from Pv1 at 100% and Pv2 at 50%

To verify the validity of the transfer functions developed, step response and frequency response tests of the two transfer functions were performed using the PV modules given in the table in Appendix B with the Ćuk converter parameters chosen in Section 3.5. Figure 4.3 and Figure 4.4 show the incremental step responses of V_{PV1} and V_{PV2} respectively with the duty ratio K varying from 0.475 to 0.575 in perturbation steps of $k=0.025$. As expected, the two sets of step responses are complementary and show similar features when K is around 0.5 (from 0.475 to 0.5). However, the response curves for $K = 0.525$ to 0.575 are different in that V_{PV1} remains only slightly under-damped while V_{PV2} is becoming progressively more oscillatory. This is due to the changes of zeros in transfer functions G_{k1} and G_{k2} affected mainly by R_{PV2} and R_{PV1} as well as the value of K . As shown in Figure 4.2, R_{PV2} increases rapidly from 12.25Ω to 90.79Ω , while R_{PV1} changes just from 6.32Ω to 4.68Ω .

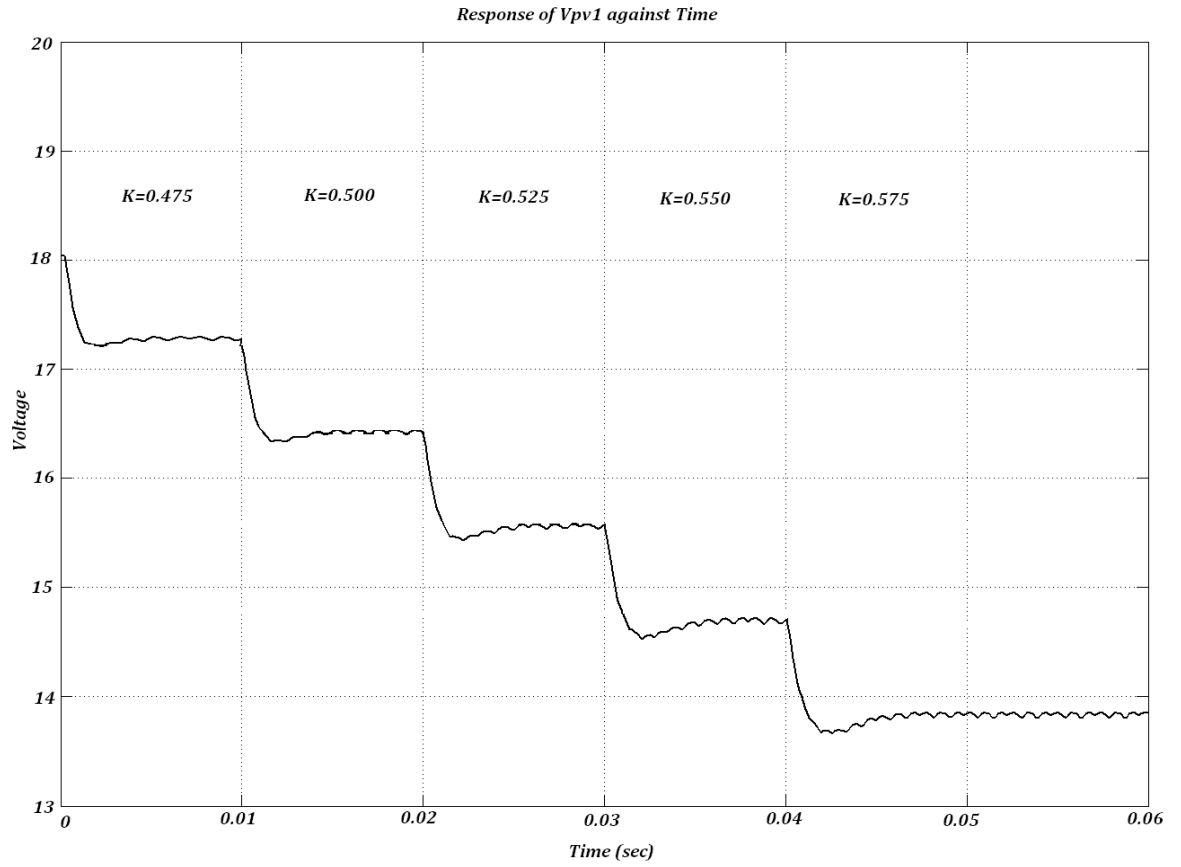


Figure 4.3 Step Response of V_{PV1} with different K values with $G_1=100\%$

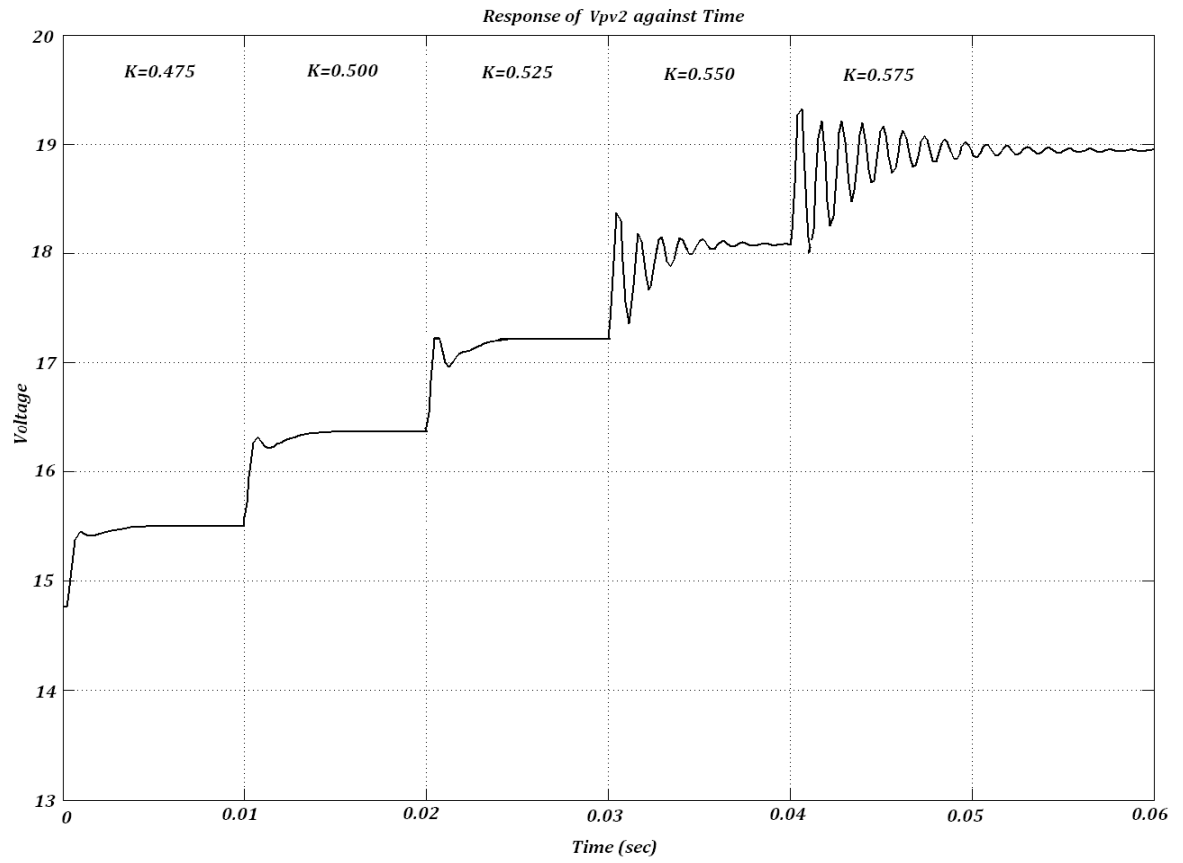


Figure 4.4 Step Response of V_{PV2} with different K values with G₂=50%

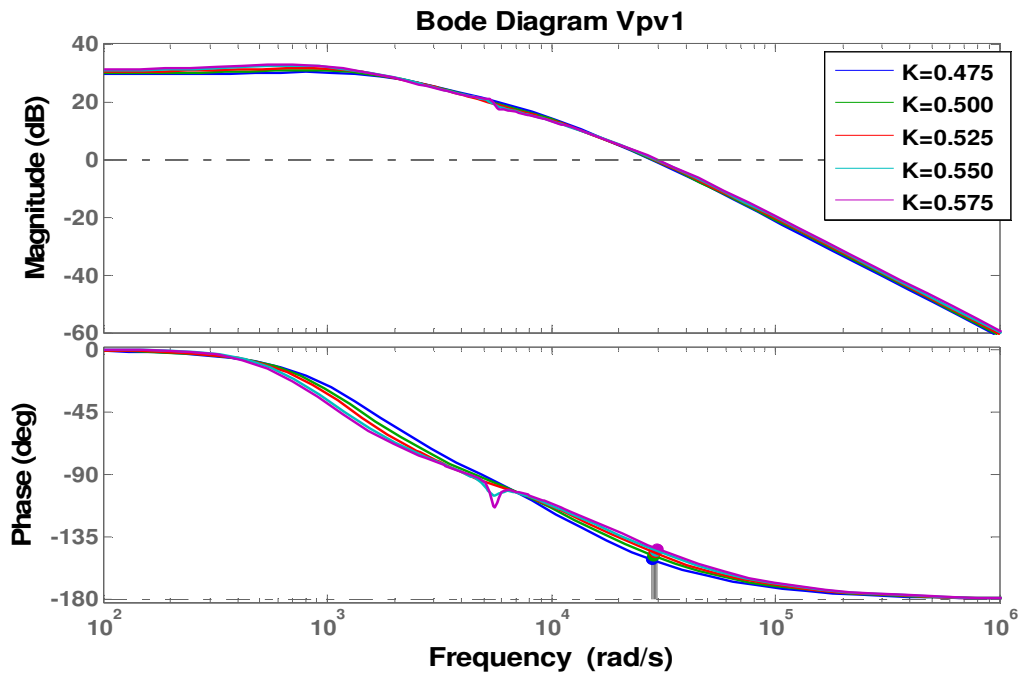


Figure 4.5 Bode plot of V_{pv1} for different K

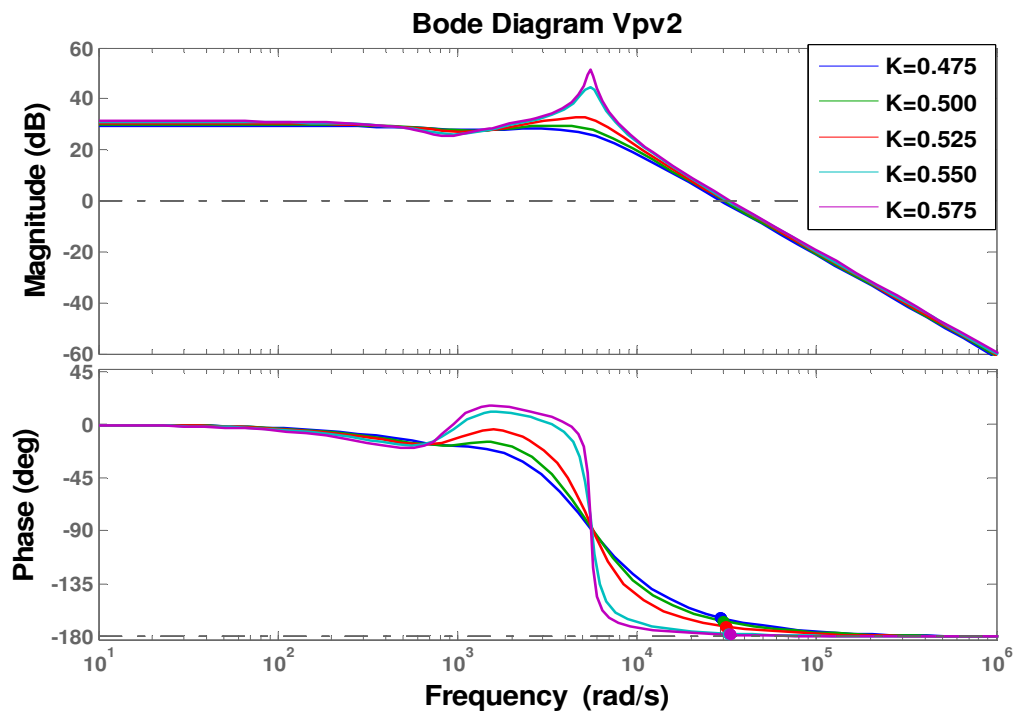


Figure 4.6 Bode plot of V_{pv2} for different K

The frequency responses of these two transfer function are shown by using the Bode plots of V_{pv1} and V_{pv2} as shown in Figure 4.5 and Figure 4.6. For $G_{k1}(s)$, in Figure 4.5 it shows that the transfer function has a fixed gain and minimum phase shift at low frequencies. The cut-off frequency is around $\omega_o = 5 \times 10^3 \text{ rad/s}$ and gain falls with a slope of around -30dB/decade and the phase shift towards -180° . For $G_{k2}(s)$, however, the level of transient overshoot increases as K increases while the oscillation frequency remains almost unchanged. This is shown in the Bode plot of Figure 4.6; the overshoot at the cut-off frequency around $\omega_o = 5 \times 10^3 \text{ rad/s}$ can be as high as 50% when $K=0.575$, showing reduction of damping with increasing K.

To confirm clearly the features shown in step-response and Bode plots, the pole-zero plots of $G_{k1}(s)$ are presented in Figure 4.7. As can be seen a pair of complex conjugate poles P_1, P_2 and a pair of complex conjugate zeros Z_1, Z_2 are both moving right towards the $j\omega$ -axis as K increases and they are almost overlapping each other throughout. Hence they are nearly cancelling each other and only make a small contribution to the response. However, this contribution is at high frequency, small amplitude and very weakly damped for $K = 0.55$. This can be seen as fine scale, small and persistent oscillations in the time responses. The remaining poles P_3, P_4 are only accompanied by the single zero Z_3 so their contribution to the response retains small amplitude which is slightly damped and at a lower frequency. These poles and zeros give the dominant characteristics of G_{k1} at $K=0.45$ and $K=0.55$.

Similar plots of G_{k2} pole-zero locations for $K = 0.45$ and 0.55 are shown in Figure 4.8 respectively. Clearly when K is 0.45, all 5 poles (one real and two complex conjugate pairs) and three zeros are on the left-hand side of s-plane, so the transfer function is both stable and minimum phase. It is slightly under-damped behaviour is due to the two complex conjugate poles P_1 and P_2 , which have higher ω values. The other two complex conjugate poles, P_3 and P_4 , have a lower ω values and are close to the pair of complex conjugate zeros, Z_1 and Z_2 , so they nearly cancel each other. However for $K=0.55$, P_3, P_4 and Z_1, Z_2 are almost at the same location in s-plane, but P_1 and P_2 move very close to $j\omega$ -axis; hence the

response is strong and heavily under-damped. Note pole P_5 and zero Z_3 in both cases are far to the left on the σ -axis, so its effect decays very fast. This behaviour is clearly shown in the step responses, in Figure 4.4.

Transfer functions with the change of the duty ratio and PV panels internal impedances are presented as follows:

- When $K=0.450$:

$$Gk1 = -\frac{2.804^{-12}s^3 + 2.317^{-8}s^2 + 9.457^{-5}s + 0.06435}{9.531^{-20}s^5 + 2.218^{-15}s^4 + 1.738^{-11}s^3 + 6.938^{-8}s^2 + 10.92^{-5}s + 0.06435} * 32.8$$

- When $K=0.550$:

$$Gk1 = -\frac{2.804^{-12}s^3 + 2.477^{-9}s^2 + 8.868^{-5}s + 0.04704}{9.531^{-20}s^5 + 2.134^{-15}s^4 + 6.492^{-12}s^3 + 6.673^{-8}s^2 + 8.901^{-5}s + 0.04704} * 32.8$$

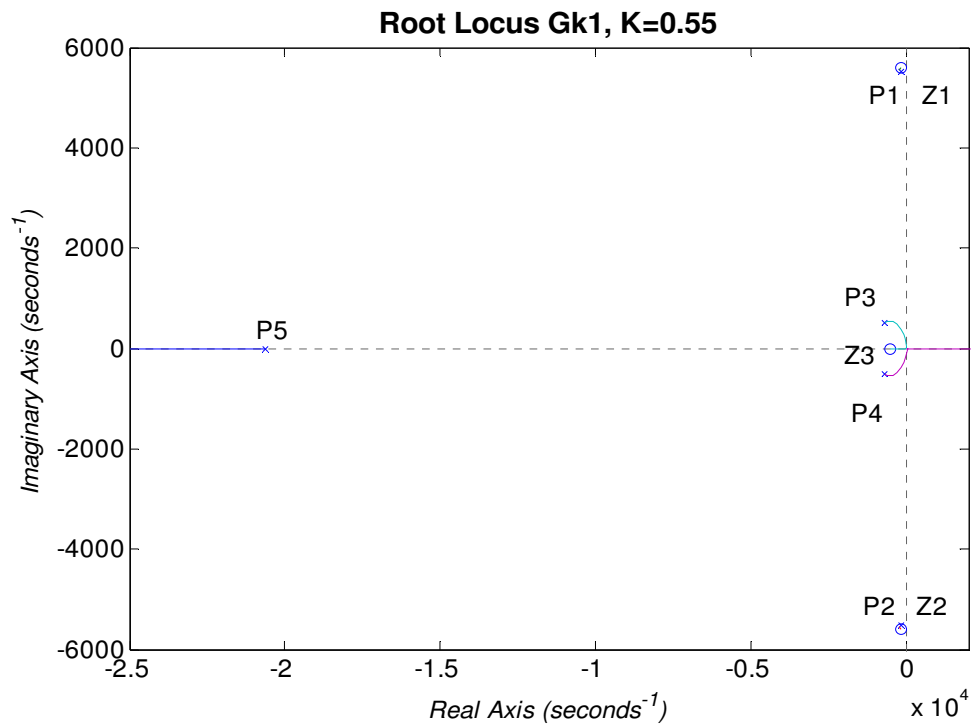
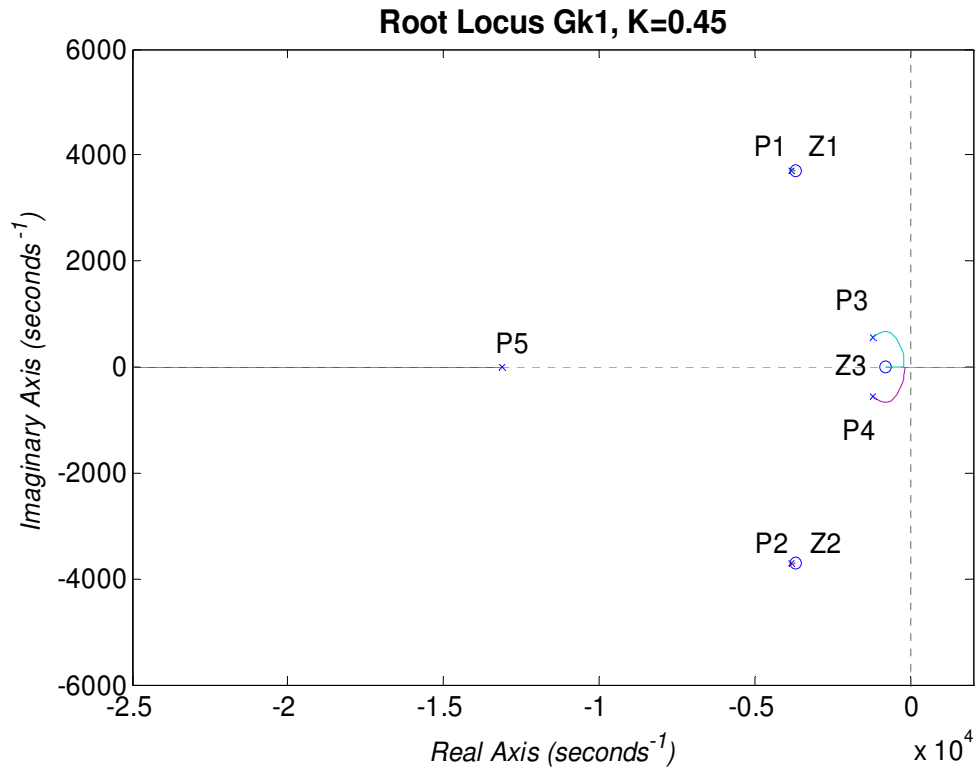


Figure 4.7 Transfer function Gk1 and its pole-zero location plots for different K

- When $K=0.450$

$$Gk2 = \frac{2.804^{-12}s^3 + 4.227^{-8}s^2 + 7.638^{-5}s + 0.06435}{9.531^{-20}s^5 + 2.218^{-15}s^4 + 1.738^{-11}s^3 + 6.938^{-8}s^2 + 0.0001092s + 0.06435} * 32.8$$

- When $K=0.550$

$$Gk2 = \frac{2.804^{-12}s^3 + 5.996^{-8}s^2 + 4.579^{-5}s + 0.04704}{9.531^{-20}s^5 + 2.134^{-15}s^4 + 6.492^{-12}s^3 + 6.673^{-8}s^2 + 8.901^{-5}s + 0.04704} * 32.8$$

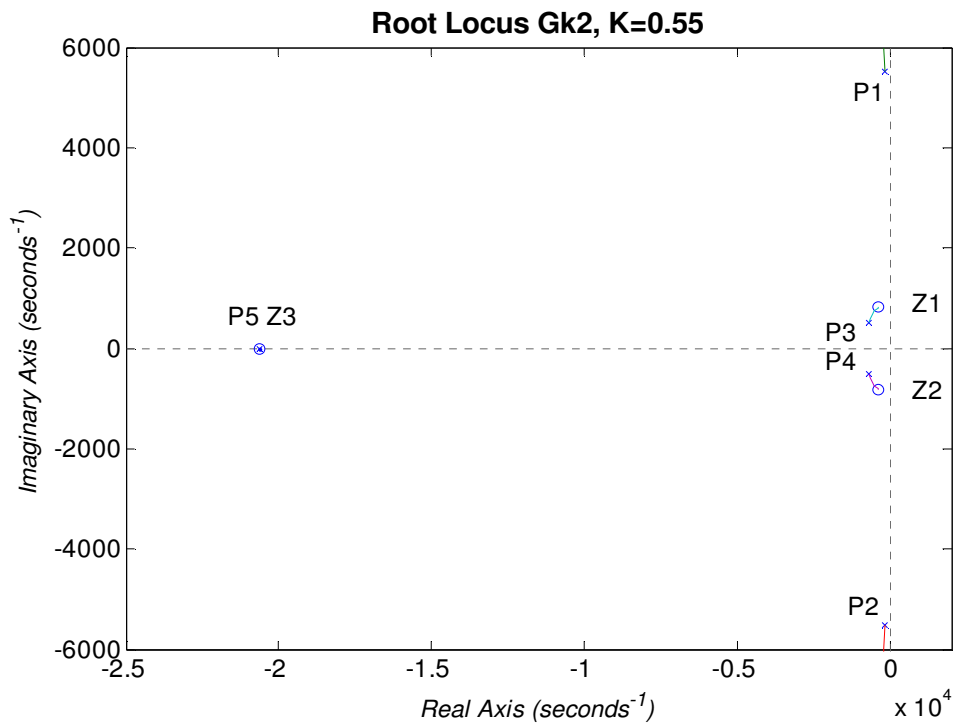
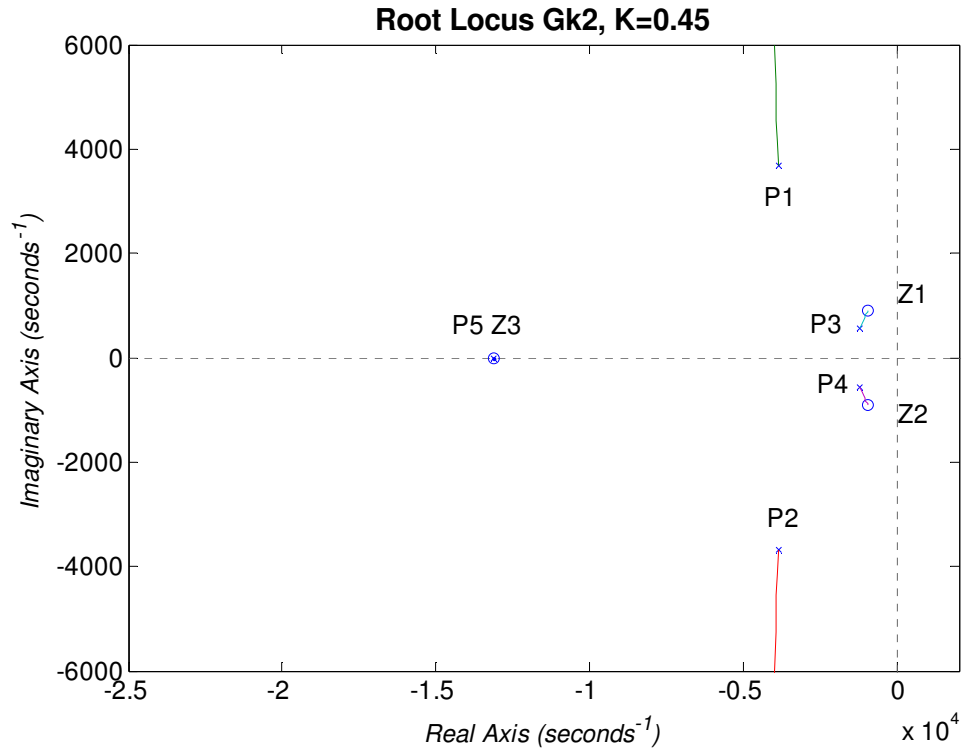


Figure 4.8 Transfer function Gk2 and its pole-zero location plots for different K

Figure 4.9 shows the responses of terminal voltage V_T , which is the sum of V_{PV1} and V_{PV2} . Its steady state value after each \hat{k} change is almost the same, though the transient response resembles that of V_{PV2} in response to each $\hat{k} = 0.025$ step change, and the advance towards a non-minimum phase characteristics are clearly shown. This is because the operating points for PV_1 and PV_2 , in the narrow range of $K=0.475$ to 0.55 , vary in opposite directions as shown in Figure 4.2. Hence, as K changes from 0.475 to 0.55 , V_{PV1} decreases from 18 V down to 13.8 V, while V_{PV2} increases from around 14.8 V to near 19 V. As expected their sum approximates to the steady state value.

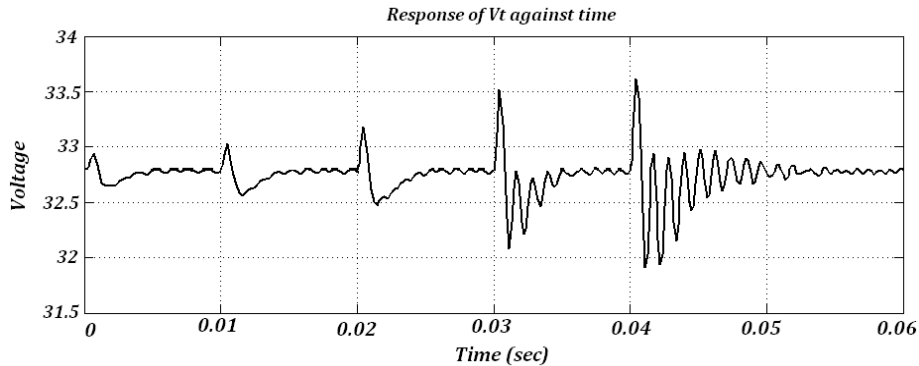


Figure 4.9 Step Response of V_T with different K values

Simulation study of this system using MATLAB/SIMULINK under the same step changes of k has been performed, and the responses for both V_{PV1} and V_{PV2} are shown in Figure 4.10. Here it can be seen the same complementary feature of V_{pv1} and V_{PV2} , and that their sum V_T is maintained almost constant after each \hat{k} perturbation. The oscillatory features of V_{PV2} and V_{PV1} at $K=0.575$ are also shown, though V_{PV2} is not as underdamped as that in Figure 4.4, V_{PV1} is more oscillatory than that shown in Figure 4.3. These differences are rooted in the simplification of transfer functions G_{k1} and G_{k2} . In particular the values of resistances R_{PV1} and R_{PV2} are only approximated at each operating point, rather than being the continuous variable dV/dI .

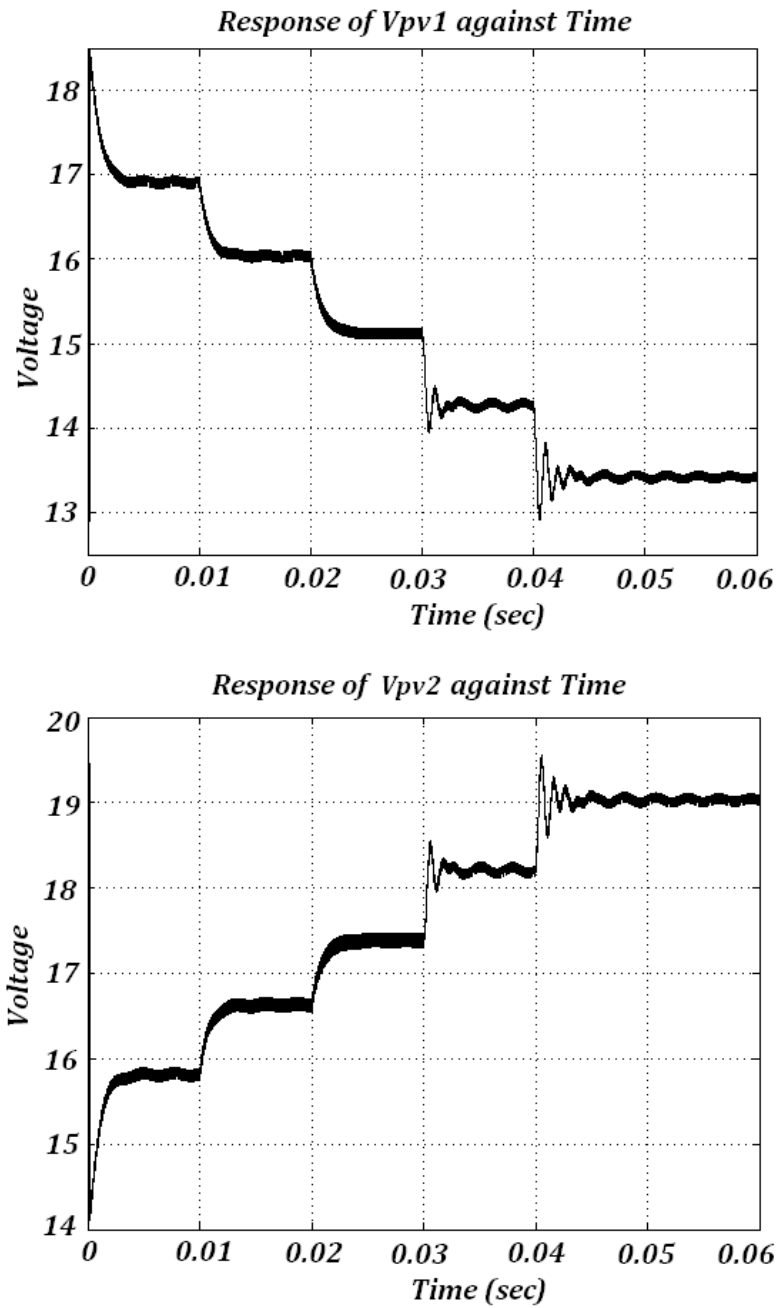


Figure 4.10 MATLAB/SIMULINK simulation of PV-Cuk Converter system step response of V_{PV1} and step response of V_{PV2}

4.5 Summary & conclusions

In this chapter presented the derivation of transfer functions of the solar modules PV_1 and PV_2 voltages to the change of duty ratio for a system consisting of a bi-directional Ćuk converter with two PV panels in the case where there is a higher level of irradiation over PV_1 in relation with PV_2 . Step and frequency response tests of the transfer functions were performed. The results show that the voltages across two panels are complementary under uneven irradiation conditions. Due to the nonlinear resistance of the PV panel, the dynamics of the PV panel receiving less light is under-damped and become more oscillatory as duty increases beyond 0.550. They also show minimum phase characteristics as far as the operation point in the PV panels is near the MPP region. The transfer function step responses are compared with that produced by the MATLAB/SIMULINK simulation. The similarities and causes of discrepancies were stated.

Chapter 5

Controlling an Integrated Ćuk Converter

The Bidirectional Ćuk Converter is presented as a solution to the “partial shading issue” of the solar modules. This chapter investigates the control schemes for an integrated Ćuk-Converter and PV-panel module. This involves testing the configuration in open loop conditions and comparing the measured results with the chained PV modules with their respective bypass diodes. This will give the information on the ranges where the power reduction is lowest and highest. Furthermore, a PV model MPPT is developed and contrasted with the very well known Perturb & Observe algorithm [5] implemented by simulation in closed loop system. The software platform is MATLAB Simulink, using the “SimPowerSystem” Toolbox. Simulation of photovoltaic panels is done with an S-Function script developed in an M-File listed under Appendix C.

5.1 Open Loop Test

Before developing the closed-loop control scheme for the configuration of Integrated Ćuk-Converter and PV modules, open loop tests for this configuration, supplying firstly an R-load and then a DC Bus with an R-load are performed. These tests are also performed on the configuration of two serially connected solar modules with their respective bypass diodes. Comparison of the test results are given. These tests are performed in MATLAB/Simulink environment. Photovoltaic panels used in the tests are rated with an I_{sc} of 3 amperes, 20 volts in V_{oc} and the maximum power value under standard test condition of 1000 W/m^2 , 25°C is 50 watts.

5.1.1 Resistive load

5.1.1.1 Solar Modules with Bypass Diodes

This open loop test of PV panels with bypass diodes involves wiring the two PV panels in parallel with their respective diodes and connecting a load at their terminals as shown in Figure 5.1. The load resistor is set to 20Ω holding the operation point in the P-V Curve at 100 watts in total when both PV panels are being irradiated at 100% of light levels. Moreover, changes of the irradiation of the PV_2 are made by dimming the lights from 100% to 10% in constant step of 10%.

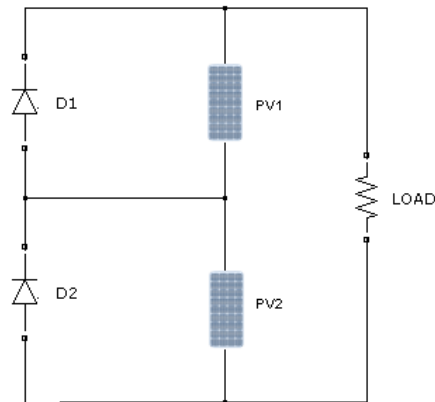


Figure 5.1 PV Panels with bypass diodes and load

The measurements listed in Table 5-1 show the light levels on PV_1 and PV_2 , the voltage across their respective terminals and terminal current, voltage and power produced by the two panels. It can be seen that when both panels are under equal light levels the total output voltage is the sum of each of them equalling to 33.54V while the output current is 2.99A and total power 100.28 Watts. However, as light levels become different, i.e. that for PV_1 is still 100% but that for PV_2 is reduced from 100% down to 40%, the total output current and power drop steadily for each step reduction of light, from 2.99A down to 1.28A and 100.28W down to 44.07W. The voltage for each panel does not differ much; the maximum difference is only

about 2V; hence the terminal voltage is still maintained at 34.43V. This indicates that PV₂ bypass diode is not turned on. Thus the power reduction is due to the increase of PV₂ internal resistance caused by partial shading. However when light level is down to G=30%, PV₂ bypass diode switches on; hence the voltage across PV₂ is measured as -0.7V. The terminal voltage drops down to 16.8V and the output power is also down to low 24W due to that PV₂ is not generating power anymore. It is possible to adjust the load resistance in order to increase output power since the irradiation on PV₁ is still at 100%.

G ₁ (%)	G ₂ (%)	V _{pv1} (V)	V _{pv2} (V)	V _T (V)	I _T (A)	P _T (W)
100	100	17.32	16.21	33.54	2.99	100.28
100	90	17.04	16.07	33.11	2.95	97.67
100	80	16.94	15.68	32.62	2.79	91.01
100	70	17.26	15.54	32.83	2.32	76.17
100	60	17.80	15.84	33.66	1.96	65.97
100	50	18.21	16.43	34.65	1.54	53.36
100	40	18.23	16.20	34.43	1.28	44.07
100	30	17.50	-0.70	16.81	1.43	24.04
100	20	16.98	-0.77	16.22	1.22	19.79
100	10	16.52	-0.81	15.73	1.03	16.20

Table 5-1 Bypass Diode Power Chart

5.1.1.2 Bidirectional Ćuk Converter + PV + Resistive Load

In this test, a Bidirectional Ćuk Converter is wired to two PV panels connected in series and supplying also the same load resistor at the terminal as above. The circuit diagram is as shown in Figure 5.2. Similar to the previous test the light level on PV₁ is held at 100% throughout while that on PV₂ performs step down changes at 10% each time.

This pattern of light level mismatch where PV_1 has a higher irradiation level than PV_2 leads to switches S_1 and D_2 being active as discussed in Chapter 3. For open loop test, for each step reduction of light level the duty ratio for S_1 is manually tuned in order to obtain the corresponding maximum power point.

The measured results for this test are shown in Table 5-2.

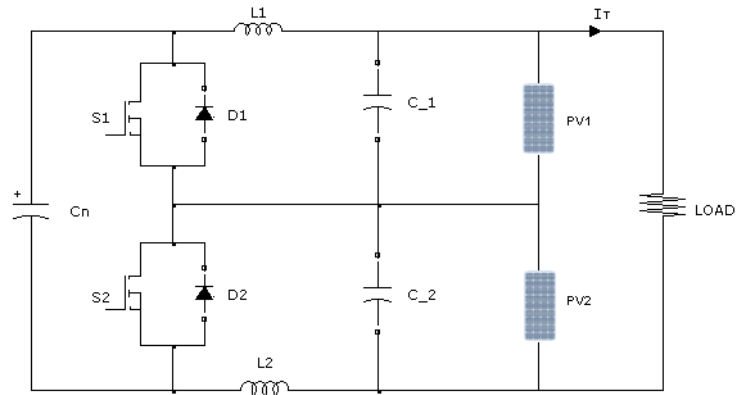


Figure 5.2 Bidirectional Ćuk Converter with resistive load

When PV_1 and PV_2 are under the same irradiation levels, switches S_1 and S_2 are deactivated by grounding S_1 and S_2 's respective gate-drive terminals to prevent any spurious firing. The total voltage is measured at 32.74V, and the output power is 98.55W. At the moment when G_2 decreases, S_1 starts working, thus dictating PV_1 as the input of the converter and PV_2 the output. With each step down of the irradiation level on PV_2 , a reduction of current and consequently the output power is recorded as shown in Table 5-2. The voltage changes for both panels are negligible, due to at each measurement the panels are operating at the voltage levels corresponding to their respective maximum power point.

$G_1(\%)$	$G_2(\%)$	$V_{pv1}(V)$	$V_{pv2}(V)$	$V_T(V)$	$I_T(A)$	$P_T(W)$
100	100	16.43	16.31	32.74	3.01	98.55
100	90	15.50	16.23	31.73	2.85	90.43
100	80	16.58	16.15	32.73	2.67	87.39
100	70	16.43	16.11	32.54	2.54	82.65
100	60	16.40	16.11	32.51	2.27	73.80
100	50	16.38	16.11	32.49	2.05	66.60
100	40	16.54	16.09	32.63	1.86	60.69
100	30	16.64	15.92	32.56	1.53	49.82
100	20	16.50	14.98	31.48	1.45	45.65
100	10	15.91	15.58	31.49	1.2	37.79

Table 5-2 PV Integrated Ćuk Converter Power Chart

5.1.1.3 Comparison

Table 5-3 contrasts the results showing the measured power values generated by the panel using bypass diodes in 5.1.1.1 and that using the integrated Ćuk converter in 5.1.1.2. under the same light levels. Their differences and percentage gains are also given in the last two columns. It can be seen that when there is no light level mismatch, both configurations produce similar levels of output power, due to that neither the bypass diode nor the converter is active. Moreover, when light mismatch occurs, the Ćuk converter starts to work, and there is a drop in the power produced due to the converter losses, but the bypass diode is in reverse bias and there are no losses of passive components. The significant power change occurs when the irradiation in the second solar module reaches 70%. As is shown in the Table, the integrated Ćuk converter and PV module configuration produces significantly more power than that with bypass diodes and this power gain increases at each step reduction of PV_2 light level, reaching the maximum more than 50%. This trend of steady and significant gain of output power demonstrates

the benefit of using the integrated Ćuk converter and PV-panel module scheme under uneven light level operation conditions.

Bypass Diode P(W)	Integrated Converter P(W)	Gain ΔP (W)	Gain (%)
100.28	98.55	-1.74	-1.71%
97.67	90.43	-7.24	-6.71%
91.01	87.39	-3.62	-3.48%
76.17	82.65	6.49	7.04%
65.97	73.80	7.82	8.75%
53.36	66.60	13.24	16.53%
44.07	60.69	16.62	22.89%
24.04	49.82	25.78	53.42%
19.79	45.65	25.86	59.65%
16.20	37.79	21.59	50.35%

Table 5-3 Comparison of power produced

Figure 5.3 shows a plot of power differences under different light ratios G_2/G_1 . It is clear from the plot the lower the light level mismatching, the lower the power gain for the integrated converter and PV module structure. In fact, it may cause negative power gain due to converter losses. However, as the mismatching is incremented, the power gain ΔP rises rapidly. Such improvement in the power generated by the PV panels can be appreciated when the difference of lighting is greater than 30% or when the lighting ratio G_2/G_1 is lower than 0.7. In addition, it is observed the amount of power gain in each light mismatching case is much higher than the power losses caused by the Ćuk converter when light differences are low.

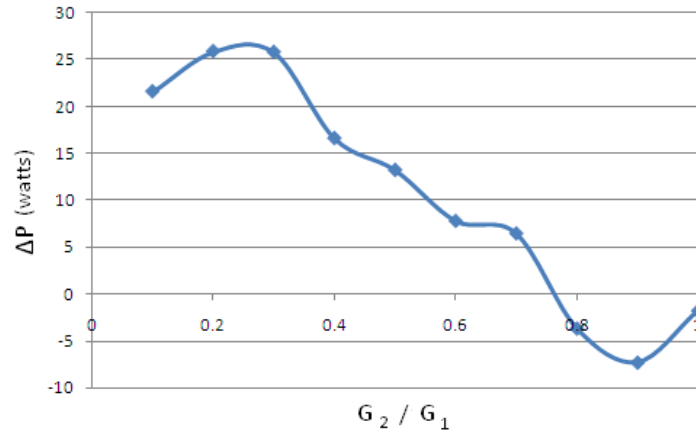


Figure 5.3 Gain ΔP Power chart

5.1.2 DC Bus connected to the system

This test compares the power generated by the above two PV system configurations under the condition that they are now, respectively, supplying power to a constant DC bus through a terminal boost converter which is used as a power conditioner. The configuration of this test system is as shown in Figure 5.4. A 40Ω resistor load is connected on the DC-bus. The details of the terminal boost converter are given in Appendix D, and the DC-Bus voltage is maintained at 60 volts by a stabilised DC power supply, hence the current demanded by the load is always 1.5A. The Boost converter should enable its output voltage reaching that of the level of DC Bus. In the event that the solar modules do not generate enough power hence the output current is low, the DC power supply will then feed to the load the remaining current needed.

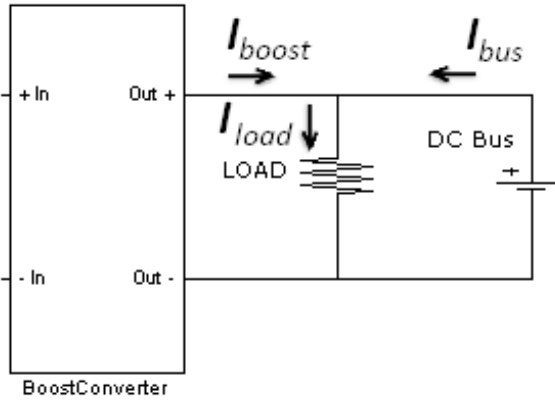


Figure 5.4 Boost converter and DC Bus

5.1.2.1 Solar modules with bypass diode and Boost converter

The open loop system of two PV panels connecting to a DC bus with a load, shown in Figure 5.5, is firstly tested to search for the maximum power points at any given irradiation levels. The light levels and their variation steps are set the same as that described in Section 5.1.1. For each test, the duty ratio for the Boost converter PWM control signal is carefully tuned manually until the maximum power extraction is obtained from both panels.

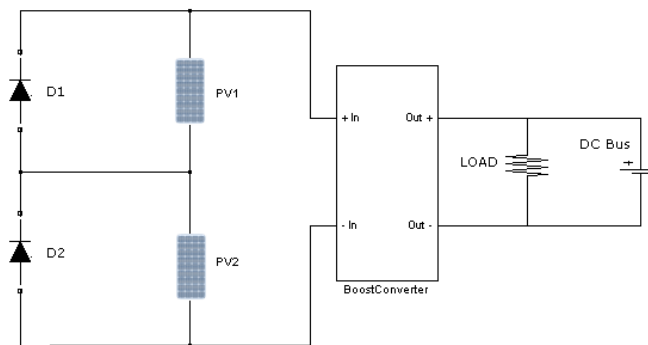


Figure 5.5 Integrated bypass diode with DC Bus

Table 5-4 presents a listing of measured results in the order as that given in Table 5-1. The patterns of output voltage, current and power variations for each light

condition are similar to the previous case when the same PV system is supplying a resistive load alone as shown in Table 5-1. However it can be noted that when G_2 is higher than 30%, and the bypass diode D_2 is still reverse biased, the voltages are similar, but power losses are higher compared to that in Table 5-1 hence the total output power is lower for each light level. This is due to the losses caused by the boost converter.

The improvement in produced power is seen significant when irradiation level G_2 drops down to 30%, hence D_2 conducts. Under this condition, the output power is 33.15 W, about 10 W higher than the same configuration listed in Table 5-1. This increment occurs because the boost converter enables flexible adjustment of duty ratio so that PV_1 operates at its maximum power point. This situation extends to when G_2 falls further down to 10%.

$G_1(\%)$	$G_2(\%)$	$V_{pv_1}(V)$	$V_{pv_2}(V)$	$V_T(V)$	$I_T(A)$	$P_T(W)$
100	100	17.89	17.30	35.19	2.66	93.61
100	90	17.64	16.89	34.53	2.62	90.47
100	80	17.68	15.42	33.10	2.42	80.10
100	70	17.83	14.46	32.29	2.15	69.42
100	60	18.02	14.08	32.10	1.74	55.85
100	50	18.21	13.74	31.95	1.41	45.05
100	40	18.31	13.54	31.85	1.24	39.49
100	30	17.59	-0.93	16.66	1.99	33.15
100	20	17.64	-1.01	16.65	1.92	31.81
100	10	17.65	-1.08	16.57	1.87	30.99

Table 5-4 Power chart of Integrated bypass diode with DC bus

5.1.2.2 1 Bidirectional Ćuk Converter + PV + Boost Converter + DC Bus

The same open loop test was carried out for Integrated Bidirectional Ćuk Converter and PV-panel Module as shown in Figure 5.6. Using the same light levels and switching scheme previously described in chapter 3, with the difference that now there are 2 switches needed to be tuned manually, the switches S_1 from the Ćuk converter and S_T at the terminal boost converter. The test starts with the two solar panels irradiated at 100%. At this stage, switch S_1 is connected to ground since there is no light mismatching. Furthermore, the duty ratio applied to switch S_T of the boost converter is tuned manually until the maximum power point is obtained. Subsequently, the light level G_2 is dimmed by 10% per step and switch S_1 starts to be tuned until the integrated converter delivers the maximum power. After this adjustment, the switch S_T is also tuned to reach the overall maximum power point. This process is applied to all the lighting steps until G_2 reaches 10%.

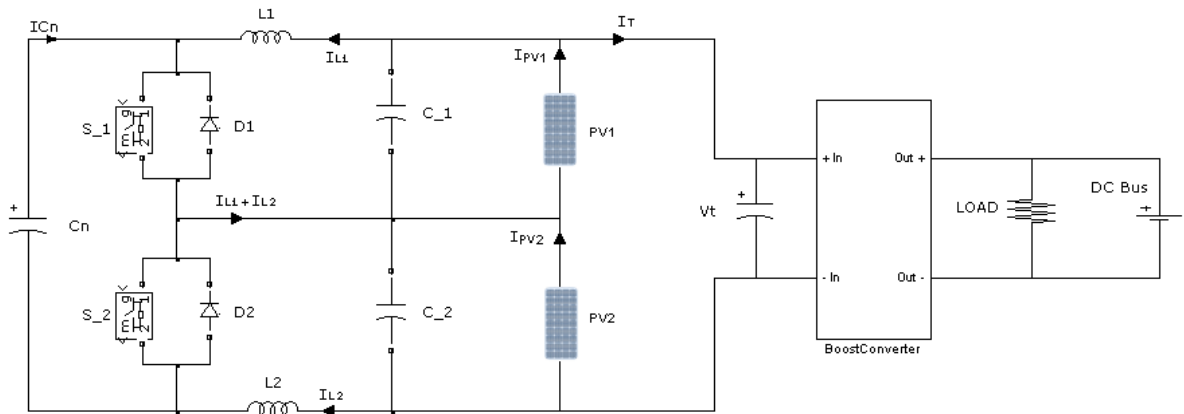


Figure 5.6 Simulink setup of 2 PV Panels with Ćuk Converter with a Boost Converter at the output, a resistive load and DC Bus

Table 5-5 lists the measurements readings taken from a test when light level over the solar module PV_2 is reduced down from 100% to 10%, and corresponding manual adjustment of the two converter duty ratios is performed. At the first glance, the data shows the voltages of the two PV panels are held almost at constant

levels by the Ćuk converter, but the output current reduces steadily as G_2 drops and so does the total generated power.

$G_1(\%)$	$G_2(\%)$	$V_{pv1}(V)$	$V_{pv2}(V)$	$V_T(V)$	$I_T(A)$	$P_T(W)$
100	100	16.62	16.22	32.84	2.73	89.65
100	90	16.56	16.20	32.76	2.67	87.47
100	80	16.46	16.18	32.64	2.53	82.58
100	70	16.44	16.02	32.46	2.29	74.33
100	60	16.64	16.00	32.64	2.13	69.52
100	50	16.30	15.94	32.24	1.92	61.90
100	40	16.34	15.94	32.28	1.80	58.10
100	30	16.43	15.96	32.39	1.48	47.94
100	20	16.50	15.99	32.49	1.28	41.59
100	10	16.57	15.83	32.40	1.10	35.64

Table 5-5 Power chart of integrated converter with DC Bus

5.1.2.3 Comparison

The results of the two topologies under the same test conditions are contrasted as shown in Table 5-6. Clearly the integrated Ćuk bi-directional converter topology shows the same pattern of power gain as that presented in subsection 5.1.1.3 when the irradiation level G_2 is below 90%. However the slightly lower total power of this scheme occurs when G_2 is 100% and 90%, which attributes to converter losses.

Bypass Diode P(W)	Integrated Converter P(W)	Gain $\Delta P(W)$	Gain (%)
93.61	89.65	-3.96	-4.42
90.47	87.47	-3.00	-3.43
80.10	82.58	2.48	3.00
69.42	74.33	4.91	6.61
55.85	69.52	13.67	19.66
45.05	61.90	16.85	27.22
39.49	58.10	18.61	32.03
33.15	47.94	14.79	30.85
35.81	41.59	5.78	13.90
30.99	35.64	4.65	13.05

Table 5-6 Power Gain Chart bypass diode and integrated converter

Figure 5.7 shows a plot of power gain variation of the Integrated Ćuk Converter structure over the conventional bypass diode topology. As can be seen clearly, negative power gain only happens when light mismatching is insignificant, shown in the right hand side of the plot when $G2/G1$ is nearly 1. As $G2$ reduces steadily, hence $G2/G1$ becomes smaller, power gain increases rapidly. The maximum power gain is 18.61 Watts, obtained when $G2/G1$ is about 0.45. This shows that the integrated Ćuk converter structure can deliver power as much as 32% higher than that of a bypass diode configuration.

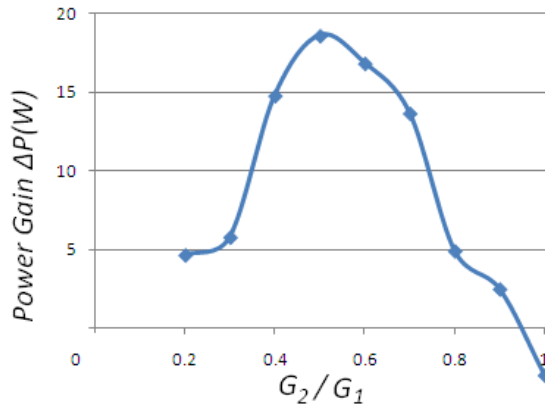


Figure 5.7 Power gain using the Integrated Converter

The above presented open loop test results and comparisons lead to the conclusion that the integrated bi-directional Ćuk converter photovoltaic modules enable higher power generation hence giving higher efficiency than just the bypass diode-based solution. Moreover, an additional feature within the switching scheme of the Bidirectional Ćuk converter is present by analyzing the open loop system measurements. When the irradiation relation G_2/G_1 (or G_1/G_2 , depending on which one is higher) is greater than 0.7, light mismatching is insignificant, the PWM signals for S_1 and S_2 must be set to zero. Consequently diodes D_1 and D_2 will function temporally as bypass diodes within the Bidirectional Ćuk Converter. However, when irradiation ratio is lower than 0.7, the Ćuk Converter should be enabled working, hence can be controlled to achieve the maximum power generation.

5.1.3 A comparison of bypass diode and integrated converter with three solar modules

The same test as above is now performed on PV system having three solar modules connected in series. Figure 5.8 presents the Simulink circuit model used with bypass diodes connected in parallel with each panel wired in series.

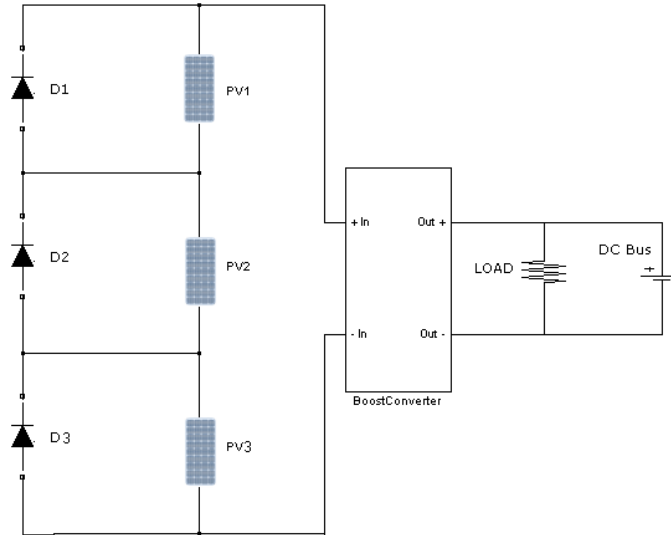


Figure 5.8 Three Panels with Bypass Diode

Now the system operates under three different levels of irradiation labelled G_1 , G_2 and G_3 , corresponding to the light irradiated on the PV panels PV_1 , PV_2 and PV_3 respectively, emulating different shading levels over the panels.

The same measurements as that in the previous tests are taken and listed in Table 5-7. The PV system with bypass diodes shows the same behaviours as that of the previous tests under similar operating conditions. As shown in Table 5-7 when a PV panel's light level is higher than 40% (rows 1, 4, 5), its corresponding bypass diode is reverse biased and the output voltage is lower than the ones with higher light levels. However if the irradiation level odd one panel is about 40% or lower (rows 2 and 3) it is corresponding diode may conduct causing it to stop generating any power, hence a significant output power reduction occurs.

$G_1(\%)$	$G_2(\%)$	$G_3(\%)$	$V_{pv_1}(V)$	$V_{pv_2}(V)$	$V_{pv_3}(V)$	$V_T(V)$	$I_T(A)$	$P_T(W)$
100	80	100	17.60	14.94	17.60	50.14	2.78	139.39
100	80	40	17.75	15.61	-0.80	32.56	2.43	79.12
100	20	50	18.89	-0.80	14.83	32.92	1.55	51.03
60	40	100	17.49	13.62	19.12	50.23	1.27	63.79
70	100	50	17.52	18.85	14.03	50.40	1.54	77.62

Table 5-7 Three Panel with Bypass Diode

When using integrated converters, the topology expands by incorporating an additional bidirectional Ćuk Converter as shown in Figure 5.9, hence new rules of switching mode scheme for this topology was presented in Table 3-2. The proportion of light irradiated upon each PV panel is organized such in a way to include all different levels of shading.

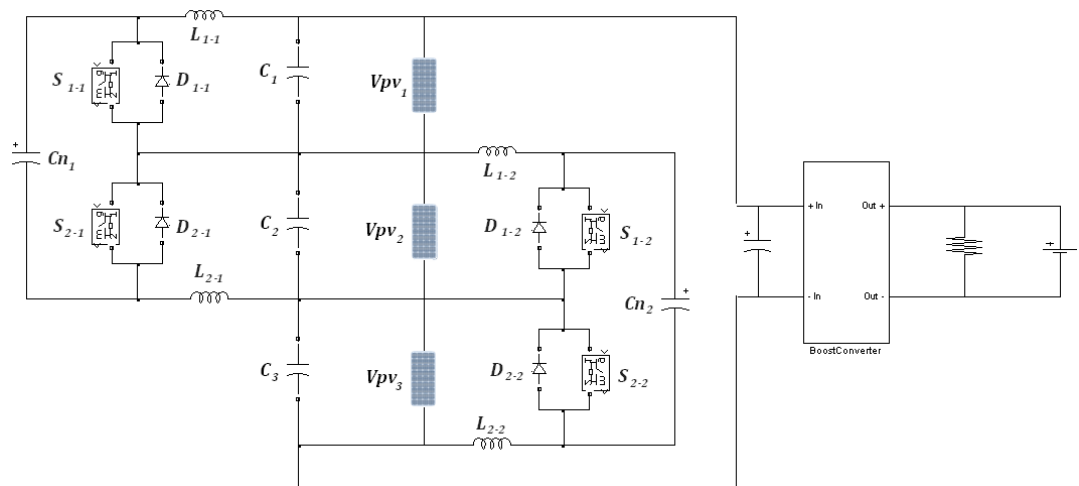


Figure 5.9 Three PV panels with two Integrated Bidirectional Ćuk Converters

The test was carried out by manually tuning the PWM signals for each of the two inner converters and one outer boost converter. Using the same protocol with the “two PV panel case”, each of the three solar panels achieves an individual

maximum power point which is listed under Table 5-8. It is of importance to note from the results that the terminal voltage is maintained relatively constant in all different irradiation levels whereas the current is independent of each panel; this is due to the small region where the maximum power point is found, in this particular case from 13 to 17 volts under an irradiation of 20% to 100% (see Figure 2.10).

$G_1(\%)$	$G_2(\%)$	$G_3(\%)$	$V_{pv1}(V)$	$V_{pv2}(V)$	$V_{pv3}(V)$	$V_T(V)$	$I_T(A)$	$P_T(W)$
100	80	100	16.52	15.38	16.52	48.42	2.72	131.70
100	80	40	17.07	15.94	14.13	47.14	2.14	100.88
100	20	50	17.20	13.90	14.40	45.50	1.67	75.99
60	40	100	14.70	14.92	17.14	46.76	1.94	90.71
70	100	50	15.49	16.82	14.94	47.25	2.16	102.06

Table 5-8 Three PV panels with Bidirectional Ćuk Converter

Contrasting the measured values in tables Table 5-7 and Table 5-8, the power values and differences in both systems under the five different light level combinations are listed in Table 5-9. It can be seen that, as expected, the integrated converter structure gives negative power gains due to converter losses when the differences on irradiance levels on each panel are insignificantly small. As the shadowing level increases, the configuration with bypass diodes generates much lower power comparing to its counterpart. The maximum power gain for the latter can be seen as high as nearly 49%.

Bypass Diode P(W)	2 Integrated Converter P(W)	Gain $\Delta P(W)$	Gain (%)
139.39	131.70	-7.69	-5.51%
79.12	100.88	21.76	27.50%
51.03	75.99	24.96	48.91%
63.79	90.71	26.92	42.20%
77.62	102.06	24.44	31.49%

Table 5-9 Contrast of two methods with three PV Panels

Reaching the same conclusion as that from the previous test comparisons, it is clear that an integrated bi-directional Ćuk converter with PV-panel module provides outstanding power gain over the common “bypass diode” solution. However, the circuit structure, the switching and control scheme are complicated, and the level of complexity increases with the numbers of PV modules and converters.

5.2 Closed loop Control of Integrated Converter PV modules

Having shown the advantages offered by the integrated Ćuk converter with PV module system in open loop condition, closed loop control schemes should be developed to enable such a system achieving the maximum power generation under all shading conditions automatically and rapidly. The development has been carried out on the PV system shown in Figure 5.6 where two PV panels are connected in series, and one bidirectional Ćuk converter is wired between them. A terminal boost converter is also used as the power conditioner interfacing the PV system with the DC bus supplying a resistive load.

The algorithms considered are the well-known Perturb & Observe method [93] and the On-line Model based Maximum Power Point Tracker proposed in the next subsection. These two methods all require on-line measurements of Voltage, Current, Irradiation and Temperature of all solar panels. Each of the measured

signals needs to be processed in order to determine the correct control actions and calculate duty ratio values for the converters. Since this system consists of two converters, the inner Ćuk converter and the outer boost converter, the sampling rate in each of the converters is different due to their respective time response. The sampling rate for those signals responsible for determining the duty ratio of the inner converter must be faster than those for the outer converter. Thus in this system for every ten operations of data sampling and control signal calculation for Ćuk converter the same operation for the boost converter only happens once. This allows the Ćuk Converter locating the individual PV module's maximum power point before adjusting the Boost converter duty ratio for controlling the total system.

- Maximum power point tracking algorithm

Over the years, many authors have proposed different maximum power point trackers in order to harness the maximum power from the PV Panels. The authors in [5] have done an exhaustive survey on strategies available, going from elemental algorithms such as Perturb and Observe [93] to complex algorithms like Neural Networks and Fuzzy Logic [92]. Salas [94] classified in three categories the MPPT algorithms, which are:

- a) Indirect control for MPPT
- b) Direct control for MPPT
- c) Artificial intelligence algorithms

Indirect control methods bases in parameters already collected before the evaluation, having a lookup table and configure the system to substitute these values on the algorithm. The major disadvantage of this method is the amount of data and the memory that takes in order to compute the MPP. Parallel to this method is the direct control, which bases the search of the MPP depending on online measurements such as voltage, current, temperature, irradiance. Artificial Intelligence algorithms are vastly used in MPPT research, in particular neural network algorithms are used to calculate the optimal operating point for the system.

Regardless of this, the high complexity and tuning time of the parameters make the method less accessible for practical uses.

Section 2.3.2 explains when the “partial shading” occurs; the P-V Curve could be divided into “n” number of local maximum power points, “n” being the number of PV panels with an irradiance difference connected with bypass diodes. The aim of having an MPPT besides to find the operative point where the power harnessed is the optimal is also to avoid falling in local MPP and find the Global MPP as it shows Figure 2.19.

Curve fitting method is firstly introduced by Veerachary [76] to create a PV model with specs measured from the solar modules. However, the temperature of the material is not considered. Since the temperature factor is such an important atmospheric component for calculate the I-V curve, the terms ΔT and β are introduced into the equation, where β is the temperature coefficient in which the V_{mpp} shifts per $^{\circ}\text{C}$ and ΔT is the difference between the sampled temperature value and the base temperature value for the curve fit in Celsius.

From the I-V curves under different irradiance, the V_{mpp} values of the same temperature are obtained from PV panels in the laboratory mentioned in Chapter 2, and plotted against Irradiance and then a logarithmic linearization of the result is given by a first degree polynomial in equation 5-1. Final V_{mpp} equation with temperature values is presented in equation 5-2.

$$V_{mpp} = 0.7658 * \ln(G) + 11.318 - \beta * (\Delta T)$$

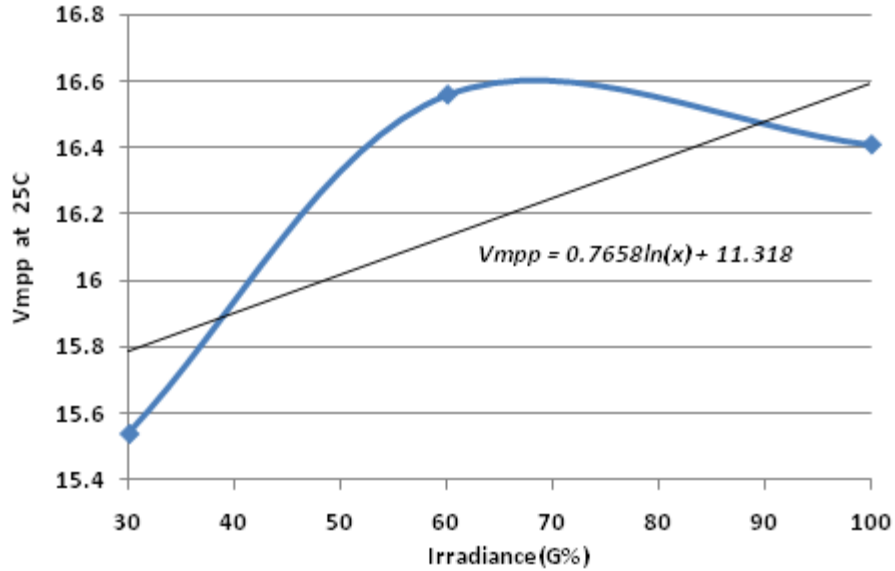


Figure 5.10 First order linearization

$$V_{mpp} = 0.7658 * \ln(G) + 11.318 - 0.06 * (T_{cell} - 25)$$

5-2

In order to verify the MPPT online model a Simulink block under MATLAB environment. The representation of the equation is given in Figure 5.11a. Since the model is directly dependant from Irradiation and Temperature, this will be the two inputs of the system having as output the value of voltage where the maximum power point is located. The value given by the model represents only one PV panel. Under Simulink environment, this model can be manipulated to reproduce the value of “n” number of panels interconnected in series.

Simulation is carried out under different temperature levels and light irradiation. Results in Figure 5.11b represent the value of V_{mpp} that can be compared with I-V curves maximum power point presented in Figure 2.18. The effects of increased temperature over the solar cells were the voltage decrease is present in the results. This particular model is only valid for the experimental panel and under those light conditions previously mentioned, but the model can be tuned for any PV panel with the same process.

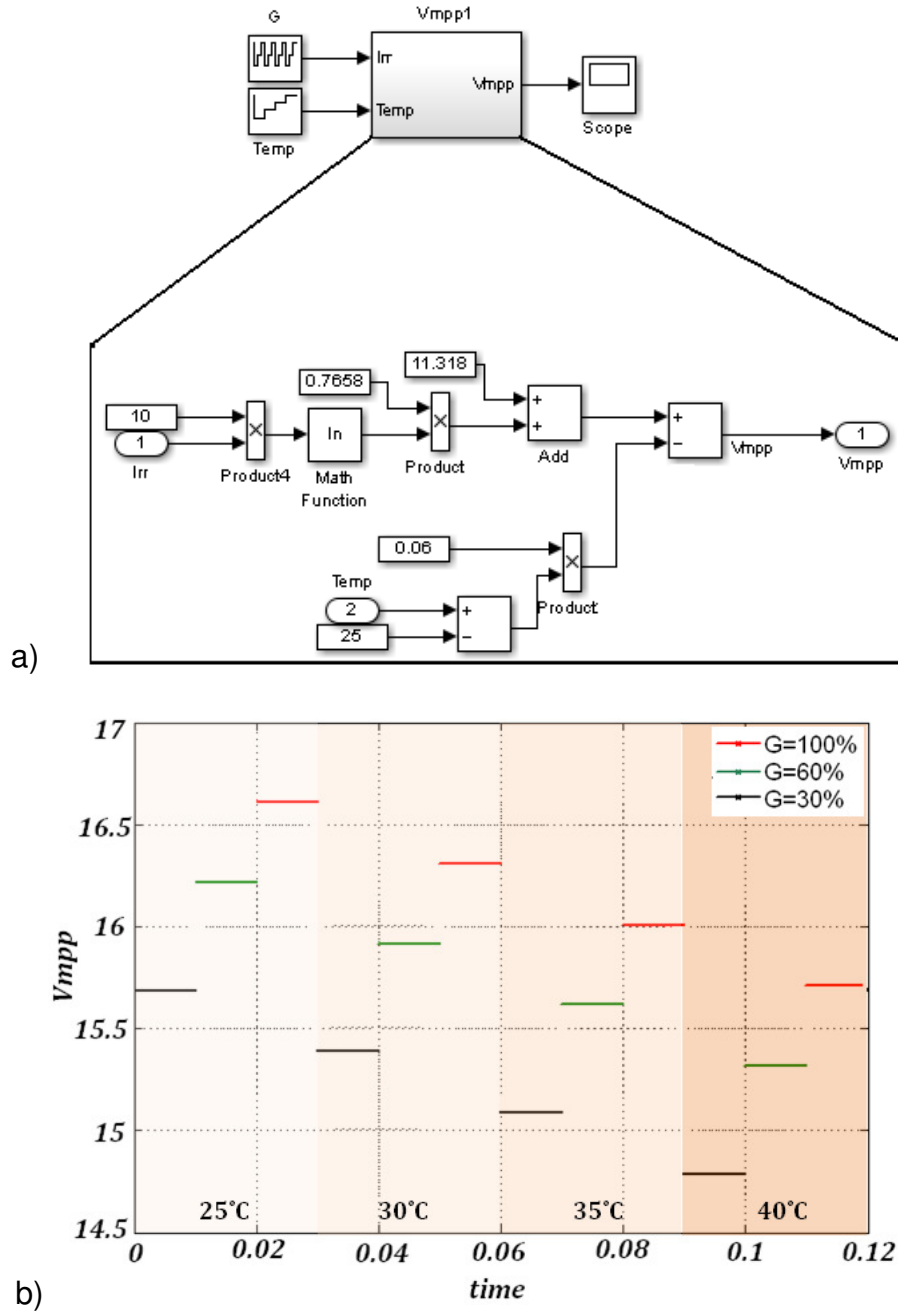


Figure 5.11 Vmpp model simulation

5.2.1 A comparison of two MPPT implemented in closed loop

5.2.1.1 Perturb and Observe in closed loop system

This algorithm is simple. At each sample instant, it measures the PV system generated power at its terminals and compares the measured value with the

previous one. If it is smaller, the algorithm will either increase or decrease the duty ratio by a constant amount set by the user. On the other hand, if the current power is greater than the last sampled value, the algorithm carries on tuning the duty ratio in the same way as the last. This process is continued until the measured power is less than the last one. Details of the P&O algorithm and simulation program used are listed in Appendix E.

When using the P&O algorithm to control the PV system in Figure 5.6, the light levels are set to let irradiation over module PV_2 being 50% while that over module PV_1 at 100%. The results obtained are shown in Figure 5.12 where five plots are given; the terminal voltage, current and power together with the duty ratios for inner and outer converters. As can be seen from these plots, at each sample instant, the duty ratio for the outer boost converter is changed by a constant ± 0.001 , causing the corresponding variations of voltage, current and power. The continuous tuning of duty ratio according to terminal power value has led to the measured parameters of this PV system matching to the ones under the same light pattern of $G_1 = 100\%$ and $G_2 = 50\%$ listed in Table 5-5 at time $t = 0.25\text{sec}$.

Adjustment of duty ratio value for inner converter switch S_1 is also shown in Figure 5.12. Clearly for each variation of switch S_T duty ratio the P&O algorithm tunes that for S_1 many times. Since S_T has a great impact in searching for global optimal power point. Without this delay, the duty ratio in the inner and outer converter would be under a false MPP value. Therefore, the P&O will never reach the individual MPP in each of the modules and the global maximum power point.

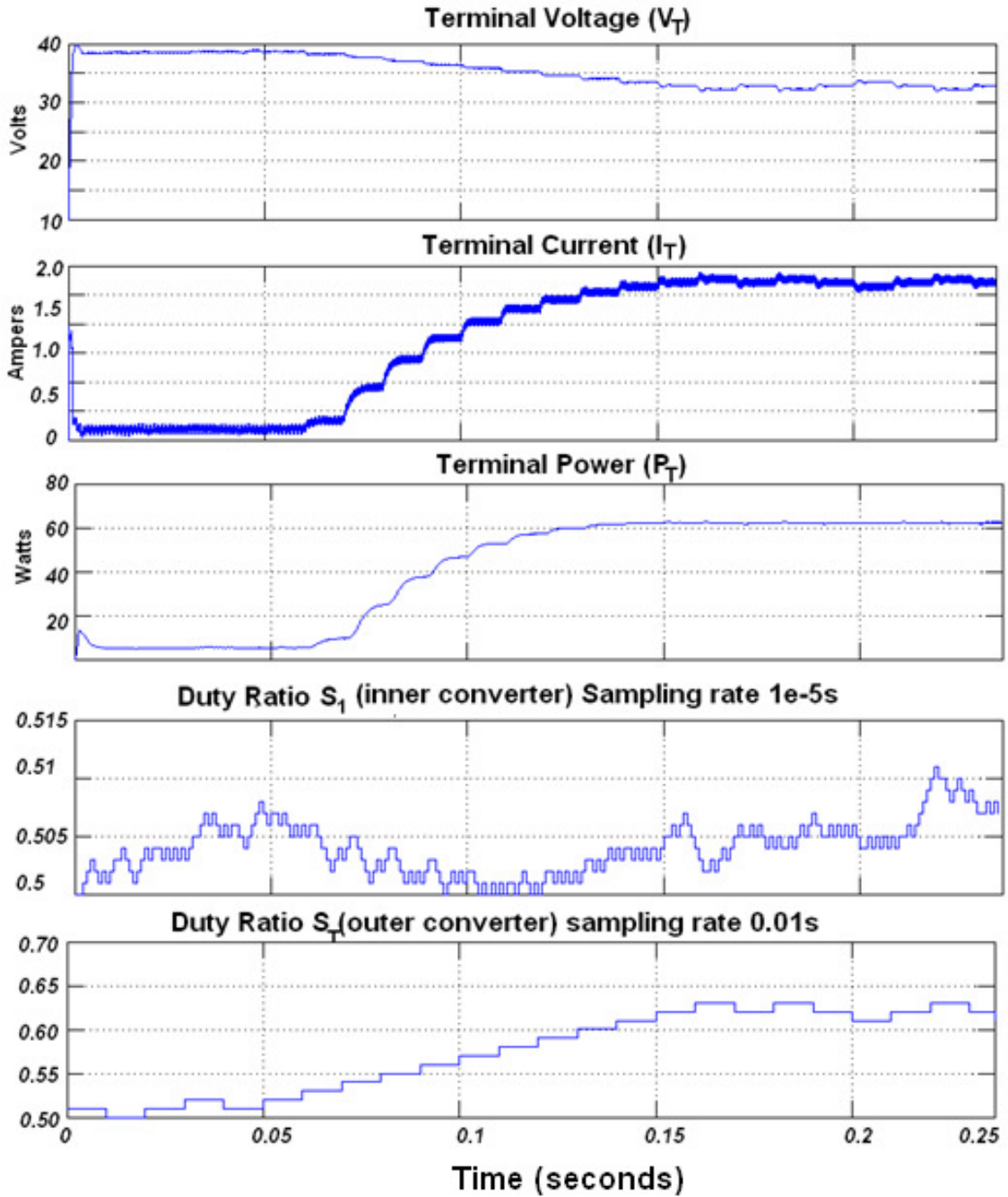


Figure 5.12 Response of P&O during an irradiation mismatch

Using the P&O algorithm, the integrated converter is also able to handle sudden changes of irradiance over the solar modules. The follow test is done to show this effect. By setting the light levels for both PV panels at 100,% initially and letting the P&O finding the MPP by controlling the Boost converter, there is a change made to

the light level over PV_2 going from 100% to 70% at the time of 0.6 sec. Figure 5.12 shows the responses against time of the individual voltage in PV_1 and PV_2 , the terminal voltage V_T , terminal current I_T , the terminal power P_T and the switch S_T change controlled by the P&O.

It can be seen at the start of this test the duty ratio value for S_T is set to 0.5, this setting enables the P&O searching for the MPP faster. The simulation curves show noisy responses initially while the duty ratio is changed by adding a constant 0.001 at each sample instant. When the duty ratio reaches its peak value where the converter is not delivering more energy, the algorithm starts subtracting the constant until the power settles around 88 watts. At time $t=0.3$ seconds, the PV panels are delivering the maximum power corresponding to when both panels are fully irradiated at $G_1=G_2=100\%$. At $t=0.6$ seconds there is a step down in irradiation G_2 . Correspondingly the ongoing algorithm is adjusting the duty ratio searching for the new MPP. Though the measured values show noisy responses (see the graphs in Figure 5.13) in this process, the system approaches a steady state at around the time $t=1.1$ seconds. Power harnessed by the P&O at this time is similar to the ones obtained by the open loop test given in Table 5-5.

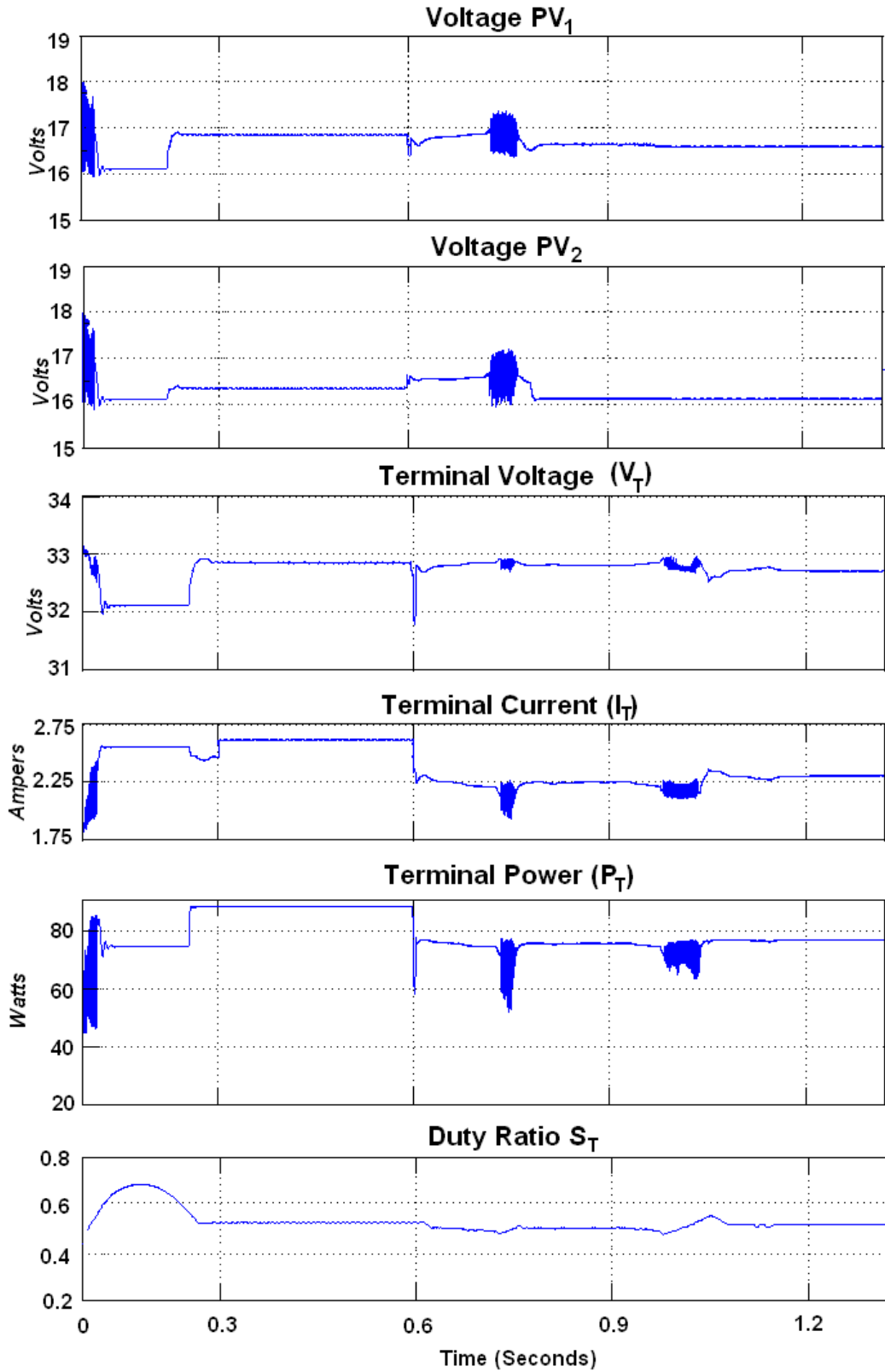


Figure 5.13 Simulation with automatic response

5.2.1.2 Real-Time Model for MPPT

A new algorithm designed by analysis is presented in order to improve the power generated from the PV panels in a Bidirectional Ćuk Converter connected as a bypass DC/DC module integrated. Although, this algorithm is not part of the MPPT algorithms, it is complementary switch scheme to reach a global maximum power point. Firstly, the irradiation on each panel is measured and compared as described in Figure 5.14. Secondly, is compared with the factor $G_{\text{shaded}}/G_{\text{unshaded}} \leq 0.7$ that comes from the irradiation relation mentioned previously. Thirdly, the decision is made of which switch will be working depending upon the irradiation difference. The algorithm is used to control the switches S_1 and S_2 .

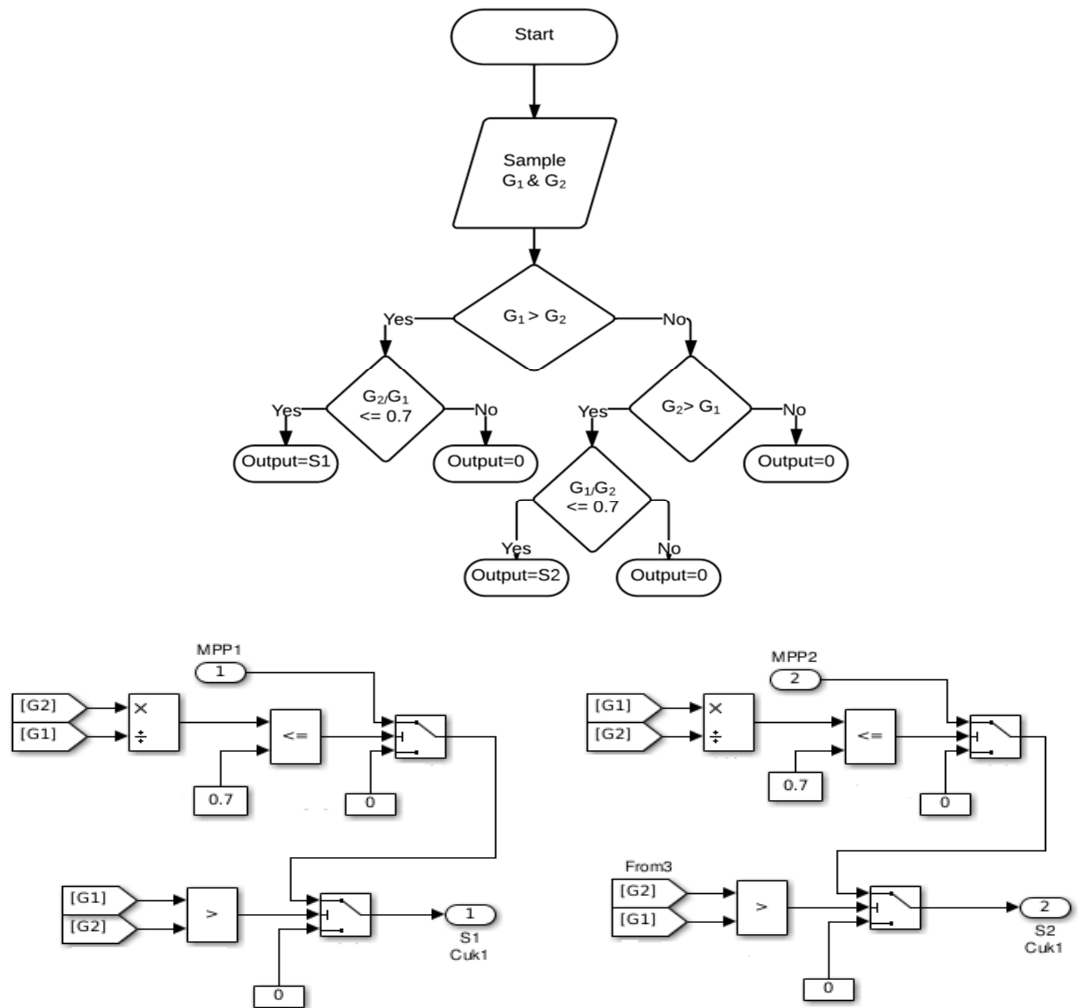


Figure 5.14 Improved switch scheme flowchart and Simulink Models

The maximum power point tracker based in online model as mentioned previously relies on measurements of irradiation and temperature over the PV module. Figure 5.15 shows how those signals are fed into the model equations, and a predicted voltage is obtained as the output labelled V_{mpp_x} , where x is the PV panel number. In this case, the closed loop control scheme is constructed by the model generated reference signal V_{mpp} of each solar module and the measured voltage values from the module output. Signals are then subtracted to create a measured error which are connected by using a P+I controller tuned by Ziegler-Nichols method [95], [96]. The output of the controller is the duty ratio for S_1 or S_2 and S_T .

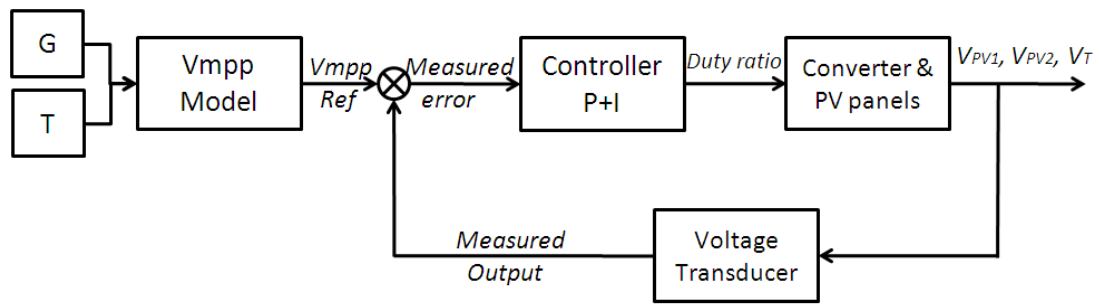


Figure 5.15 Block diagram of the integrated converter in close loop

Converter	Proportional Gain (Kp)	Integral Gain (Ki)
Inner	0.001	4.6
Outer	0.0015	2.952

Table 5-10 P+I controller values

In order to test the dynamic responses of the integrated converter and PV system and the switch scheme, different levels of irradiation are introduced against time. The changes of irradiation in the solar modules over PV_1 and PV_2 activates S_1 or S_2 depending on which irradiation, G_1 or G_2 , is higher whereas S_T is active all

times. Graphic responses of the experiment are provided in Figure 5.16. Measured voltage is represented by a continuous line whereas predicted voltage by the MPPT is drawn by a dashed line.

Simulation starts with $G_1=G_2=100\%$ since there is no mismatching in irradiation, the only active switch at this time is S_T . Terminal voltage holds around 33.6 volts and each PV panel at 16.8 volts, which is the values corresponding to the individual maximum power point voltage. From the time of 0.04 to 0.06 seconds there is a change in G_1 that goes from 100% to 50% shaped as a ramp, emulating the change of irradiation over time on the module. At point "a)" in the middle of this stage, the difference of irradiation of G_1 relative with G_2 triggers the switch scheme of the Ćuk converter, activating the switch and diode S_2 - D_1 , showing a sudden improvement in the power harnessed at the terminal. When time reaches 0.06 seconds, the irradiation values hold in $G_1=50\%$ and $G_2=100\%$ for the next 0.02 seconds. The voltage drop in V_{mpp_1} is followed by the measured voltage in PV_1 thanks to the change of the duty ratio in the Ćuk converter. Voltage drop also affects the V_{mpp_T} since the voltage reference is the sum of V_{mpp_1} and V_{mpp_2} . Control at the terminal converter helps to follow this reference voltage. A shadow is then emulated over PV_2 when irradiation goes from 100% to 50% matching G_1 at the time of 0.1 seconds. While this transition, irradiation relation G_1/G_2 surpasses the 0.7 value set in the switch scheme and the Ćuk converter switch S_2 is deactivated, which for the terminal power represents a small decay of the power delivered by the system. Irradiation from 0.1 to 0.12 seconds is kept as constant with $G_1=G_2=50\%$. Again only switch S_T is the one activated. After 0.12 seconds, the irradiation in G_1 goes from 50% up to 100% for the rest of the experiment. At this time, the lower irradiation is held by G_2 giving now the relation of G_2/G_1 . Now, when this light relation is lower than 0.7, (which occurs in point "b)", between 0.12 and 0.14 seconds) the pair of elements S_1 - D_2 in the Ćuk converter are activated, improving the power delivered at the terminal of the bi-directional converter by following the individual MPP on each PV panel. Once reach the time of 0.16 seconds, G_2 starts to rise from 50% until 100%, eliminating the mismatch and

deactivating the elements S_1 - D_2 . From the time 0.18 seconds onwards, only the boost converter is active, and the global MPP is achieved.

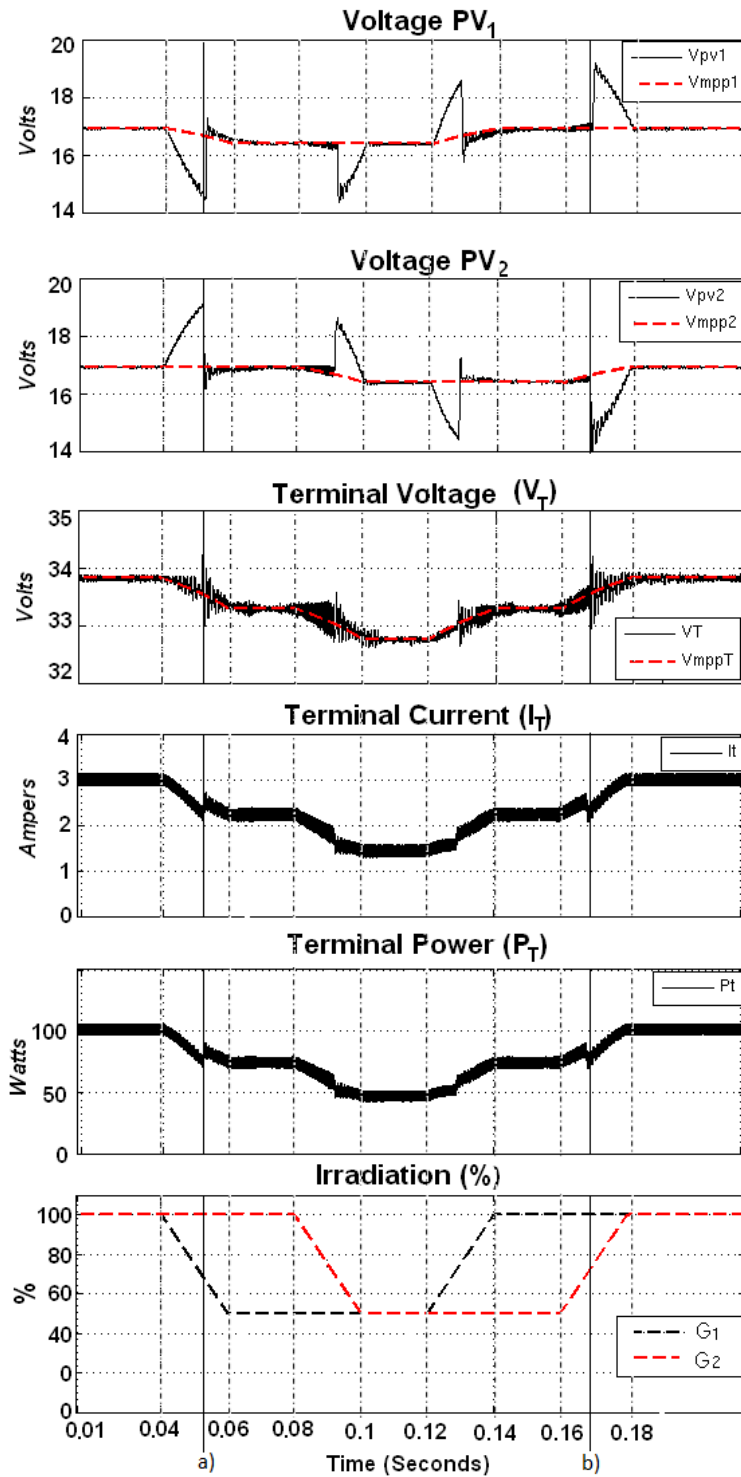


Figure 5.16 Results Ćuk Converter with online model.

5.3 Summary

The chapter presents comparisons of different cases where a bypass diode and the bidirectional Ćuk converter integrated with photovoltaic panels interconnecting with a load. A thorough analysis of open loop tests is then carried out to study the effect of different levels of irradiation over the PV panels and the power harness from them in each case. In each comparison, the integration of the Bidirectional Ćuk Converter has a clear advantage over the bypass diode when there is an irradiance difference between the solar modules. From the analysis, a new switch scheme is formulated where the converter is deactivated unless there is sufficient light difference over the panels.

A maximum power point tracker model was presented by Veerachary [76] in order to find the voltage region where the MPP is located. The temperature “variable” is then introduced to the PV model to have a more accurate value of the V_{mpp} . The V_{mpp} response is validated under atmospheric conditions present in the laboratory by Simulink model. The online model computer processing is as fast as the sample rate of the application, a clear advantage over other PV models where need learning process.

Closed loop system is achieved by sensing each voltage, current, irradiance and temperature response from the system. Two maximum power point trackers algorithms are introduced in the simulations. The “Perturb & Observe” response over a change of irradiance is then compared with the response of the online model MPPT based on temperature and irradiance. The improved switch scheme is then implemented depending on the irradiation of each panel.

Both algorithms compared in the chapter are able to find the global maximum power point. In the case where one PV is irradiated at 70% while the other PV is at 100%, both algorithms have a steady state generation around 80 watts, which matches the open loop results and represents a degradation of the system by 15% due to the shadow compared with the bypass diode case in open loop with a degradation of 22%.

The difference of the techniques lays in the complexity and the number of sensors the computation depends on. Since both techniques are online based, the constant measurement of the output is needed.

Chapter 6

Experimental Photovoltaic System Integrated with the Bidirectional Ćuk Converter

The direct impact of atmospheric conditions on the photovoltaic panels makes the system susceptible to sudden changes. In order to control and manage the power harvested from the renewable source, various electronic instrumentation are provided. Sensors such as voltage, current, light irradiance and temperature are required to feed data back to the microprocessor and activate the algorithm to reach the maximum power point of the system.

The present chapter covers the instrumentation and system design of an integrated photovoltaic converter forming a closed loop system which will maintain the maximum power output under varying light and temperature conditions. The system block diagram is presented in Figure 6.1.

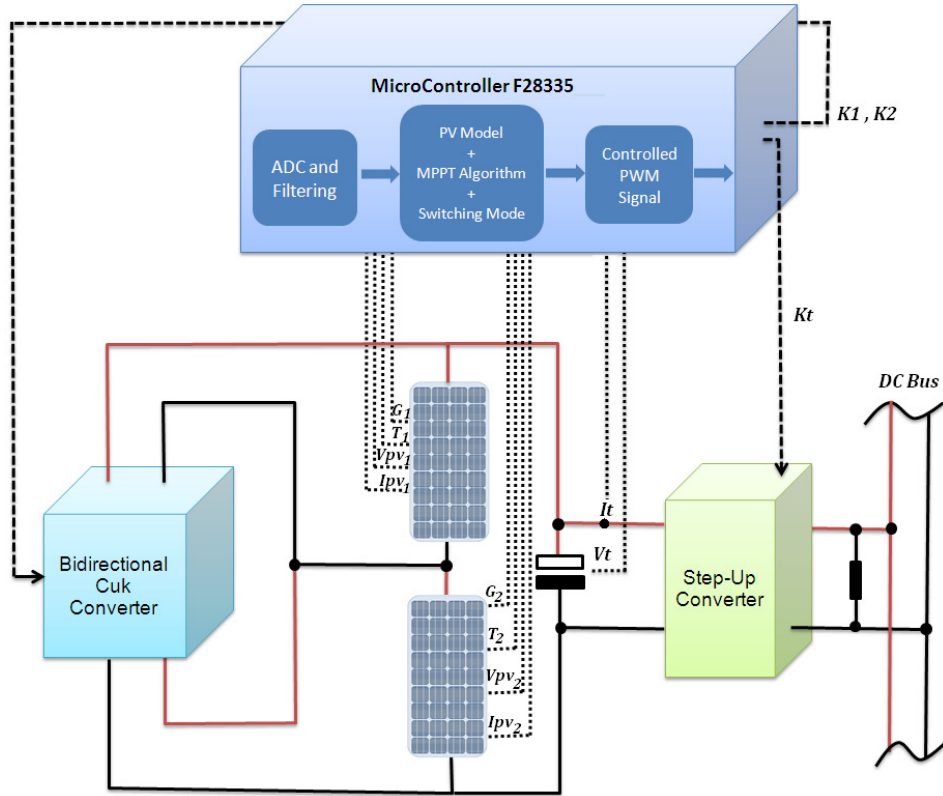


Figure 6.1 Photovoltaic converter with module integrated converter and sensors

6.1 Bidirectional Ćuk Converter

Here a bidirectional Ćuk converter is designed for research purposes only, i.e it is a demonstrator and not rated for commercial operation. In Chapters 3 and 4 the Ćuk converter as a solar converter was analysed theoretically. Using a set component values calculated in subchapter 3.5 is presented in Table 6-1, these corresponding to inductance and capacitances in the converter.

Component	Value
Inductance L_1 and L_2	$3.03mH$
Capacitor C_1 and C_2	$10.3\mu F$
Capacitor C_n	$82.5\mu F$

Table 6-1 Ćuk converter components values

As a precaution, a safety margin was calculated, and an inductor of 5Amp current rating was selected; however the largest commercially available inductor of this rating is only 1mH. Due to the high inductance needed which was not currently available, a compromise within the design had to be made. Dealing with the problem will lead to three possible solutions:

- 1) Increasing the switching frequency,
- 2) Connecting inductors in series,
- 3) The ripple is compromised.

Due to the relationship of the frequency with the inductor size, an increase of the switching frequency will reduce significantly the inductance value. This solution will be associated with higher switching loss. The second solution will consider connecting in series three inductors, considerably increasing the price and size of the converter. A viable solution is found in a compromise between the second and third solutions, whereby connecting in series two 1mH inductors compromises the ripple, increasing it to 11% at 250mA.

Since the Bidirectional Ćuk converter is a symmetrical topology, the inductors will be the same in both sides of the converter with a total of four inductors of 5A/1mH from the maker EPCOS.

Capacitors C_1 and C_2 are chosen by availability within a tolerable range. The next capacitance value available corresponds to 22 μ F, whereas for the capacitor C_n a capacitor of 82 μ F will be enough for research purposes. Since each photovoltaic panel, V_{oc} can produce 20 volts, and there will be two connected in series, each capacitor should be able to handle 40 volts. The next available rated value is 160 volts which will fit with the circuit characteristics. Higher capacitance values could have been used in the converter in order to mitigate the ripple, but a delay in the step response of the system could be produced. Due to the nature of the system, time is not a critical factor in the process and should not have a great impact within the overall performance.

Since the PV module maximum current is 2.2A and maximum voltage 20 V, the switching and diode components need to have high current and voltage handling capabilities at the frequency of 20 kHz. At a duty cycle of 50% the on/off time is 25 μ Sec, though, the converter will be designed to work within the range of 40% to 60% duty ratio.

The switching components S_1 and S_2 are realised by the MOSFET “STB24NF10” [97]. The minimum duty cycle expected is 40% which corresponds to 20 μ s. the “STB24NF10” is designed to handle currents up to 26A and a drain voltage source of 100V with the gate in the “off” state. According to the datasheet, the “on delay” is 60ns, and the rise time 15ns, these being in a switching circuit of 50V/12Amp; since the converter will be working at lower current and voltage levels, the speed is more than enough. The diodes D_1 and D_2 are chosen as “DPG10I300PA” [98] from manufacturer XYS Semiconductors. This diode was selected for the high current capability of up to 20A and the fast recovery time.

The final product is presented in Figure 6.2, and the PCB design can be consulted in Appendix F.

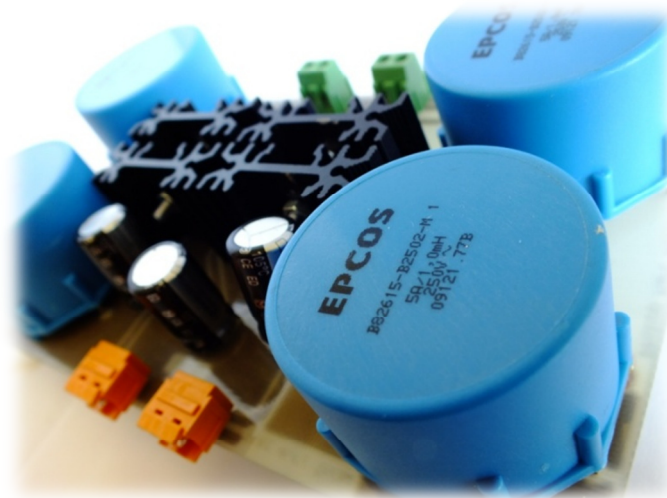


Figure 6.2 Bidirectional Ćuk Converter

6.1.1 Efficiency

The converter integrity needed to be tested, so a thorough efficiency test was executed in order to evaluate the performance of the system. The converter is connected at the input to a variable voltage source and at the output to a constant load of 22Ω . A PWM signal is then connected to the MOSFET “S₁” whereas the switch “S₂” is grounded.

When active, at a duty ratio of 50% or less, the converter will perform as a step down whereas above 50% it will act as a step up converter. The test was conducted varying the voltage from 4 volts to 20 volts with a duty ratio ranging from 20% up to 70%.

Figure 6.3 presents measured data from the test; these can be found in Appendix G. The graphic shows that when the voltage and duty ratio are near the design values, the converter presents a higher efficiency, and since the operational duty ratio will vary from 40% to 60% we can conclude that the Bidirectional Ćuk Converter is efficient enough for the purposes of this investigation.

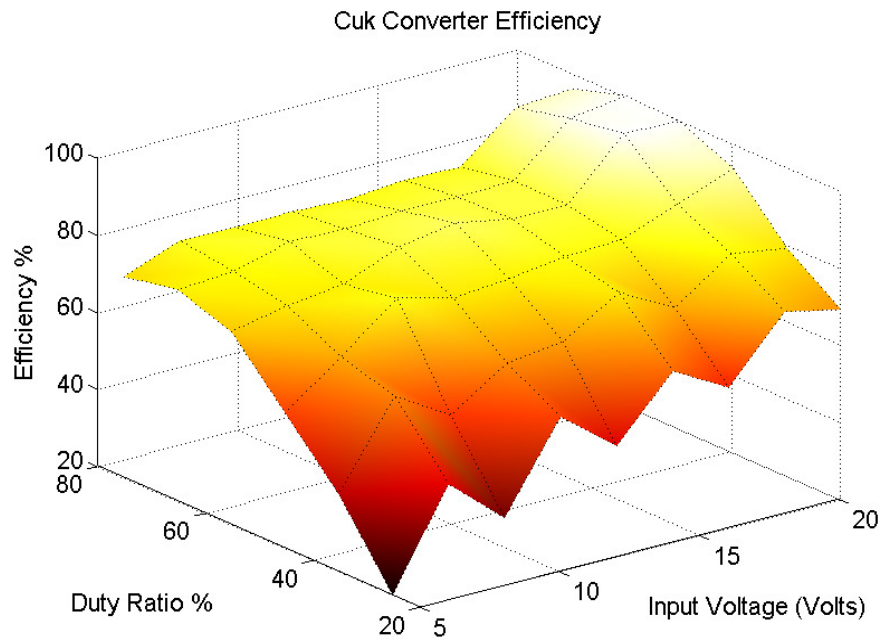


Figure 6.3 Efficiency graph of the Ćuk Converter

6.2 Photovoltaic System Interface

A description is now given of the electronic instruments and software interface which were designed to provide information to the microprocessor and hence allow it to maintain maximum power point operation. The converter is controlled by a PWM signal produced by the microprocessor.

6.2.1 Hardware

6.2.1.1 Light Irradiance and Temperature Sensor

Commonly, an ambient light sensor made of semiconductor material will have an I-V curve with exponential shape. Since light irradiance is assumed to be linear at the PV Setup discussed in subchapter 2.6, a linear output is more convenient. The light sensor chosen is the “Ambient Light Sensor SFH 5711” [99] by OSRAM. Due to the particular built-in characteristic of the logarithmic output current (Linearization of the exponential output from the semiconductor material) and the SMD encapsulation, this is a practical choice for experimentation. Size is an important factor due to the obstruction that a sensor can generate in the solar module. A load resistor of 43k Ω across the sensor output is installed to scale the current signal into 0v - 2v output that will represent 0% to 100% sun irradiance.

The temperature sensor uses the component “TC1047” from the manufacturer Microchip [100]. The TC1047 is a linear voltage output sensor whose output signal is proportional to the temperature in the chip. Temperature measured is represented by a voltage signal with a scale of 10mV/ $^{\circ}$ C, starting from 500mV as 0 $^{\circ}$ C. PCB connections are represented in Appendix H and Figure 6.4 shows the miniature sensors.

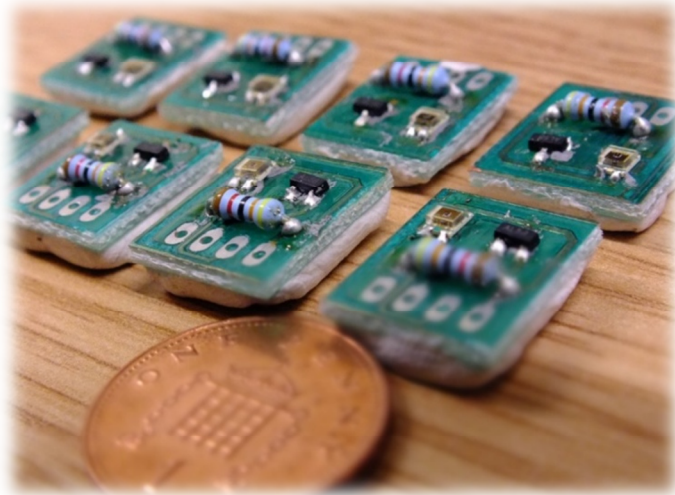


Figure 6.4 Irradiance and Temperature Sensor

At the installation, three sensors of temperature and irradiance are distributed over the solar module (Figure 6.5), and their measurements are averaged.

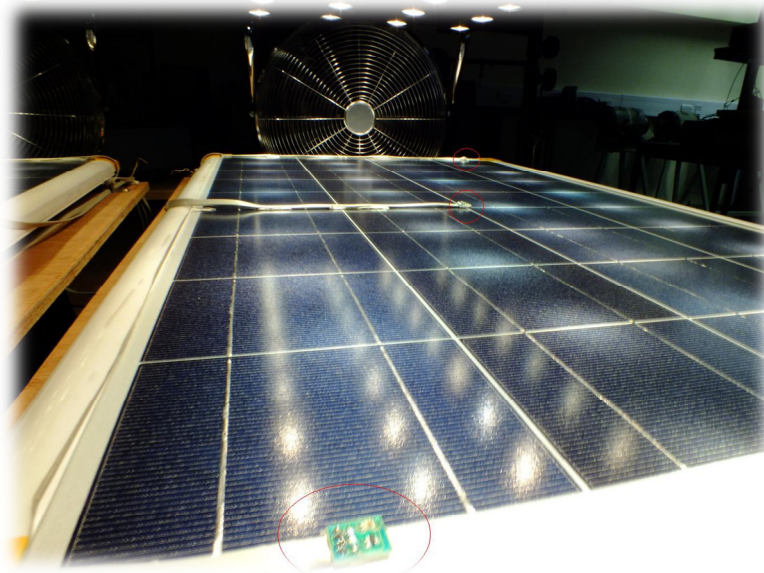


Figure 6.5 Solar Module with Temperature and Irradiance Sensors

6.2.1.2 Voltage & Current Transducers

a) Voltage Transducer

The voltage signal is produced by the transducer LV 25-P (see Figure 6.6) from the manufacturer LEM [101]. For voltage measurements, a proportional current must flow in the resistor R_{in} which is selected by the equation 6-1, considering that $V_{oc} = 20volts$ for each panel and nominal current for the primary side of the transducer is $i_{inmax} = 10mA$.

$$R_{in} = \frac{V_{in}}{i_{in}} = \frac{20volts}{10mA} = 2k\Omega$$

6-1

The first immediate resistor value available is $2.2k\Omega$, which will make the new $i_{in} = 9.16mA$. The R_{vo} depends on the output current i_o which is calculated by

$$i_o = i_{in} \times K_N = 9.16mA \times 2.5 = 23mA ,$$

where K_N is the conversion ratio from the datasheet specifications, giving an output voltage ratio of 10:1, hence

$$R_{vo} = \frac{V_o}{i_o} = \frac{2volts}{23mA} = 87\Omega$$

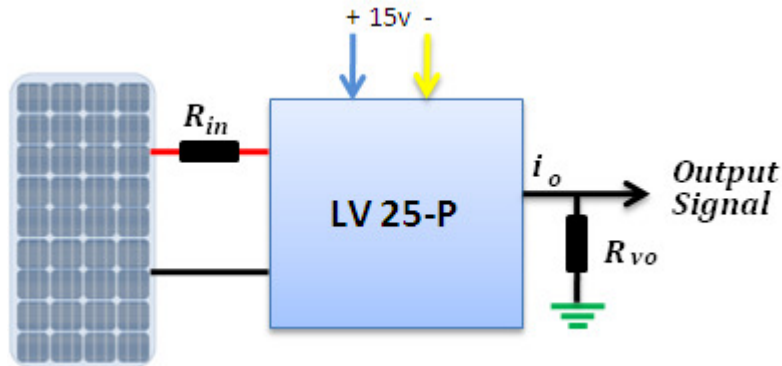


Figure 6.6 Voltage transducer block diagram

The electronic circuit is mounted inside an insulated box (Figure 6.7) to prevent damage to the equipment. Electrical plugs are installed to have a quick access to

the transducer terminals. PCB schematics for the voltage transducer are in Appendix I.

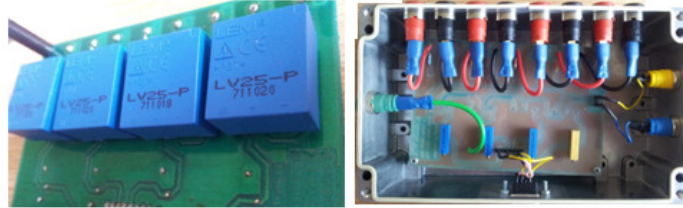


Figure 6.7 Voltage transducer circuit mounted

b) Current Transducer

The current transducer chosen is LA 25-NP [102] from the manufacturer LEM. Due to the advantages of power isolation from the control signal by using the Hall Effect [103], current overload capability and simplicity, the current transducer is good enough for research purposes. The Transducer has many configurations to work at different current levels, and in this particular case uses a turns ratio of 5/1000. The scale needed by the transducer is 0.5V per 1 amp from the PV modules.

The output resistor R_{vo} connected in series with the output signal (see Figure 6.8) sets the gain of the nominal output current. To calculate the output resistor, the datasheet gives:

$$\begin{aligned} \text{Output Voltage} &= R_{vo} * \frac{i_o}{\# \text{ turns}} \\ 0.5v &= R_{vo} * \frac{25mA}{5} = 100\Omega \end{aligned}$$

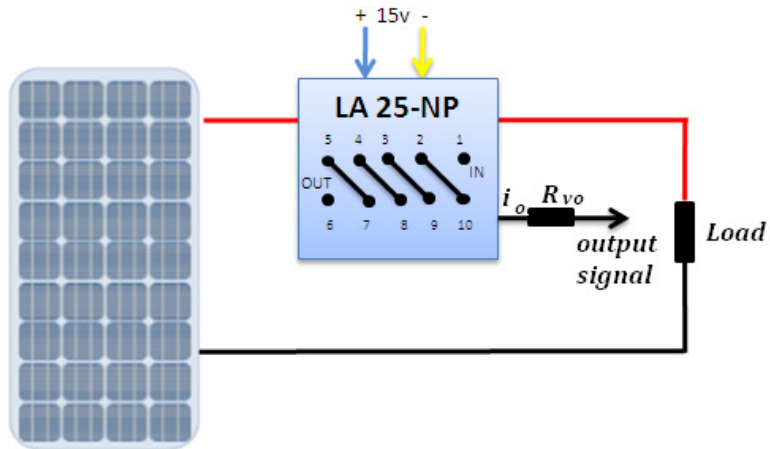


Figure 6.8 Connection diagram of current transducer LA 25-NP

The PCB board design is shown in Appendix J. The final prototype of the current transducer presented in Figure 6.9 were then housed in an aluminium box and connected to electrical receptacles for easy access by the user.

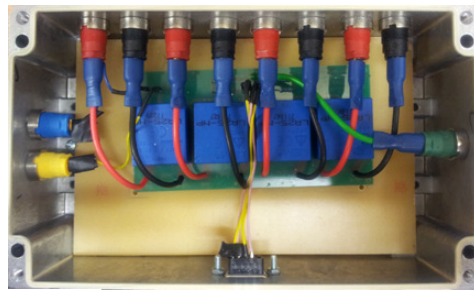


Figure 6.9 Current transducers boxed

Each transducer control box output signal in Figure 6.10 is wired directly to a DB9 receptacle for fast interfacing with the microprocessor.



Figure 6.10 Transducers control box

6.2.1.3 Microcontroller eZdsp™ F28335

The eZdsp™ F28335 is a developer kit manufactured by Spectrum Digital [104] which allows the user to develop and execute applications in real time. This board is supplied with the Digital Signal Controller TMS320F28335 from Texas Instruments. Elements included within the card are:

- TMS320F28335 Digital Signal Controller
- 32-bit floating point unit
- 512K bytes on-chip Flash memory
- 256K bytes off-chip SRAM memory
- 12 bit ADC with 16 channels
- 30 MHz input clock
- Multiple Expansion Connectors such as analogue and I/O
- Up to 18 PWM Outputs and 6 high resolution PWM output

Code Composer Studio v3.3 programming software is also supplied. The hardware/software allows the ability to couple with MATLAB Simulink, Real-Time Workshop and an embedded target for TI C2000 DSP to undertake rapid prototyping [105], allowing not only fast connection, but also the use of the same Simulink model of the complex algorithms and compiling them into the DSP.

The number of inputs and outputs of the photovoltaic system is the main reason for choosing this microcontroller. The system I/O can be listed by the inputs signals as the transducers and output signals as the PWM's which will control the converters. The list of I/O hence follows:

- 1) Input signal of Voltage measurement from PV_1 , PV_2 , PV_3 and V_t
- 2) Input signal of Current measurement from PV_1 , PV_2 , PV_3 and I_t
- 3) Input signal of Temperature sensor from T_1 , T_2 , T_3
- 4) Input signal of Light irradiance sensor from G_1 , G_2 , G_3
- 5) Output signal of PWM for S_{1-1} , S_{2-1} , S_{1-2} , S_{2-2} and S_T

Fast interconnection with the transducers control box and the microcontroller is made by DB9 receptacles. Due to the high cost and sensitivity of the DSP card, a box made from acrylic was fabricated to contain and isolate it (see Figure 6.11). The PWM output signal is also installed with a DB9 receptacle.

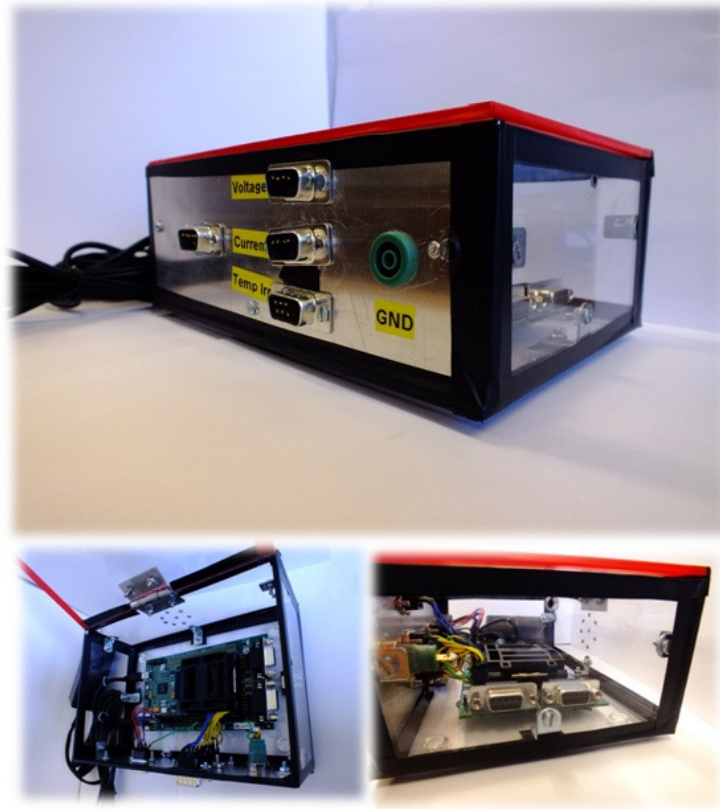


Figure 6.11 eZdsp™ F28335 board with interface box

The DSP is integrated with an analogue to digital converter with a resolution of 12 bits which translates to 4095 values within the range of 0-3volts as the input control signal, each of these steps representing ≈ 0.733 mV. 16 channels are available in the microprocessor, and up to 14 are used in this investigation.

The Bidirectional Ćuk Converter is controlled by the PWM signal calculated by the MPPT algorithm mentioned previously in subchapter 5.2. The Integrated PV system is expandable to interact with up to three PV panels, two Bidirectional Ćuk Converters and a Terminal Boost converter as in Figure 3.6 and Figure 3.9.

6.2.1.4 PWM Driver

In order to control the output voltage from the PV Panels, the MOSFETs installed in the converter needs to be driven by the PWM signal evaluated by the microcontroller. According to its specifications, the DSP F28335 has up to 18 PWM channels with amplitude of 3.3 volts whereas the MOSFET gate requires a minimum signal of 10 volts. In order to step-up the PWM control signal from the DSP and isolate it from the power electronics, a PWM driver is designed and is presented in Figure 6.12.

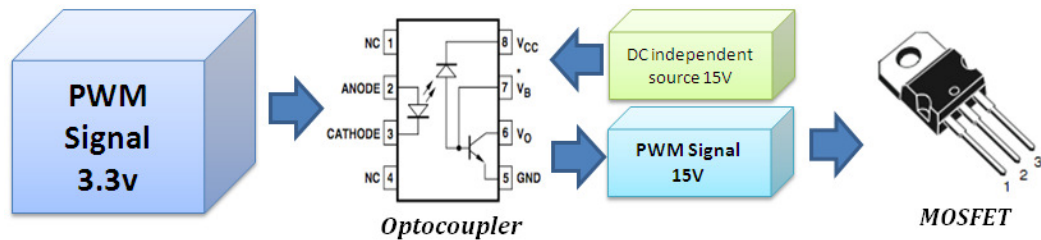


Figure 6.12 PWM driver Block diagram

The approach used in this project is to isolate the signals with Optocouplers HCNW-4503 by AVAGO Technologies. Moreover, they are connected to an independent DC source of 15 volts in order to increase the amplitude of the PWM output signal. The DC source uses the NKE0515SC manufactured by Murata. Furthermore, the signal is fed to a PWM driver chip TD3511N from STMicroelectronics, and from there to the MOSFET gate. PCB board schematics with five PWM drivers are presented in Appendix K. Resistance and capacitance values have been selected using the datasheet. The final prototype (see Figure 6.13) must be connected to the DSP interface box and the converters.



Figure 6.13 PWM Driver

6.2.2 Software

The evaluation board eZdsp™ F28335 is supplied with a copy of the Code Composer Studio v3.3 and a list of libraries which can be found in the Texas Instruments website [104]. The board interfaces with the user by C++ language, using this to activate different features in the DSP. A thorough understanding of C++ programming is needed to use the board. MATLAB software provides the opportunity to use the Simulink friendly interface using a high-level programming language and allowing rapid prototyping to be achieved as shown in [105], [106].

The MATLAB version used in this report is 2009b combined with compiler Microsoft Visual C++ 2008 [107] and Simulink target support toolbox.

6.2.2.1 Matlab Simulink Embedded Encoder and Code Composer Studio

The Simulink environment offers support for the Texas Instruments C2000 microcontroller family which includes the DSP F28335. With the “target support toolbox” and “embedded encoder”, Simulink can activate the Analogue to Digital Converter and the PWM integrated in the DSP. The Simulink system in Figure 6.14 uses as input the ADC (left side), whose signal needs to be filtered and conditioned

for processing any given user algorithm. Once the signal processing is completed, a PWM signal is created by the ePWM box as the system output in the right side of the figure.

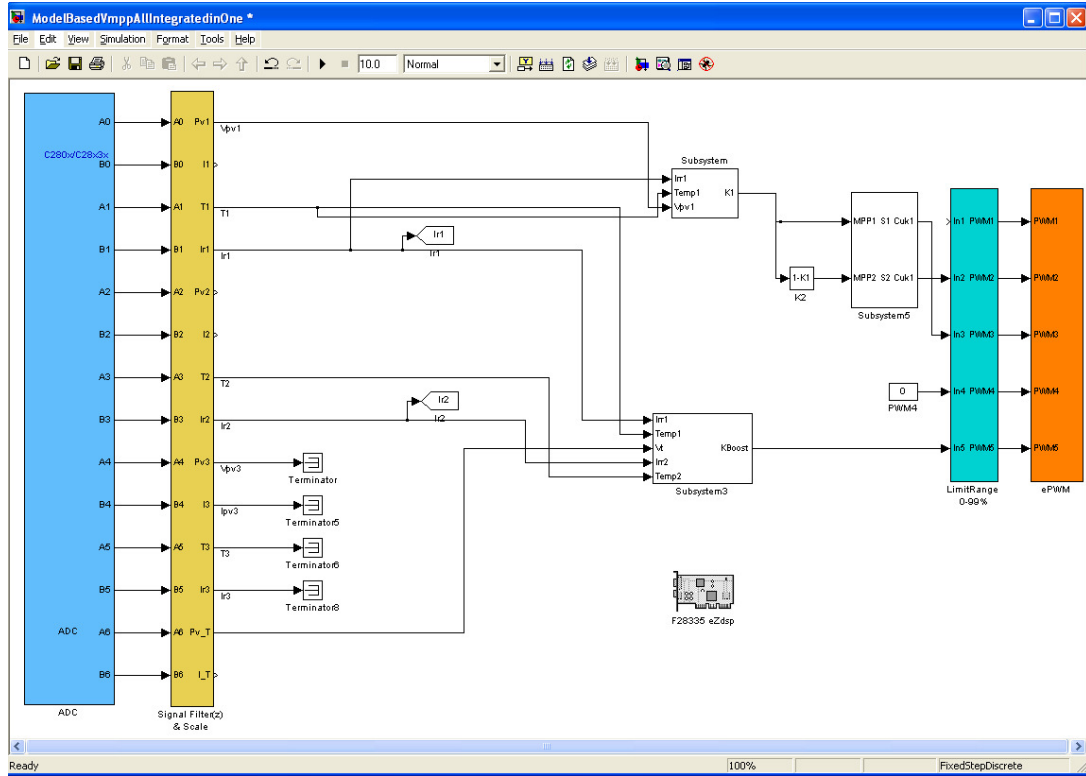


Figure 6.14 Simulink model with F28335 board support

The measured signal need conditioning by a gain scaling before its use by signal processing algorithms such as the MPPT for the inner and outer DC/DC converters.

6.2.2.2 Signal Conditioning

ADC activation is made under commands taken from the reference guide [108] of the DSP.

- ADC

The conversion sampling time is set equal to the switching frequency of the converter in Figure 6.15, so the instantaneous power will be updated at every switching time of the converter [109]. Conversion is set to produce simultaneous pairs of data on channel A and channel B of the DSP. Transducer signals are connected as indicated respectively in Table Table 6-2.

ADC Channel	Signal acquired
ADCINA0 & ADCINB0	V_{PV1} & I_{PV1}
ADCINA1 & ADCINB1	T_1 & I_{rr1}
ADCINA2 & ADCINB2	V_{PV2} & I_{PV2}
ADCINA3 & ADCINB3	T_2 & I_{rr2}
ADCINA4 & ADCINB4	V_{PV3} & I_{PV3}
ADCINA5 & ADCINB5	T_3 & I_{rr3}
ADCINA6 & ADCINB6	V_{PVT} & I_{PVT}

Table 6-2 ADC acquisition signal channels

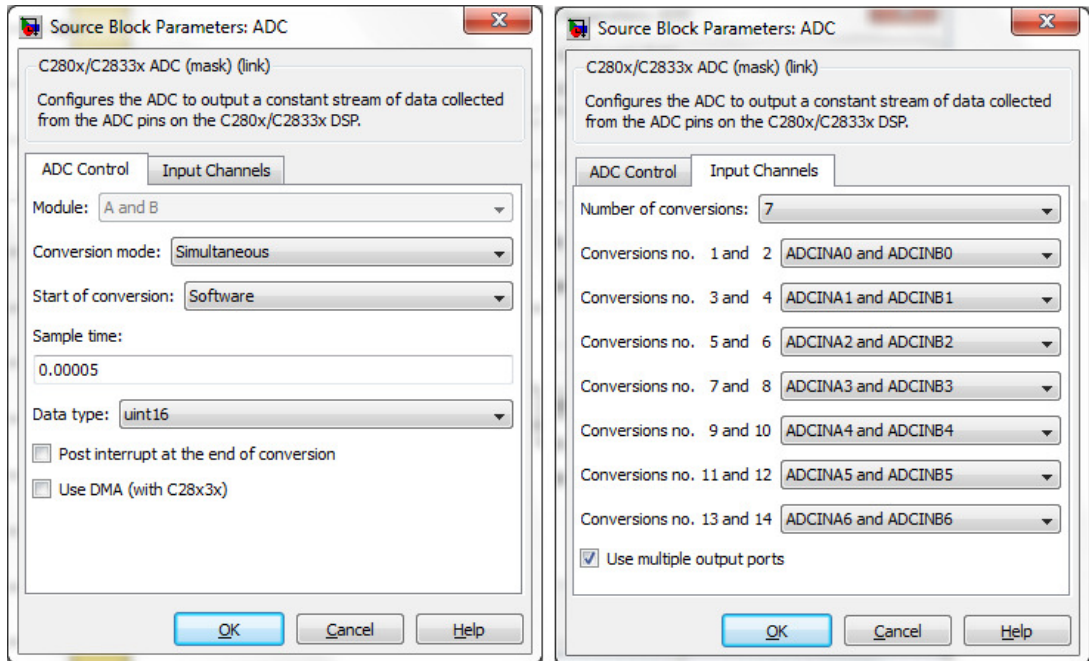


Figure 6.15 ADC conversion configuration

- Scaling

Scaling factors are set by the relationships of values from the transducer, the voltage and the resolution of the ADC. The digital value of the input analogue voltage is derived by:

Digital value = 0, when input ≤ 0 V;

Digital value = $4095 \times \frac{\text{Input Analog Voltage} - \text{ADCLOW}}{3}$, when $0 \text{ V} < \text{input} < 3 \text{ V}$;

Digital value = 4095, when input ≥ 3 V.

Thus, the scaling factor for each conversion of the transducers are calculated and listed in Table 6-3.

Transducer Signal	Scaling factor	Real Value
$V_{PV1}, V_{PV2}, V_{PV3}$	0.007326007326	0-30V
V_{PVT}	0.021978021978	0-60V
$I_{PV1}, I_{PV2}, I_{PV3}, I_{PVT}$	0.001465201465	0-6A
T_1, T_2, T_3	0.073260073260	0-100°C
$I_{rr1}, I_{rr2}, I_{rr3}$	0.074074074074	0-100%

Table 6-3 ADC Scaling factor

- PWM

The enhanced PWM module integrated to the DSP F28335 has the capability to control up to 18 channels[110] or use these as 6 channels of High Resolution PWM [111]. The enhanced PWM (ePWM) is a module that can involve two PWM outputs labelled ePWMA and ePWMB. Within the microprocessor, there is a time base sub- module called ePWM event manager, entangled to each ePWM module. This sub- module is used to set the frequency of the 16-bit counter. Furthermore, the

input signal is being compared with the internal register CMPB in order to generate the PWM signal as in Figure 6.16.

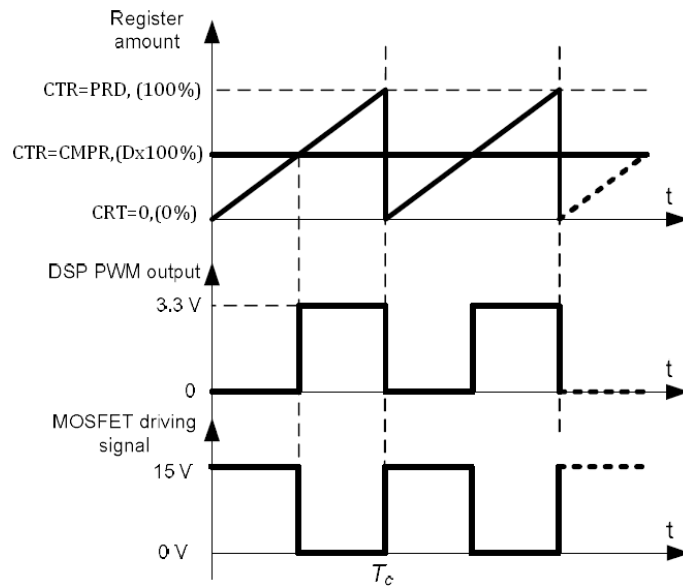


Figure 6.16 ePWM Generation

With respect to the generation of the PWM signal for the Ćuk Converter and Boost converter, the Simulink block configuration is set out in Figure 6.17.

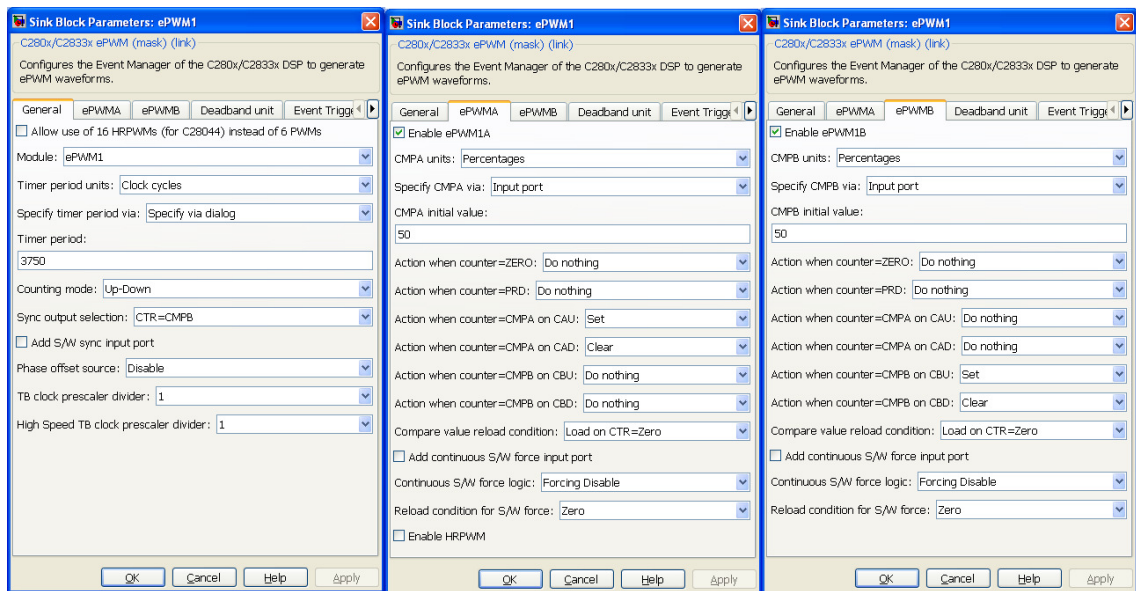


Figure 6.17 ePWM block configuration

6.3 Summary

In this chapter a variety of instrumentation designs was presented, to serve the purpose of sensing atmospheric conditions emulated in the laboratory and their effect on the solar modules in terms of instantaneous voltage and current.

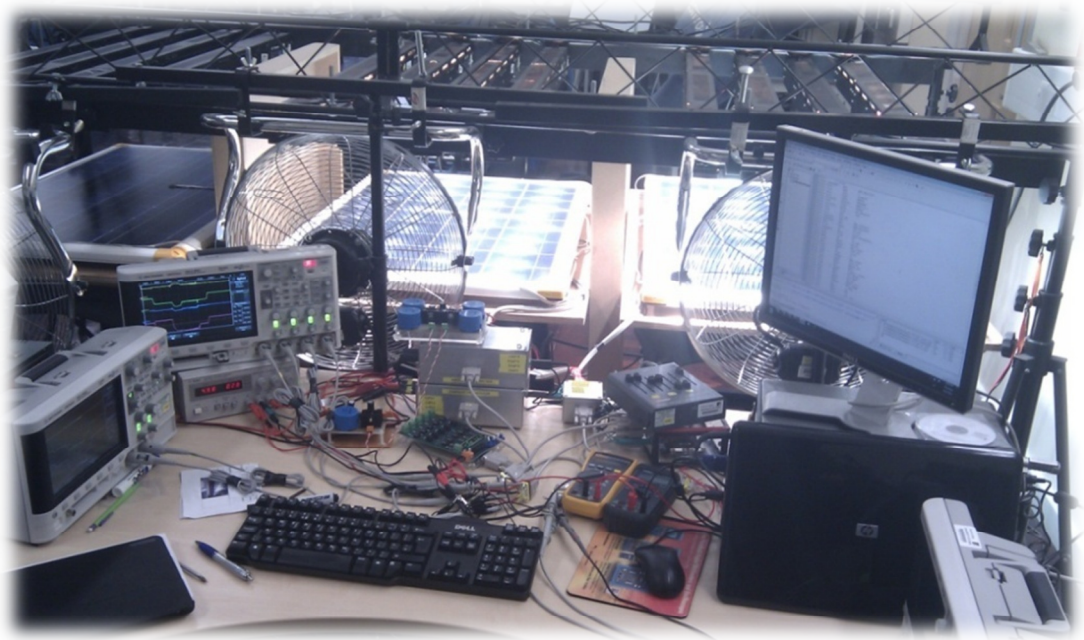


Figure 6.18 Hardware Final implementation

Chapter 7

Integrated PV Converter Implementation

It has been the overall aim of this work to study and develop a Bidirectional Ćuk converter integrated PV-panel module in both open and closed loops to harness the maximum power. In this chapter, the control techniques proposed so far in Chapter 5 of this thesis will be verified experimentally using instrumentation designed and presented in the previous chapter.

The chapter presents the responses of the practical converter applying different duty ratios in open loop confirming the simulation of the Transfer Functions in Chapter 4. Moreover, the close loop control of integrated converter PV panel system is performed in the laboratory. Dynamic responses of this system are investigated through introduction of different shading levels over the solar modules.

The follow experiments are performed with solar modules analysed previously in subsection 2.4 upon practical solar modules.

7.1 Open loop Test

7.1.1 Experimental results versus Transfer Function Model

The Bidirectional Ćuk converter prototype is tested to validate the ac small signal model derived in Chapter 4. Circuit shown in Figure 7.1 represents the converter connections where V_T is emulated by a constant DC source at 30 Volts in parallel with a load resistor of 25Ω .

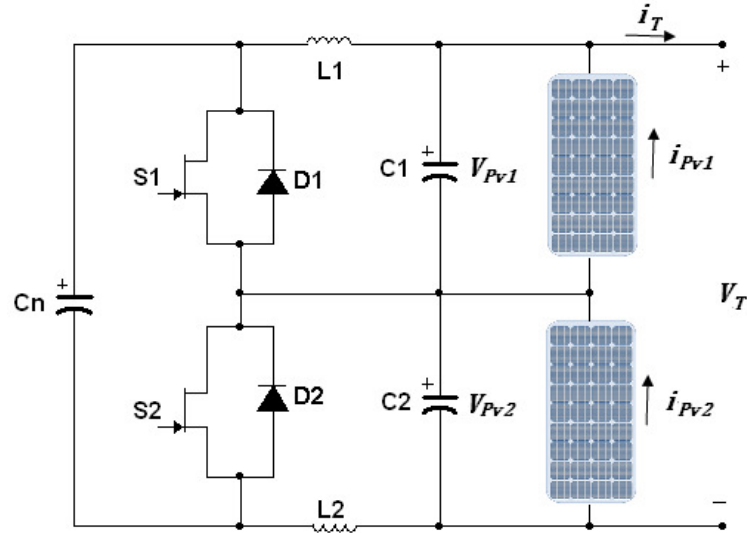


Figure 7.1 Integrated converter with PV

In the experiment, a mismatch in irradiation levels over the two PV panels is made where the level over PV_1 is at 30% that on PV_2 is at 100%. Duty ratio feeding to the converter is then changed from $K=0.40$ to $K=0.60$ in constant increments of $k=0.05$. The active switch pair is $S_2 - D_1$ since the solar module PV_2 is irradiated with more light relatively to PV_1 . The voltages of both PV panels across the terminals of Ćuk converter are presented in Figure 7.2 and Figure 7.2a. It can be seen that step changes take place at every 0.4 seconds, their features vary from damped (when the duty ratio is 0.40, 0.45 and 0.50) to under-damped (after the duty ratio has been changed from 0.50 to 0.60), presenting a clear overshoot. Moreover, Figure 7.3 presents the terminal voltage V_T , which holds the same level throughout with only minor disturbances. This is in contrary to the terminal current i_T changing at each step, giving different power values. Through graphical representation, the global maximum power point is found when the duty ratio is at 0.50 with 30 watts delivered into the load.

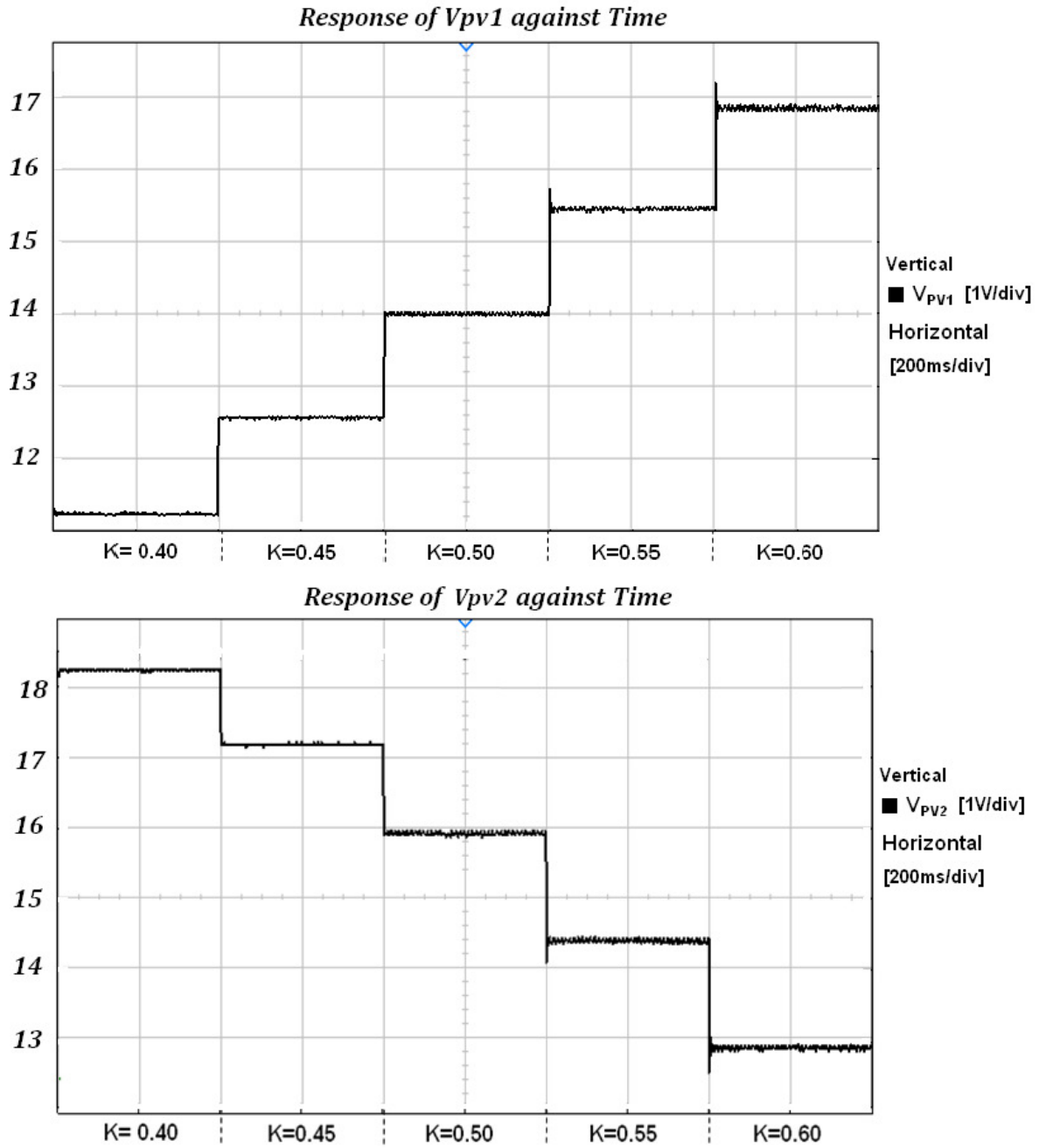


Figure 7.2 Response to Duty ratio of PV1 and PV2

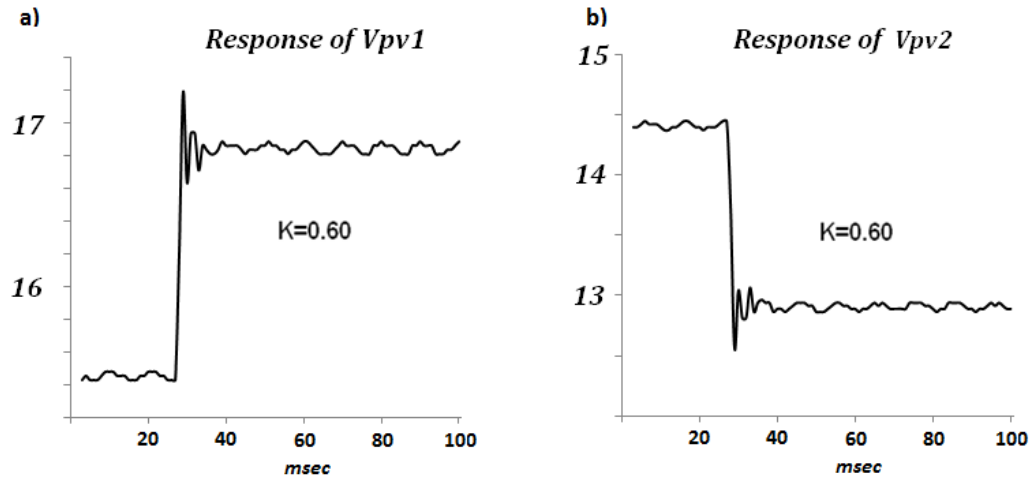


Figure 7.2a Zoom of Response against time when $K=0.60$

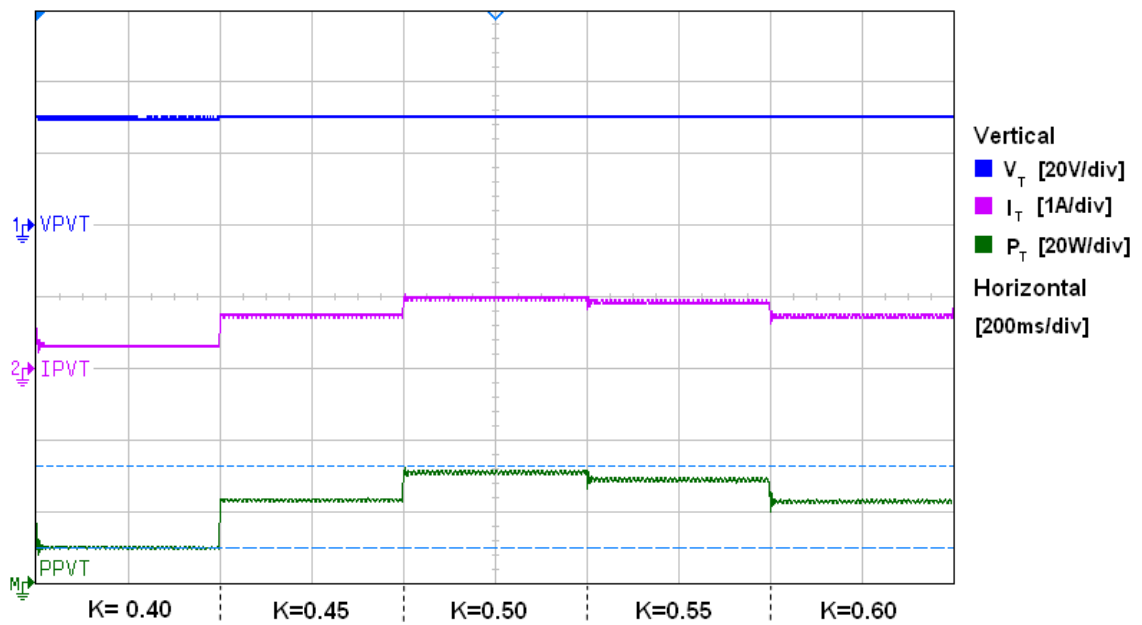


Figure 7.3 Transfer Function terminal response

Comparing to the simulation results shown in Figure 4.3 to Figure 4.4, the voltage step changes give similar pattern and step size. However, the transient variations in the simulation show less damping than that of the practical results. These differences may be due to that the components used in the simulation are assumed ideal and no parasitic impedance is considered. In addition the model

has been developed under a series of approximations which may not conform to the practical conditions, for example it assumed that when switching frequency is high, the values of $t_{on}t_{off}$, t_{on}^2 and t_{off}^2 would be smaller than L and C components, hence are negligible. Nevertheless the experimental results confirm well with that from the averaged model particularly for static responses, hence allowing further exploration of the model for converter controller design and analysis.

7.2 Closed-Loop Tests

Similar to the simulation studies of the closed-loop system presented in Chapter 5, implementation and verification of experimental closed-loop system are presented in this sub-section.

The system to be tested includes one bidirectional Ćuk converter, one terminal boost converter, two identical solar panels, PV₁ and PV₂, a DC Bus of 60V and a load of 25Ω connected as described in Figure 5.6.

7.2.1 Step responses under equal light level G₁=G₂=100%

The experiment represents a real scenario where there is no partial shading over the PV panels and studies the responses of terminal voltage and power of the integrated converter and PV-panel module. The control scheme used is the Online model based MPPT presented in Chapter 5. This sets the reference voltage of the control loop as the sum of the voltage values of both PV panels at the maximum power point when the light levels are G₁=G₂=100%. By comparing the measured voltage values, it generates the error signals for the P+I controller.

Figure 7.4 represents the responses of voltage and current for each panel, and Figure 7.5 shows the voltage, current and power variations at the system terminals.

Since irradianations on both panels are, for this test, the same, the bidirectional Ćuk converter switches are inactive according to the control scheme. As shown in Figure 7.4 and Figure 7.5, during the first 0.5 seconds the lights over the panels

are turned off, so there is little power generated by the solar panels and the load power is mainly supplied by DC source. Note during this period the system is under open loop operation; hence the voltage value is around 20 volts for each panel and the current is zero. Then the light levels are gradually increased from 0% to 100%. When irradiation over both PV panels reaches 100%, according to the measured temperature and irradiation values from sensors for each PV panel, the control algorithm calculates the voltage values corresponding to the maximum power point to adjust the duty ratio for the terminal boost converter. As can be seen in Figure 7.4 and Figure 7.5, all variables reach steady states after about 1 second. The total generated power measured at the terminals of the solar system is, approximately, $P_T \approx 54.37$ watts with a terminal voltage of $V_T \approx 32.16$ volts and a terminal current of $I_T \approx 1.68$ amps. Verification of the individual MPPT is done with equation 5-2 of the solar model which follows,

$$V_{mpp} = 0.7658 * \ln(1000) + 11.318 - 0.06 * (33 - 25) = 16.13 \text{ volts}$$

per solar module, giving a predicted terminal voltage of 32.26 volts. The signals presented in Figure 7.6 are gate pulses for switches S_T , S_1 and S_2 . S_T is operating at the duty ratio 48.2% while the other two switches are not operating, so their gate signals are at logical ground level.

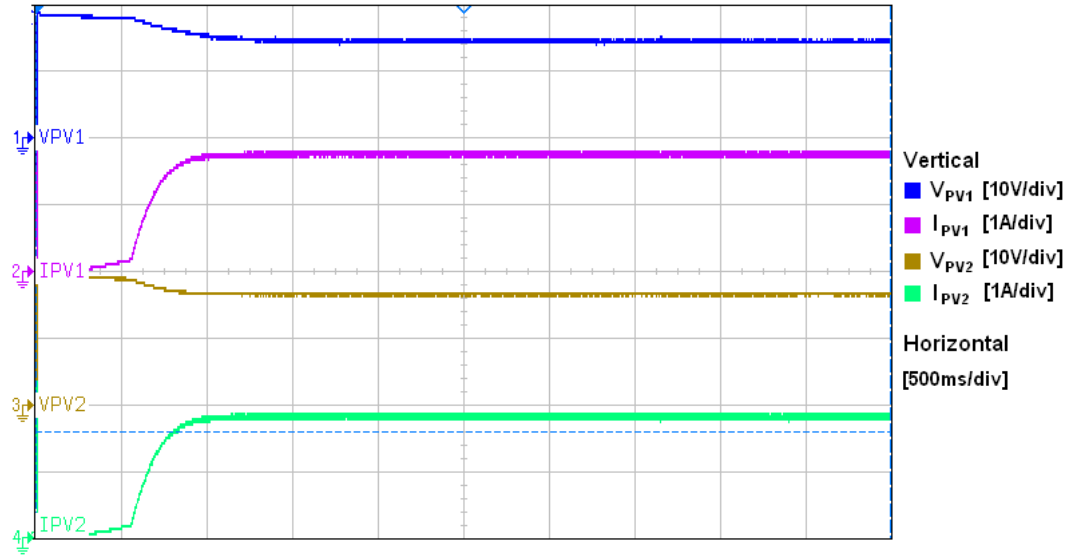


Figure 7.4 PV1 and PV2 step response, no shading

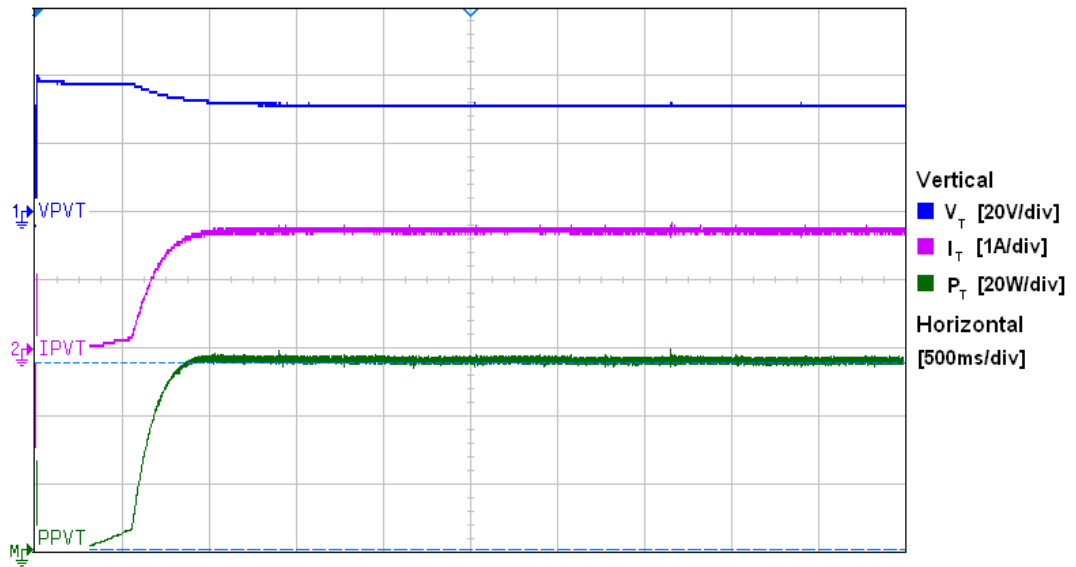


Figure 7.5 Terminal step response, no shading

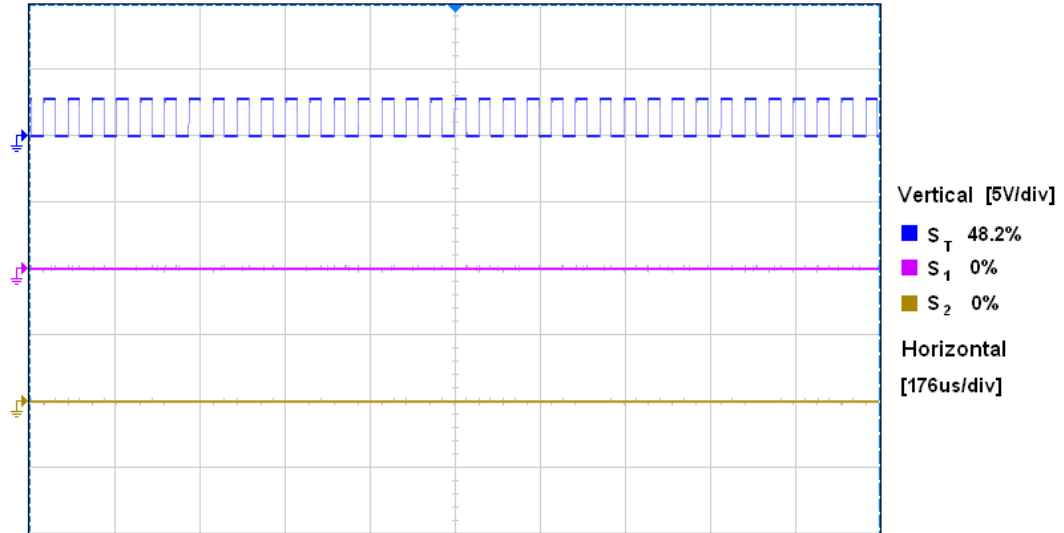


Figure 7.6 Switching signals for converter switches under equal light level

7.2.2 Step responses under partial shading over PV1

This experiment analyses the dynamic response when PV_1 is under a severe shading condition in which the light dims gradually from 100% to 30% while the light over PV_2 remains always at 100%. Figure 7.7 and Figure 7.8 represent the responses in each PV panel while Figure 7.9 shows the gate signals for S_T and S_2 .

Within the first two seconds after the start of the experiment, PV_1 and PV_2 are fully irradiated at 100% supplying a total of 53 watts. During this time only S_T is functioning while S_1 and S_2 are idle. After two seconds a shade is introduced over PV_1 , the light level is lowered down gradually from 100% to 30%. During the transition period from 2 to 3 seconds, when the difference between the light levels over the two PV panels becomes sufficiently high the switching control scheme described in Chapter 5 is activated. This sends the signals from light sensors installed over the solar panels to the DSP, which determines to control S_2 in Ćuk Converter. The duty ratio for S_2 , evaluated according to the model predicted V_{mpp2} , is 52.2% and switching signals are as shown in Figure 7.9. The generated power shown in Figure 7.8 presents a spike initially due to the delayed activation of the control scheme. As stated previously, if a shadow is present over a solar panel,

correspondingly its current changes linearly with the amount of irradiation. In Figure 7.7, the steady state current value I_{PV1} after the shading occurs is about 200mA whereas the current produced by I_{PV2} is 2 amps, showing the independence between the two panels due to the use of Ćuk converter. After about 4 seconds of the change of light level, the measured terminal power generated by the system settles to about 32 watts at terminal current of about 1.02amps and a terminal voltage at about 31.6volts. The generated power is higher with the Ćuk converter activated than just with a bypass diode, showing the clear advantage of this scheme.

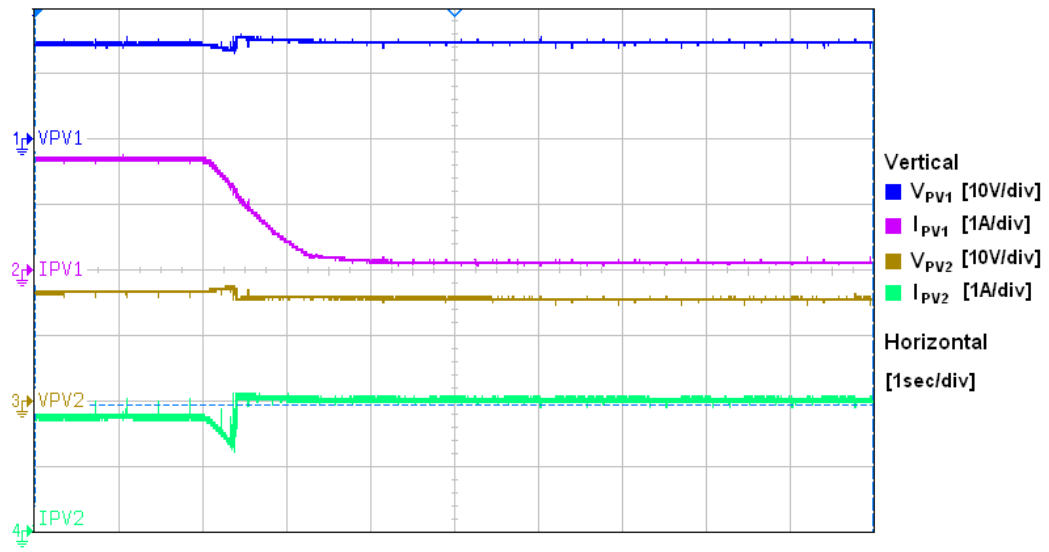


Figure 7.7 Responses of PV₁ and PV₂ with 30% Partial shading on PV₁

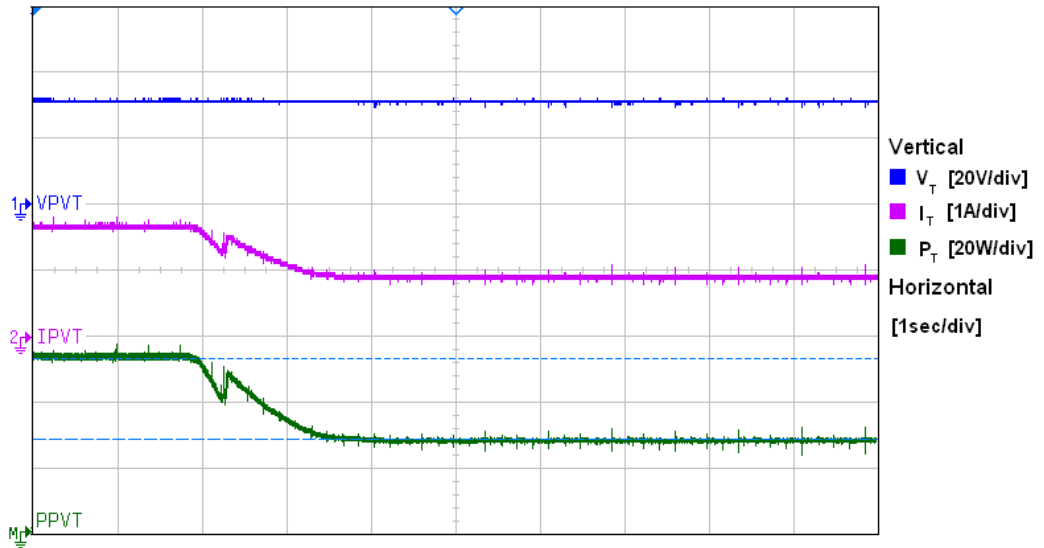


Figure 7.8 Terminal responses with PV model for a 30% Partial shading on PV_1

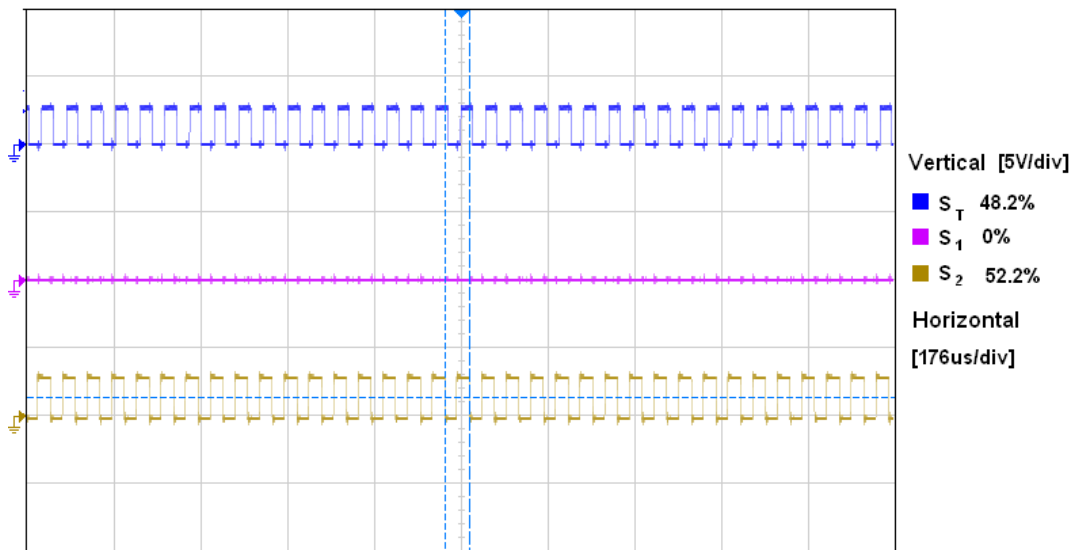


Figure 7.9 Switching signals for converter switches under a shading condition

Same experimental protocol is used to perform a comparison with Perturb & Observe algorithm in closed loop finding the global maximum power point at the terminal in Figure 7.10.

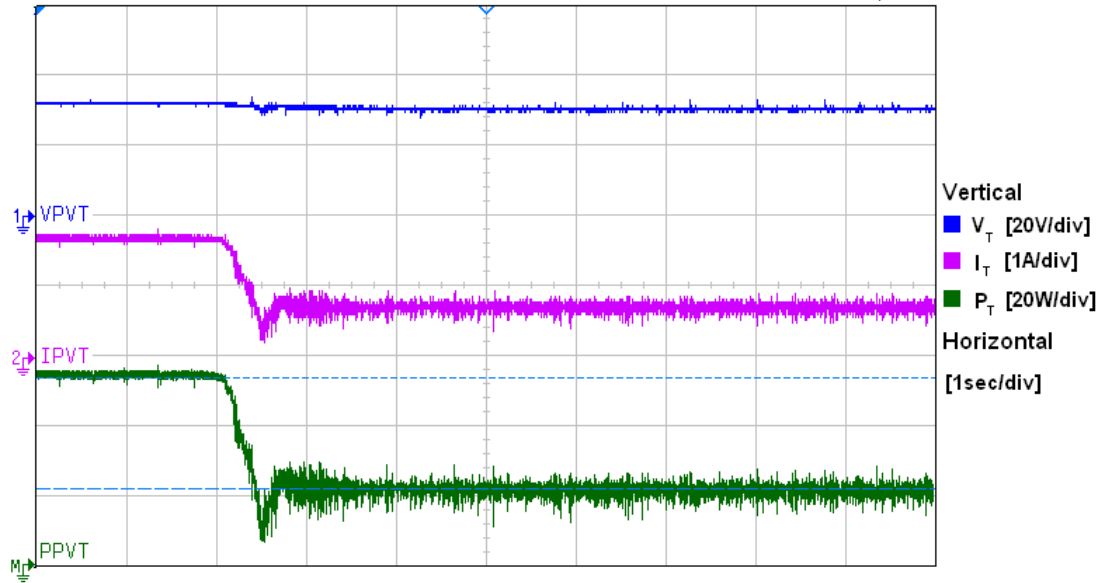


Figure 7.10 Terminal responses with P&O for a 30% Partial shading on PV₁

The perturb & observe algorithm as previously mentioned, at each sample instant the duty ratio for the outer boost converter is changed by a constant ± 0.01 , causing the corresponding inherent characteristic variations of voltage, current and power in Figure 7.10. Both algorithms achieve maximum power point, difference lays in the noise presented with the P&O technique.

7.2.3 System responses for different shading conditions

In this experiment, the integrated converter and PV-panel module and the proposed control scheme are tested by constantly varying the irradiation levels G_1 and G_2 . The variation patterns include five different scenarios as listed in Table 7-1 and illustrated graphically in Figure 7.11. The experiment is designed to cover the possible operating conditions where ratios of light intensity $G_{\text{shaded}}/G_{\text{unshaded}} < 0.7$, and demonstrate that the control scheme can activate the correct switch for each scenario. It is also aimed to show the system responses during the transitions between the changes of the light pattern. Figure 7.12 represents the voltage and

current measurement from individual solar panels PV₁ and PV₂ while Figure 7.13 gives plots of terminal voltage, current and power.

Scenario	G ₁ (%)	G ₂ (%)	Switch activation
A	100	100	S _T
B	50	100	S _T , S ₂
C	50	30	S _T , S ₁
D	50	50	S _T
E	100	100	S _T

Table 7-1 Dynamic Irradiation and switch activation

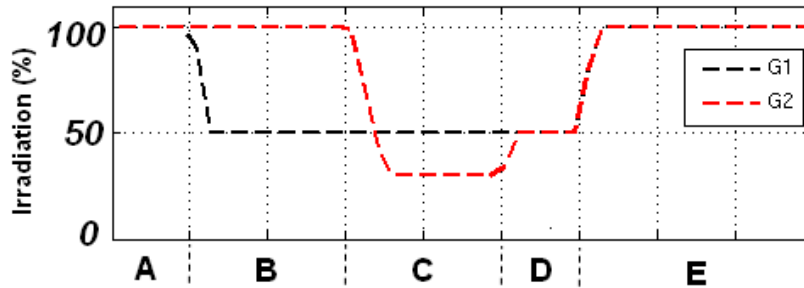


Figure 7.11 Irradiation changes over time

The experiment recordings start with the scenario “A” where measurements are in steady state values while irradiances G₁ and G₂ are equal to 100%, producing a terminal power of P_T ≈ 55.5watts at 32 volts as presented in sub-section 7.2.1. Since no shading exists between the panels, the inner Ćuk converter is off and the power produced is directly from the panels connected in series.

A sudden change of the irradiation over PV₁ takes place in scenario “B” where irradiation G₁ is gradually dimmed from 100% to 50% while G₂ is not affected and held at 100%. As the light intensity over PV₁ decays to the level such that the irradiation difference is large enough to activate switch pair S₂-D₁ within the Ćuk

converter, the individual maximum power point trackers for the converters start to search for the optimal operation points. The voltage and current changes on both PV panels are shown in Figure 7.12. An instant gain in the terminal power is presented as a spike with a magnitude of ≈ 7 watts while the light is in transition, this due to the Ćuk converter activation. It settles to a steady state value of 43.7watts with an $I_T \approx 1.375$ amps and a $V_T \approx 31.7$ volts.

Moreover, in scenario "C" a severe shade is introduced over the PV_2 going from 100% to 30% while G_1 holds at 50%. During the light changing transition, the inner converter switch S_2 is deactivated by grounding the gate signal. Moments later, when the irradiation difference is large enough to activate S_1 (Figure 7.14), voltage values in each PV panel experience a change due to the controller action. Since the solar module PV_2 is now the one with lower irradiation relative to that on PV_1 , the current produced from it is also the lowest. Steady state is achieved at the second half of this scenario producing a terminal power of $P_T \approx 7.3$ watts, with terminal current $I_T \approx 0.238$ amps and a terminal voltage of $V_T \approx 30.64$ volts.

Scenario "D" starts with an increment of irradiation in PV_2 , going from 30% to 50%, the current from PV_2 increases correspondingly. When the light levels are equal over both panels ($G_1 = G_2$), both switches S_1 and S_2 at the inner Ćuk converter are off, leaving the solar modules in series and the terminal converter switch S_T to find the global maximum power point of $P_T \approx 25$ watts with $I_T \approx 0.792$ amps and $V_T \approx 31.55$ volts.

The final scenario "E" starts with both light levels G_1 and G_2 increasing from 50% to 100% simultaneously. As shown in Figure 7.12 and Figure 7.13 the currents through individual and terminal converter all increase, leading to the power increase to the maximum power point as that produced in scenario "A".

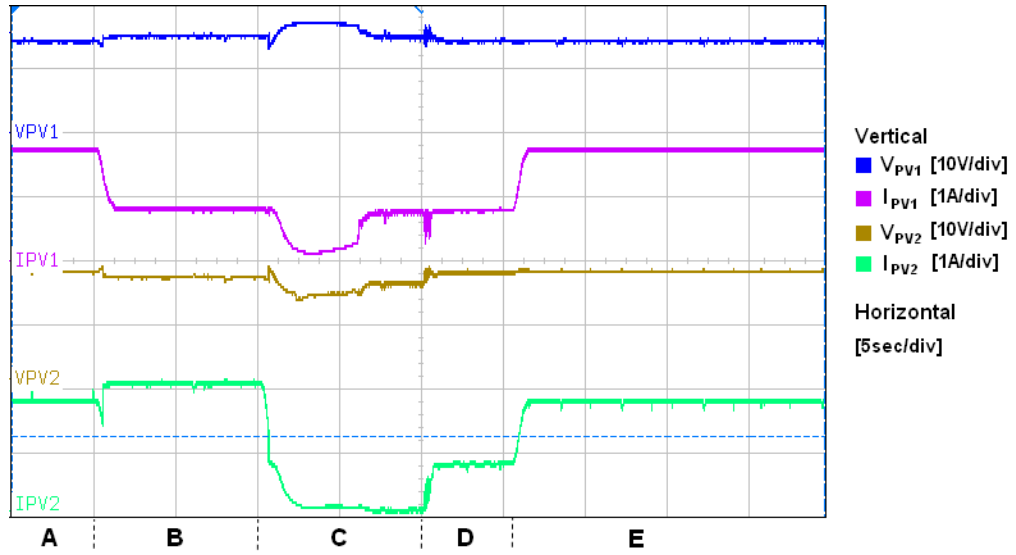


Figure 7.12 PV1 and PV2 measurements to dynamic response

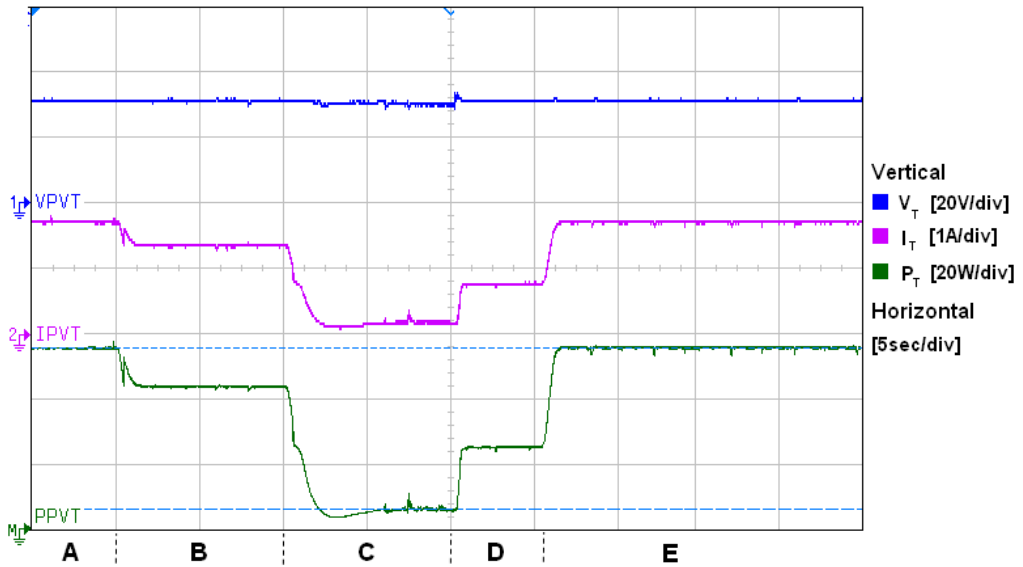


Figure 7.13 Terminal measurements to dynamic response

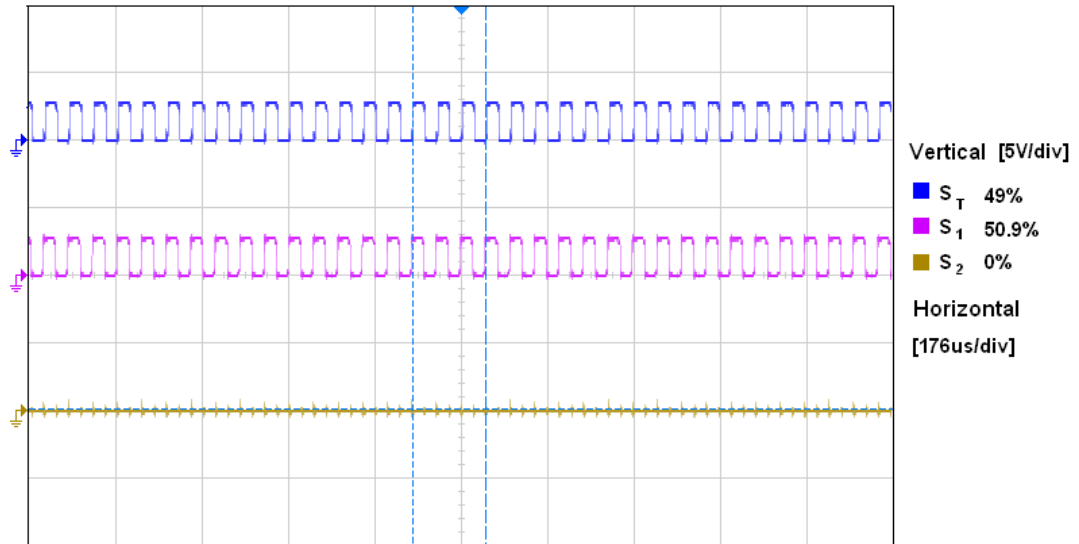


Figure 7.14 PWM switch signal when $G_2/G_1 < 0.7$

7.3 Summary

The chapter presents a series of experimental results obtained in the laboratory with the prototype design presented in Chapter 6 of this thesis.

Transfer functions step response discussed in chapter 4 are verified by experimentation under similar conditions where PV panels connected to the converter presents a mismatch of irradiance. While different duty ratios are applied to the converter, voltage step response is recorded with an oscilloscope against time.

The dynamic responses of the system in closed loop are tested by changing irradiation levels over the PV panels. Online model-based MPPT is capable of searching for voltage values which achieve the global maximum power points with irradiation and temperature measurements from each solar module sensor. Control strategy concluded in previous simulations is verified by the experimental results. A clear improvement in the power harnessed from the PV panels is shown in cases where considerable light differences are presented.

Chapter 8

Conclusions and Recommendations

This research project has been set up to investigate converter topology and compare MPPT control strategies for photovoltaic power generation systems working under uneven irradiation conditions. The specific aim has been to enable the serially connected PV panels to operate at their optimal power points according to their respective light levels. The project has led to a successful development and practical implementation of an integrated converter and PV-panel module where a bidirectional Ćuk converter is connected across two serially chained PV panels, and a terminal boost converter is used as a whole system power conditioner. A novel model based control scheme has been developed for this system which has the feature to predict the optimal power point voltages for individual PV panel in the system leading to effective and efficient operation in harnessing power under any light level patterns over the solar panels, either even or partially shaded. The test results of the scheme have shown that it can respond to dynamic atmospheric condition changes to locate the global maximum power points quickly and accurately. A summary of the detailed contributions from this work is presented below.

- A detailed analysis of an integrated bi-directional Ćuk converter and PV panel module has been given leading to a mathematic model developed for such a system. This is through deriving State Space equations of a bidirectional Ćuk converter in bypass connection with two PV panels. Using ac small signal analysis to these equations it has led to the derivation of transfer functions representing the dynamic responses of voltages across PV_1 and PV_2 in response to variations of converter switch duty ratio. Analysis of this transfer function model through Bode and Root locus plots

has been performed to reveal its stability margins under different duty ratio variation ranges. Step response test of the model has been carried out, and results are compared with that from experimental prototype in the laboratory. The exercise confirmed that the model is largely accurate and hence plausible for being used to controller design and tuning

- A comprehensive study of the power harness from two photovoltaic panels connected in series under partial shading while interface either with bypass diodes or a bidirectional Ćuk converter is performed. The comparisons of the two solutions under different irradiation levels lead to the creation of a control scheme which minimizes power losses inherent to the system. The control scheme is then verified by simulations where power delivered increases up to 32% under severe shading conditions in comparison of two PV panels connected in parallel with bypass diodes.
- A novel maximum power point tracking algorithm has been developed. This combines a switching scheme and model based optimal control scheme. The former determines which switch pair in the bidirectional Ćuk converter to be active according to measured light levels on each PV panel and the latter has the ability to predict the optimal voltage values across the individual PV panels under any practical irradiance and temperature levels. This algorithm has been studied through simulations and compared with the widely used Perturb & Observe algorithm in simulation. Experimental verification of the new control algorithm has been performed and also contrasted with the P&O method. Though both are capable of finding the MPPs in any given lighting conditions, the newly proposed model based scheme can locate the optimal power points for individual PV panels as well as the complete system faster and more accurate than the P&O algorithm. A serious shortcoming of P&O method is identified which is caused by its inherent continuous adjustment of the duty ratio. This is that the system parameters contaminates with high level noise which may make it misallocating the optimal power points, hence inefficient and giving high electromagnetic interferences.

- An experimental prototype of an integrated bi-directional Ćuk converter and two PV panel system has been designed, constructed and tested by the author. A terminal boost converter is also built in the practical set-up functioning as the whole system power conditioner. These MOSFET-based converters are equipped with sensors and transducers for voltage/current measurements. The system is controlled by a TMS320F28335DSP-based microcontroller (eZdsp™ F28335), which can access input signals from 14 sensors suitable for similar systems containing up to three chained PV panels. Open and closed loop tests of this prototype has shown that it can function as desired in obtaining the maximum power generation corresponding to the measured weather conditions. A dynamic response test has been designed to subject the system to a series of scenarios where the combination pattern of irradiance level over each of the two PV panels is changed systematically. As expected, the system can activate the inner Ćuk converter switch-diode pair correctly and promptly hence improving the power harness from the PV panels under partial shading.
- The price of the DC/DC converter represents an investment of \$500dolls and the commercial equivalent is from the brand SolarEdge, model OP600-96V which is listed with a retail price of \$170.00. Considering SolarEdge converter as a mass production instrument, the price of the bi-directional Ćuk converter could be improved in order to compete the nowadays offer.

To date, one conference paper has been presented based on the work described in Chapter 5. A journal paper detailing the mathematical model and experimental verification is being prepared. In addition, a second journal paper is being assembled including experimental results presented in Chapter 7.

8.1 Recommendations for Future Work

There are multiple directions in which this research can be refined and expanded. The follows are a list of recommended areas that the research can be carried out.

- The mathematical model presented in this report could be used to develop other control techniques which once completed can be directly applied by Simulink to the prototype.
- Since the MPP duty ratio is located in a narrow space from 40% to 60% in this application, A high resolution PWM signal could be used as improvement of this research
- Further analysis and practical implementation could be done using the experimental prototype to study cases where three or more PV panels are connected to bidirectional converters.
- Although this thesis is concentrated in the Ćuk converter topology, other bidirectional topologies can fulfil the role of this. A full study that involves all the bidirectional topologies integrated to PV panels can be done. The efficiency of different integrated converter topologies with PV panels should be studied and compared.
- Having an experimental prototype completed and working, one can use a high level programming interface software such as Simulink to develop different maximum power point trackers. Automatic algorithms such as Fuzzy logic and Neural networks model based control schemes could be explored.

With the continuation of these recommendations for the future research, it is hoped to achieve significant contributions to the field and lead to publications with high impact.

Appendix A

AC Small Signal Analysis Derivation

$$L_1 \frac{d[I_{L1} + \hat{i}_{L1}]}{dt} = V_{Pv1} + \hat{v}_{Pv1} - [(1 - K) + \hat{k}](V_{Cn} + \hat{v}_{Cn})$$

$$\overbrace{L_1 \frac{dI_{L1}}{dt}}^0 + L_1 \frac{d\hat{i}_{L1}}{dt} = \overbrace{V_{Pv1}}^0 + \hat{v}_{Pv1} - \left[\overbrace{V_{Cn}(1 - K)}^0 + V_{Cn}\hat{k} + \hat{v}_{Cn}(1 - K) + \overbrace{\hat{v}_{Cn}\hat{k}}^0 \right]$$

$$\Rightarrow L_1 \frac{d\hat{i}_{L1}}{dt} = \hat{v}_{Pv1} - V_{Cn}\hat{k} - \hat{v}_{Cn}(1 - K)$$

$$L_2 \frac{d[I_{L2} + \hat{i}_{L2}]}{dt} = (K - \hat{k})(V_{Cn} + \hat{v}_{Cn}) - (V_{Pv2} + \hat{v}_{Pv2})$$

$$\overbrace{L_2 \frac{dI_{L2}}{dt}}^0 + L_2 \frac{d\hat{i}_{L2}}{dt} = \overbrace{V_{Cn}K}^0 + \hat{v}_{Cn}K + V_{Cn}\hat{k} + \overbrace{\hat{v}_{Cn}\hat{k}}^0 - \overbrace{V_{Pv2}}^0 - \hat{v}_{Pv2}$$

$$\Rightarrow L_2 \frac{d\hat{i}_{L2}}{dt} = \hat{v}_{Cn}K + V_{Cn}\hat{k} - \hat{v}_{Pv2}$$

$$C_1 \frac{d\hat{v}_{Pv1}}{dt} = \hat{i}_{Pv1} - \hat{i}_T - \hat{i}_{L1}$$

$$\Rightarrow C_1 \frac{d\hat{v}_{Pv1}}{dt} = -\frac{\hat{v}_{Pv1}}{R_{Pv1}} - \hat{i}_T - \hat{i}_{L1}$$

$$C_2 \frac{d\hat{v}_{Pv2}}{dt} = \hat{i}_{Pv2} + \hat{i}_{L2} - \hat{i}_T$$

$$\Rightarrow C_2 \frac{d\hat{v}_{Pv2}}{dt} = -\frac{\hat{v}_{Pv2}}{R_{Pv2}} + \hat{i}_{L2} - \hat{i}_T$$

$$C_n \frac{d[V_{Cn} + \hat{v}_{Cn}]}{dt} = (I_{L1} + \hat{i}_{L1})[(1 - K) - \hat{k}] - (K + \hat{k})(I_{L2} + \hat{i}_{L2})$$

$$\overbrace{C_n \frac{dV_{Cn}}{dt}}^0 + C_n \frac{d\hat{v}_{Cn}}{dt}$$

$$= \overbrace{I_{L1}(1 - K)}^0 - I_{L1}\hat{k} + \hat{i}_{L1}(1 - K) - \overbrace{\hat{i}_{L1}\hat{k}}^0 - \left[\overbrace{I_{L2}K}^0 + \hat{i}_{L2}K + I_{L2}\hat{k} + \overbrace{\hat{i}_{L2}\hat{k}}^0 \right]$$

$$\Rightarrow C_n \frac{d\hat{v}_{Cn}}{dt} = -I_{L1}\hat{k} + \hat{i}_{L1}(1 - K) - \hat{i}_{L2}K - I_{L2}\hat{k}$$

Appendix B

Duty Ratio	Vpv1	Ipv1	Rpv1	Ppv1	Vpv2	Ipv2	Rpv2	Ppv2	Ptotal	
0.450	18.04	2.42	7.46	43.62	14.76	1.44	10.25	21.25	64.88	
MPP	0.475	17.22	2.72	6.33	46.87	15.58	1.27	12.25	19.82	66.69
0.500	16.40	2.95	5.56	48.36	16.40	1.11	14.73	18.25	66.62	
0.525	15.58	3.07	5.07	47.88	17.22	0.77	22.40	13.24	61.12	
0.550	14.76	3.15	4.69	46.49	18.04	0.20	90.79	3.58	50.08	
0.575	13.94	3.17	4.40	44.13	18.86	0.00	-	0.00	44.13	
0.600	13.12	3.22	4.07	42.27	19.68	0.00	-	0.00	42.27	

Table: Voltage, Current and Impedances of two PV panels under an uneven light condition G1 =100%, G2=50%

Appendix C

S-Function File

sfun1.m

```
function [sys,x0,str,ts] = sfun1(t,x,u,flag)

%*****Main Body for S-function*****
switch flag, % Determine the tasks to be done for specific flag

    % Initialising is done to define the structure information
case 0
[sys,x0,str,ts] = mdlInitializeSizes;

case 2 % Value is updated for the next sample
sys = mdlUpdate(t,x,u);

case 3 % Determining the output value
sys = mdlOutputs(t,x,u);

case {1,4,9} % Continuous states are not used
            % Variable sample sizes are not used
            % Emergency termination is not used
    sys = [];

otherwise
error(['Unhandled flag = ', num2str(flag)]); %Error handling
end;

%*****end of main body*****
%*****mdlInitializeSizes subroutine*****

function [sys,x0,str,ts]= mdlInitializeSizes;
%Call simsizes for a size structure, define it before converting it
%to the array sys.

sizes = simsizes;
sizes.NumContStates = 0;
sizes.NumDiscStates = 1;
sizes.NumOutputs =1;
sizes.NumInputs = 5;
sizes.DirFeedthrough =1;
sizes.NumSampleTimes = 1;

sys = simsizes(sizes);
x0 = 0;
str = [];
ts = [1e-5 0];
%*****end of initialization stage*****
%*****mdlUpdate subroutine*****

function sys = mdlUpdate(t,x,u)
    %next sample is updated through another subroutine

sys = compute(u(1),u(2),u(3),u(4),u(5));

%*****end of sampling update*****
%*****mdlOutputs subroutine*****
```

```
function sys = mdlOutputs(t,x,u)
    %the current discrete state is made available in output

sys = x;
%*****end of sampling update*****

%*****compute subroutine*****
function I=compute(H,Tamb,ns,np,V)

if (V<0)
    V=0;
end

%*****(Enter your own code)*****

A      = 1.72;           % A      = Ideality factor of silicon
                        %          = material used in cell
q      = 1.602e-19;     % q      = electron charge in Coulomb
k      = 1.380658e-23;  % k      = Boltzmann constant
Eg     = 1.00;          % Eg     = Energy bandgap of one cell in eV
Ior    = 19.9693e-6;    % Irr or I = reverse saturation I at ref T in A
Iscr   = 3.3;           % Iscr   = cell short circuit I at ref T in A
ki     = 0.0017;       % ki     = short circuit current temperature
                        %          = coefficient at Iscr in A/Celsius
Rs     = 5e-5;         % Rs     = typical series resistance of one
                        %          = cell in ohms ) literature
Rp     = 5e5;          % Rp     = typical paralel resistance of one
                        %          = cell in ohms )
Tr     = 301.18;       % Tr     = reference temperature in K
%*****Computation of Parameters of PV array*****
Ta     = Tamb + 273;    % Calculate cell temperature in K
Tc     = Ta+0.2*H/100 ; % Calculate cell temperature in K
                        % If NOCT is given then Tc=Ta+(NOCT-20)/0.8*G
Rsht   = (np/ns)*Rp;   % Calculate total parallel resistance
Rst    = (ns/np)*Rs;   % Calculate total series resistance
Is     = Ior * (Tc/ Tr)^3.* exp(q*Eg/(k*A)*((1/Tr) - 1/Tc)); % Calculate
                        %          = leakage current
Isc    = (Iscr + ki * ( Tc - Tr)) * H/100;% Calculate photovoltaic current
%*****Bishop View*****
%*****The following are values inherent to the leakage current term Ish**
a      =0.10;          % a      = Fraction of ohmic current involved
                        %          = in avalanche breakdown
em     =3.7;           % em     = Avalanche Breakdown Exponent
Vbr    =-4.0;         % Vbr    = Junction Breakdown Voltage

%*****
%*****
%With this method there is no need to solve iteratively (no for loops)
%since Vj in vector form so we can get values for V+I*Rs
%we make Vj in vector form so we can get values for I and V

%Vj=Vbr:0.1:0.7*ns;
Ishunt=V/Rsht.*(1+a*(1-(V/Vbr)).^(-em));
I=(np*Isc-(np*Is*(exp((q*V)/(ns*A*k*Tc))-1))-Ishunt)/(1+Rst/Rsht);
%V=Vj-(I*Rst);
if (I<0)
    I=0;
end
```

Appendix D

The Boost Converter will also be operating at 20 kHz and uses the same MOSFET and diode in the Ćuk converter. Assuming that the inductor L_{bus} charges and discharges linearly, its current ripple is given by [35], [59]:

$$\Delta I_{L_{bus}} = \frac{-V_T(V_{BUS} - V_T)}{fL_3V_{BUS}}$$

$$\Delta I_{L_{bus}} = \frac{V_T S_T}{fL_{bus}}$$

It is desired to keep the inductor's current ripple relatively low. It is known that the average current $I_{L_{bus}}$ is around 3.3 A. At full light conditions, solar modules operate at 16.2 volts, and thus the terminal voltage will be around 32.4V:

$$\Delta I_{L_{bus}} = \frac{V_T S_T}{fL_{bus}} = \frac{32.4 \cdot 0.5}{20 \text{ kHz} \cdot 1 \text{ mH}} = 0.81$$

$$\% \Delta I_{L_{bus}} = \frac{\Delta I_{L_{bus}}}{I_{L_{bus}}} \times 100 = \frac{0.81}{3.3} \times 100 = 25\%$$

Although this is a relatively high, this will not affect the boost operation and will be enough for research purposes. It decided to have the value of 1mH due to the high cost. The electrolytic capacitors chosen for the input and output have 82 μF .

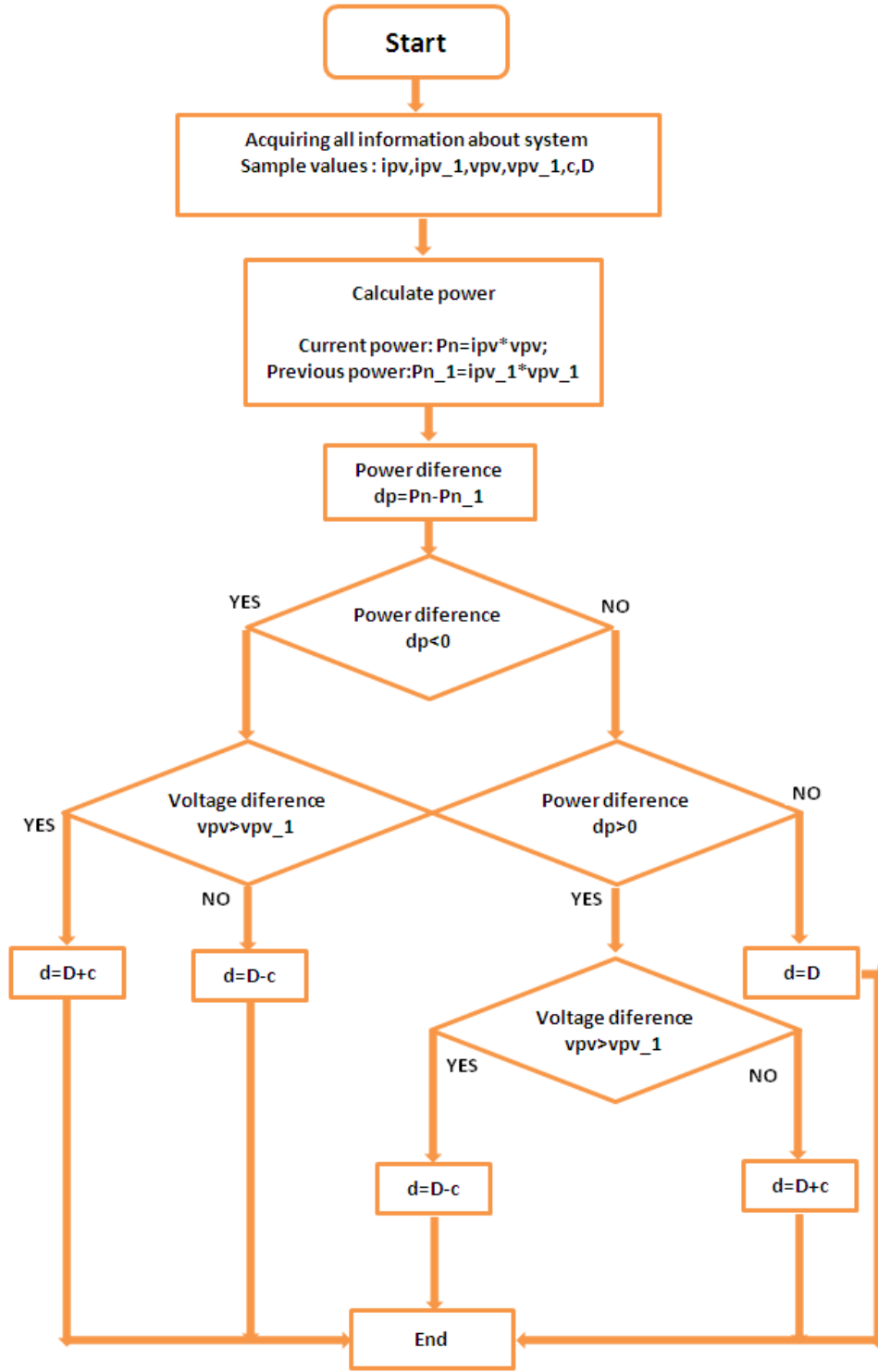
$$\Delta V_{C_{out}} = \frac{1}{C_{out}} \int_0^{T_{on}} I_{C_{out}} dt = \frac{1}{C_{out}} \int_0^{T_{on}} I_{out} dt = \frac{I_{out}k}{fC_{out}}$$

Since the Bus voltage is 60V, and the input voltage will be around 32V, $S_T \approx 0.47$.

$$\Delta V_{C_{out}} = \frac{I_{out}k}{fC_{out}} = \frac{1.65 \cdot 0.45}{20 \text{ kHz} \cdot 82 \mu\text{F}} = 0.453$$

$$\% \Delta V_{C_{out}} = \frac{\Delta V_{C_{out}}}{V_{C_{out}}} \times 100 = \frac{0.453}{60} \times 100 = 0.754\%$$

Appendix E



S-function File

PO.m

```
function [sys,x0,str,ts] = PO(t,x,u,flag)

%*****Main Body for S-function*****
switch flag, % Determine the tasks to be done for specific flag

    % Initialising is done to define the structure information
case 0
[sys,x0,str,ts] = mdlInitializeSizes;

case 2 % Value is updated for the next sample
sys = mdlUpdate(t,x,u);

case 3 % Determining the output value
sys = mdlOutputs(t,x,u);

case {1,4,9} % Continuous states are not used
            % Variable sample sizes are not used
            % Emergency termination is not used
    sys = [];

otherwise
error(['Unhandled flag = ', num2str(flag)]); %Error handling
end;

%*****end of main body*****
%*****mdlInitializeSizes subroutine*****

function [sys,x0,str,ts]= mdlInitializeSizes;
%Call simsizes for a size structure, define it before converting it
%to the array sys.

sizes = simsizes;
sizes.NumContStates = 0;
sizes.NumDiscStates = 1;
sizes.NumOutputs =1;
sizes.NumInputs = 6;
sizes.DirFeedthrough =1;
sizes.NumSampleTimes = 1;

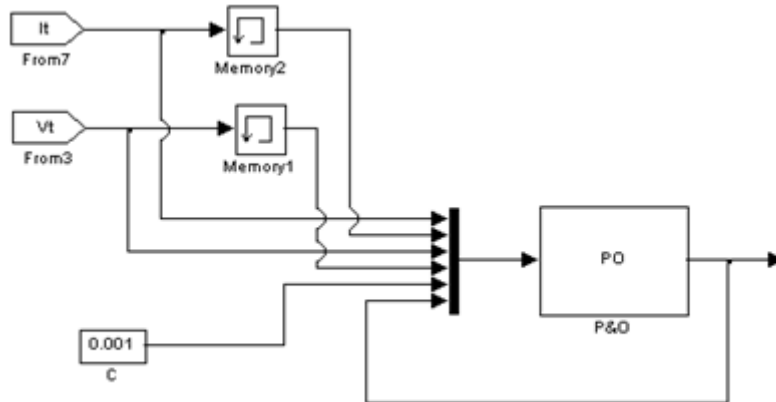
sys = simsizes(sizes);
x0 = 0;
str = [];
ts = [1e-4 0];
%*****end of initialization stage*****
%*****mdlUpdate subroutine*****

function sys = mdlUpdate(t,x,u)
    %next sample is updated through another subroutine

sys = compute(u(1),u(2),u(3),u(4),u(5),u(6));

%*****end of sampling update*****
```

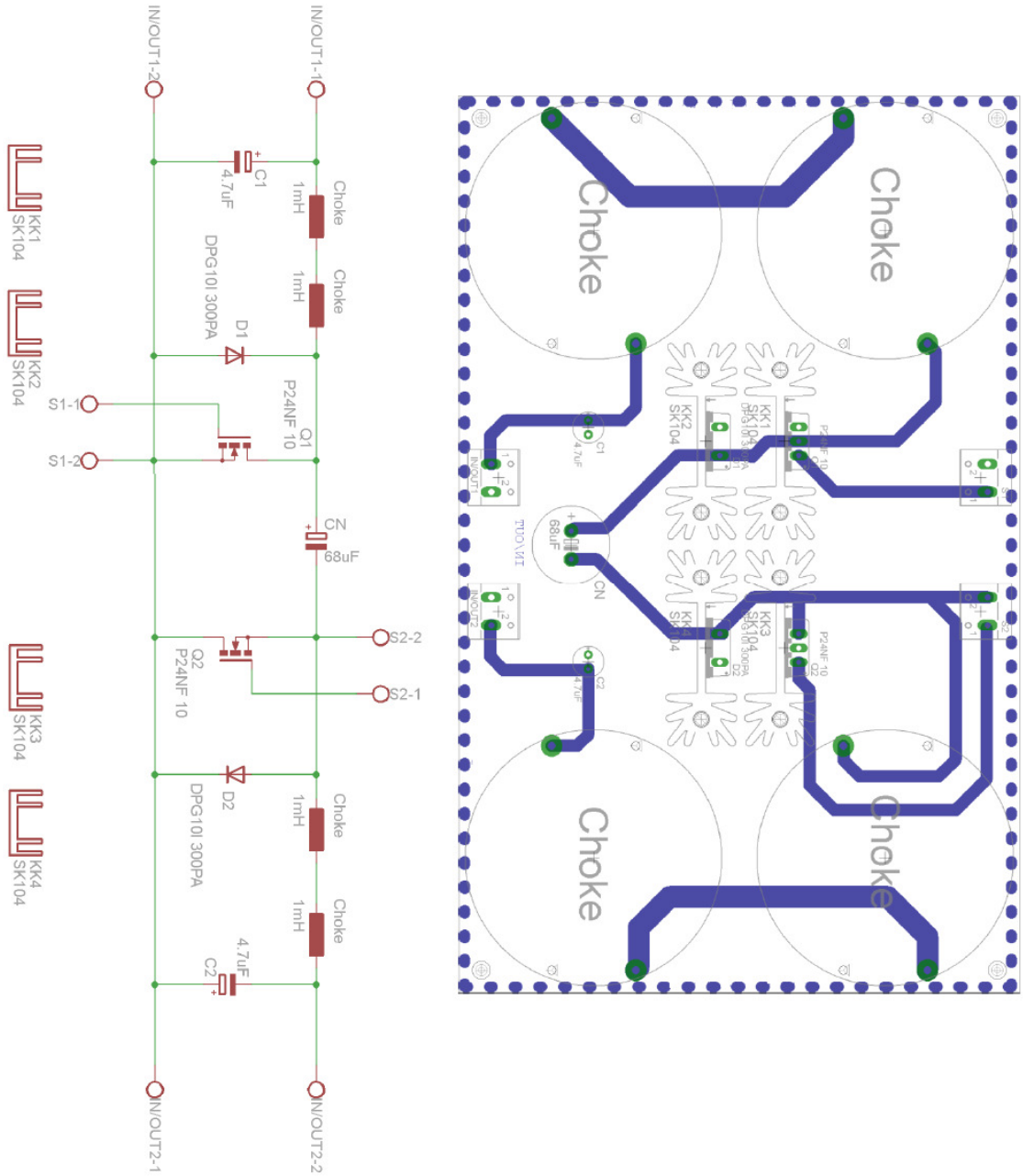
```
*****mdlOutputs subroutine*****  
  
function sys = mdlOutputs(t,x,u)  
    %the current discrete state is made available in output  
  
    sys = x;  
    %*****end of sampling update*****  
  
    %*****compute subroutine*****  
    function d=compute(ipv,ipv_1,vpv,vpv_1,c,D)  
  
        Pn=ipv*vpv; %PV output power  
        Pn_1=ipv_1*vpv_1;  
        dp=Pn-Pn_1; %power difference  
        if (dp<0)  
            if (vpv>vpv_1)  
                d=D+c;  
            else  
                d=D-c;  
            end  
        else if (dp>0)  
            if (vpv>vpv_1)  
                d=D-c;  
            else  
                d=D+c;  
            end  
        else  
            d=D;  
        end  
    end  
    %*****end of computation*****
```



Subsystem MPPT P&O

Appendix F

Bidirectional Ćuk Converter PCB diagram



Appendix G

Efficiency test of the Ćuk Converter at different voltage levels

$$V_{in} = 4 V$$

k (%)	V_{out} (V)	I_{in} (A)	I_{out} (A)	V_{out}/ V_{in}	P_{in} (W)	P_{out} (W)	P_{out}/ P_{in}
20	0.5	0.01	0.02	0.125	0.04	0.010	0.250
30	1.2	0.02	0.03	0.300	0.08	0.036	0.450
40	2.0	0.05	0.06	0.500	0.20	0.120	0.600
50	3.3	0.11	0.10	0.825	0.44	0.330	0.750
60	5.1	0.24	0.15	1.275	0.96	0.765	0.797
70	7.7	0.55	0.22	1.925	2.20	1.694	0.770

$$V_{in} = 6 V$$

k (%)	V_{out} (V)	I_{in} (A)	I_{out} (A)	V_{out}/ V_{in}	P_{in} (W)	P_{out} (W)	P_{out}/ P_{in}
20	1.0	0.01	0.03	0.167	0.06	0.030	0.500
30	2.0	0.03	0.06	0.333	0.18	0.120	0.667
40	3.4	0.08	0.10	0.567	0.48	0.340	0.708
50	5.3	0.17	0.15	0.883	1.02	0.795	0.779
60	8.0	0.38	0.23	1.333	2.28	1.840	0.807
70	11.9	0.84	0.35	1.983	5.04	4.165	0.826

$$V_{in} = 8 V$$

k (%)	V_{out} (V)	I_{in} (A)	I_{out} (A)	V_{out}/ V_{in}	P_{in} (W)	P_{out} (W)	P_{out}/ P_{in}
20	1.5	0.02	0.04	0.188	0.16	0.06	0.375
30	2.9	0.05	0.08	0.363	0.40	0.232	0.580
40	4.7	0.10	0.14	0.588	0.80	0.658	0.823
50	7.3	0.24	0.21	0.913	1.92	1.533	0.798
60	10.8	0.51	0.32	1.350	4.08	3.456	0.847
70	16.1	1.15	0.47	2.013	9.20	7.567	0.823

$$V_{in} = 10 V$$

k (%)	V_{out} (V)	I_{in} (A)	I_{out} (A)	V_{out}/ V_{in}	P_{in} (W)	P_{out} (W)	P_{out}/ P_{in}
20	2.0	0.02	0.06	0.200	0.20	0.120	0.600
30	3.7	0.06	0.11	0.370	0.60	0.407	0.678
40	6.0	0.13	0.17	0.600	1.30	1.020	0.785
50	9.2	0.29	0.27	0.920	2.90	2.484	0.857
60	13.9	0.66	0.40	1.390	6.60	5.560	0.842
70	20.3	1.45	0.59	2.030	14.50	11.977	0.826

$$V_{in} = 12 V$$

k (%)	V_{out} (V)	I_{in} (A)	I_{out} (A)	V_{out}/ V_{in}	P_{in} (W)	P_{out} (W)	P_{out}/ P_{in}
20	2.5	0.03	0.07	0.208	0.36	0.175	0.486
30	4.5	0.07	0.13	0.375	0.84	0.585	0.696
40	7.3	0.16	0.21	0.608	1.92	1.533	0.798
50	11.2	0.36	0.34	0.933	4.32	3.808	0.881
60	16.7	0.80	0.49	1.392	9.60	8.183	0.852
70	24.4	1.76	0.71	2.033	21.12	17.324	0.820

$$V_{in} = 14 V$$

k (%)	V_{out} (V)	I_{in} (A)	I_{out} (A)	V_{out}/ V_{in}	P_{in} (W)	P_{out} (W)	P_{out}/ P_{in}
20	3.0	0.03	0.09	0.214	0.42	0.270	0.643
30	5.5	0.08	0.16	0.393	1.12	0.880	0.786
40	8.7	0.19	0.25	0.621	2.66	2.175	0.818
50	13.2	0.43	0.39	0.943	6.02	5.148	0.855
60	19.9	0.97	0.58	1.421	13.58	11.542	0.850
70	28.6	2.06	0.84	2.043	28.84	24.024	0.833

$$V_{in} = 16 V$$

k (%)	V_{out} (V)	I_{in} (A)	I_{out} (A)	V_{out}/ V_{in}	P_{in} (W)	P_{out} (W)	P_{out}/ P_{in}
20	3.6	0.04	0.10	0.225	0.64	0.36	0.563
30	6.3	0.10	0.18	0.394	1.60	1.134	0.709
40	10.0	0.22	0.29	0.625	3.52	2.900	0.824
50	15.2	0.49	0.44	0.950	7.84	6.688	0.853
60	22.6	1.09	0.66	1.413	17.44	14.916	0.855
70	32.9	2.38	0.96	2.056	38.08	31.584	0.829

$$V_{in} = 18 V$$

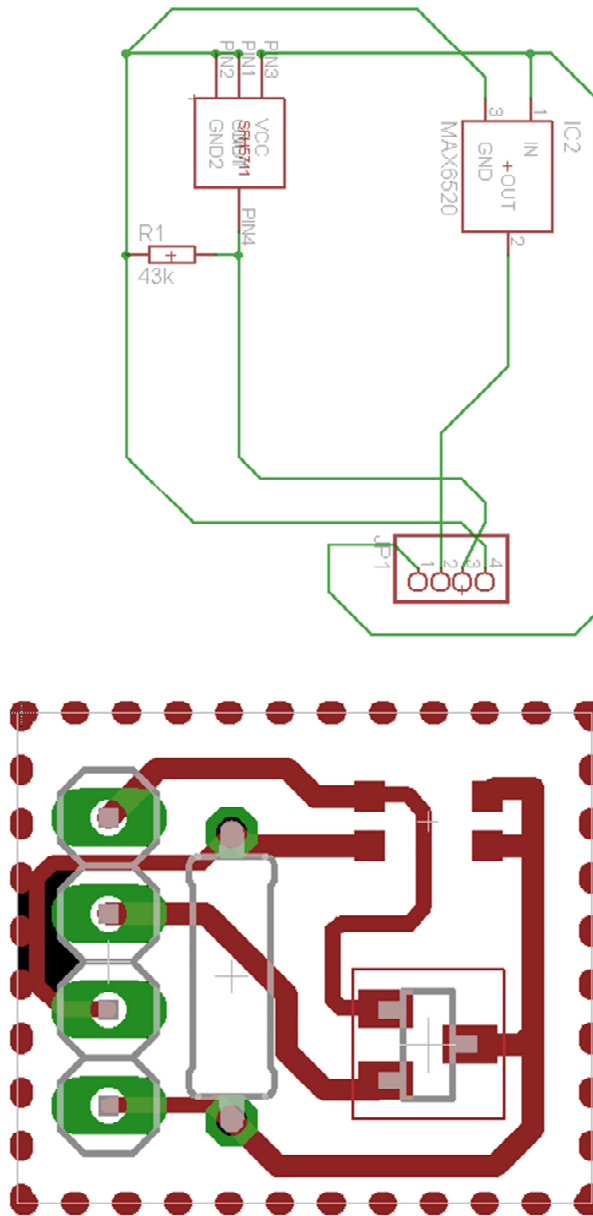
k (%)	V_{out} (V)	I_{in} (A)	I_{out} (A)	V_{out}/ V_{in}	P_{in} (W)	P_{out} (W)	P_{out}/ P_{in}
20	4.0	0.04	0.13	0.222	0.72	0.52	0.722
30	7.3	0.11	0.22	0.406	1.98	1.606	0.811
40	11.3	0.25	0.35	0.628	4.50	3.955	0.879
50	17.4	0.57	0.59	0.967	10.26	10.266	1.001
60	25.3	1.22	0.85	1.406	21.96	21.505	0.979
70	36.7	2.67	1.24	2.039	48.06	45.508	0.947

$$V_{in} = 20 V$$

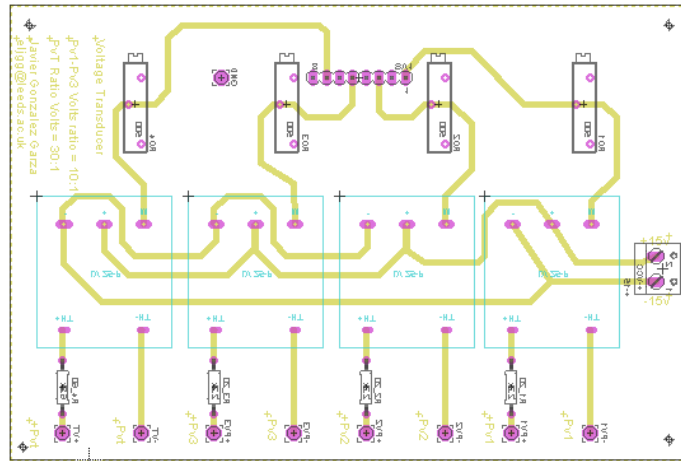
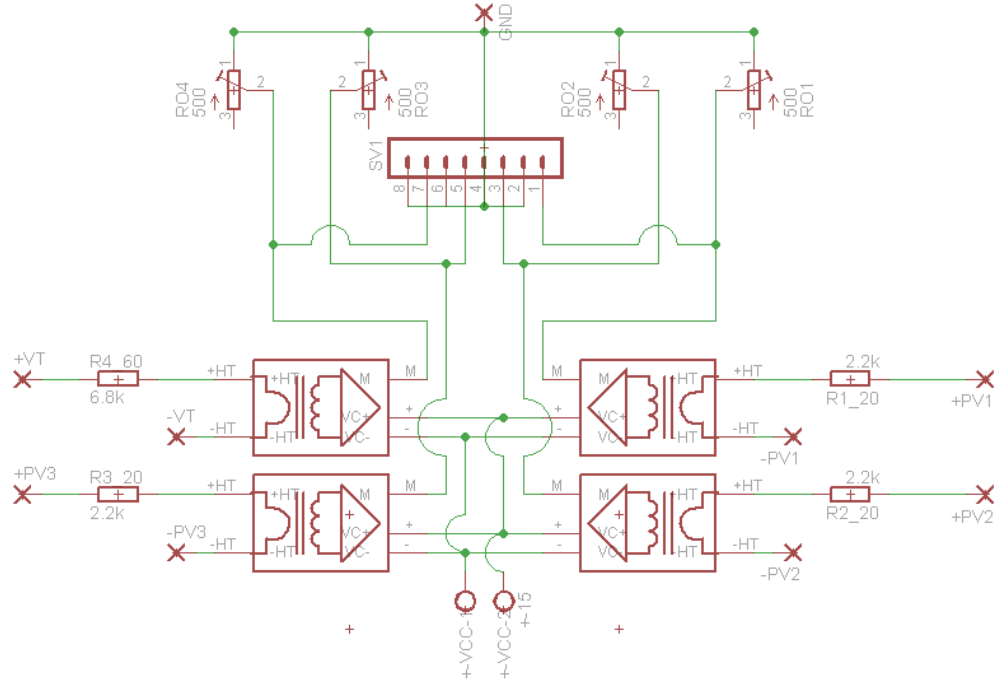
k (%)	V_{out} (V)	I_{in} (A)	I_{out} (A)	V_{out}/ V_{in}	P_{in} (W)	P_{out} (W)	P_{out}/ P_{in}
20	4.6	0.05	0.15	0.230	1.00	0.690	0.690
30	8.2	0.13	0.25	0.410	2.60	2.050	0.788
40	12.9	0.29	0.42	0.645	5.80	5.418	0.934
50	19.3	0.64	0.66	0.965	12.80	12.738	0.995
60	28.8	1.42	1.02	1.440	28.40	29.376	1.000
70	40.9	2.97	1.39	2.045	59.40	56.851	0.957

Appendix H

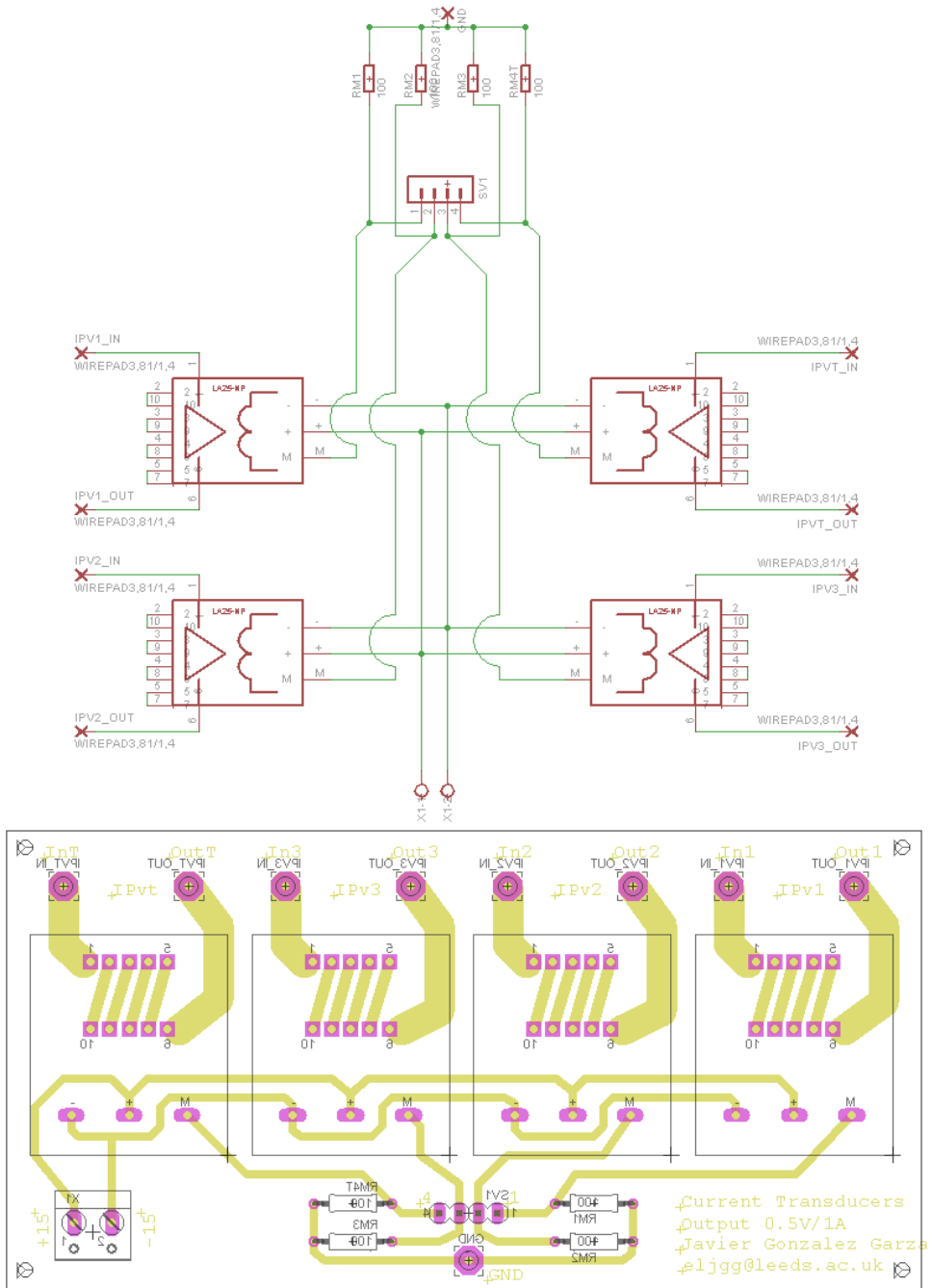
Irradiance and temperature sensor PCB board design



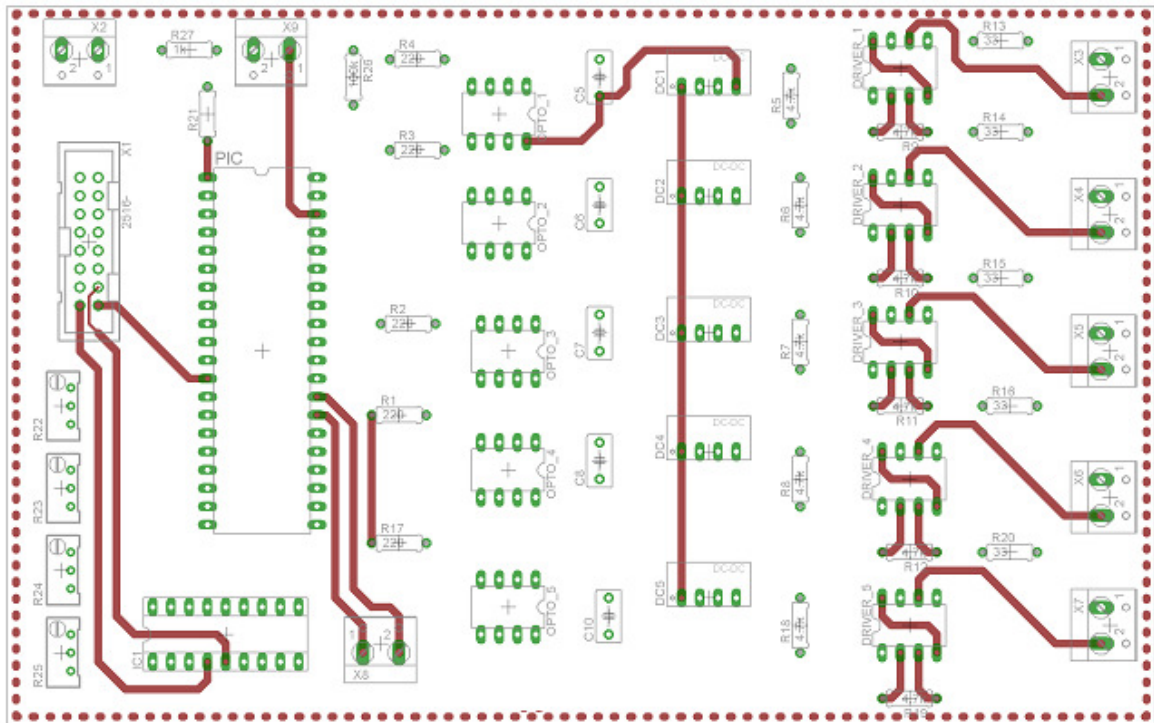
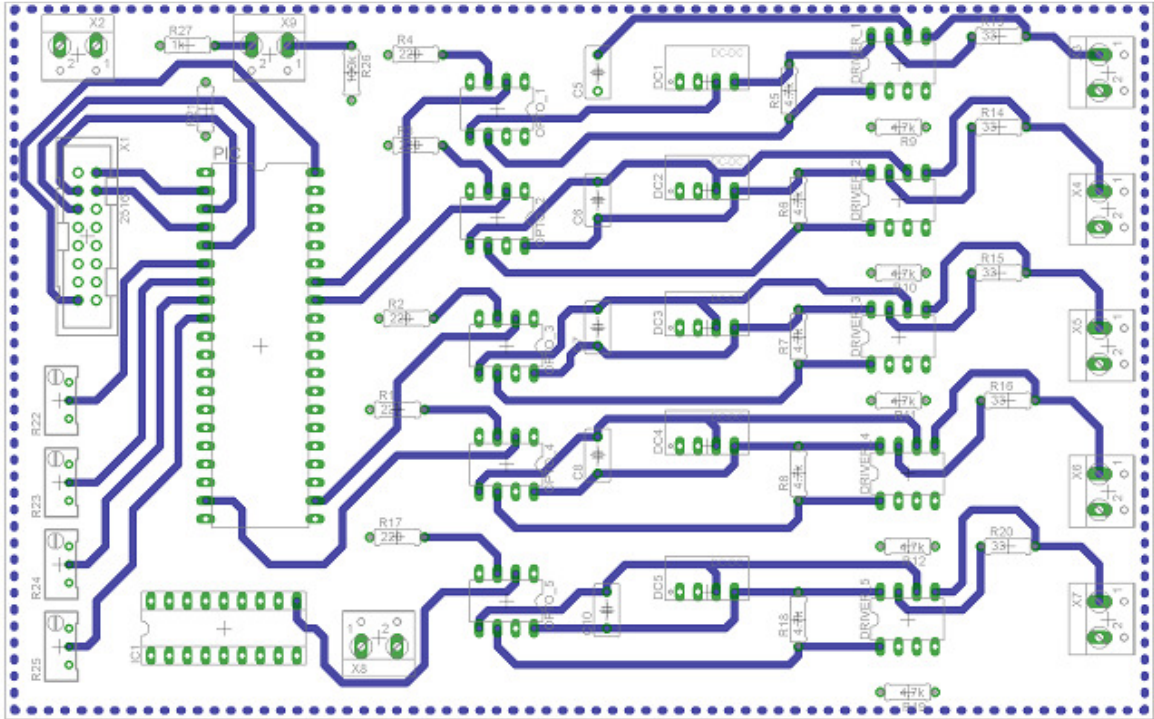
Appendix I



Appendix J



Appendix K



Bibliography

- [1] International Energy Agency, "Trends In Photovoltaic Applications 2013," 2013.
- [2] J. Gray, *Handbook of Photovoltaic Science and Engineering*. Chichester, UK: John Wiley & Sons, Ltd, 2005, p. Chapter 3. The Physics of the Solar Cell.
- [3] G. Masters, *Renewable and Efficient Electric Power Systems*. Wiley-IEEE Press, 2005, p. 680.
- [4] S. B. Kjaer, J. K. Pedersen, and F. Blaabjerg, "A Review of Single-Phase Grid-Connected Inverters for Photovoltaic Modules," *IEEE Trans. Ind. Appl.*, vol. 41, no. 5, pp. 1292–1306, Sep. 2005.
- [5] A. N. A. Ali, M. H. Saied, M. Z. Mostafa, and T. M. Abdel- Moneim, "A survey of maximum PPT techniques of PV systems," in *2012 IEEE Energytech*, 2012, pp. 1–17.
- [6] J. W. Bishop, "Computer simulation of the effects of electrical mismatches in photovoltaic cell interconnection circuits," *Sol. Cells*, vol. 25, no. 1, pp. 73–89, Oct. 1988.
- [7] R. Ramabadran and B. Mathur, "Matlab based modelling and performance study of series connected SPVA under partial shaded conditions," *J. Sustain. Dev.*, pp. 85–94, 2009.
- [8] M. C. Alonso-García and J. M. Ruíz, "Analysis and modelling the reverse characteristic of photovoltaic cells," *Sol. Energy Mater. Sol. Cells*, vol. 90, no. 7–8, pp. 1105–1120, May 2006.
- [9] M. C. Alonso-García, J. M. Ruiz, and W. Herrmann, "Computer simulation of shading effects in photovoltaic arrays," *Renew. Energy*, vol. 31, no. 12, pp. 1986–1993, Oct. 2006.
- [10] D. Sera, R. Teodorescu, and P. Rodriguez, "PV panel model based on datasheet values," in *2007 IEEE International Symposium on Industrial Electronics*, 2007, no. 4, pp. 2392–2396.
- [11] M. S. IMAMURA, "A SIMPLIFIED METHOD FOR DETERMINING THE AVAILABLE POWER AND ENERGY OF A PHOTOVOLTAIC ARRAY," *Int. J. Sol. Energy*, vol. 10, no. 3–4, pp. 205–210, Oct. 1991.

- [12] W. Xiao, F. F. Edwin, G. Spagnuolo, and J. Jatskevich, "Efficient Approaches for Modeling and Simulating Photovoltaic Power Systems," *IEEE J. Photovoltaics*, vol. 3, no. 1, pp. 500–508, Jan. 2013.
- [13] V. Di Dio, D. La Cascia, R. Miceli, and C. Rando, "A mathematical model to determine the electrical energy production in photovoltaic fields under mismatch effect," in *2009 International Conference on Clean Electrical Power*, 2009, pp. 46–51.
- [14] S.-H. Park, "C-language based PV array simulation technique considering effects of partial shading," in *2009 IEEE International Conference on Industrial Technology*, 2009, no. 1, pp. 1–6.
- [15] M. Seyedmahmoudian, S. Mekhilef, R. Rahmani, R. Yusof, and E. Renani, "Analytical Modeling of Partially Shaded Photovoltaic Systems," *Energies*, vol. 6, no. 1, pp. 128–144, Jan. 2013.
- [16] a. Kajihara and T. Harakawa, "Model of Photovoltaic Cell Circuits under Partial Shading," in *2005 IEEE International Conference on Industrial Technology*, 2005, pp. 866–870.
- [17] P. Rodrigo, E. F. Fernández, F. Almonacid, and P. J. Pérez-Higueras, "A simple accurate model for the calculation of shading power losses in photovoltaic generators," *Sol. Energy*, vol. 93, pp. 322–333, Jul. 2013.
- [18] D. Nguyen and B. Lehman, "Modeling and Simulation of Solar PV Arrays under Changing Illumination Conditions," in *2006 IEEE Workshops on Computers in Power Electronics*, 2006, pp. 295–299.
- [19] H. Patel and V. Agarwal, "MATLAB-Based Modeling to Study the Effects of Partial Shading on PV Array Characteristics," *IEEE Trans. Energy Convers.*, vol. 23, no. 1, pp. 302–310, Mar. 2008.
- [20] G. Petrone, G. Spagnuolo, and M. Vitelli, "Analytical model of mismatched photovoltaic fields by means of Lambert W-function," *Sol. Energy Mater. Sol. Cells*, vol. 91, no. 18, pp. 1652–1657, Nov. 2007.
- [21] G. Vachtsevanos and K. Kalaitzakis, "A Hybrid Photovoltaic Simulator for Utility Interactive Studies," *IEEE Trans. Energy Convers.*, vol. EC-2, no. 2, pp. 227–231, Jun. 1987.
- [22] I. Caluianu, G. Notton, I. Colda, S. Caluianu, and A. Damian, "Photovoltaic energy generation under partially shading conditions," in *2009 8th International Symposium on Advanced Electromechanical Motion Systems & Electric Drives Joint Symposium*, 2009, no. July, pp. 1–6.

- [23] X. Weidong, W. G. Dunford, and A. Capel, "A novel modeling method for photovoltaic cells," in *2004 IEEE 35th Annual Power Electronics Specialists Conference (IEEE Cat. No.04CH37551)*, 2004, pp. 1950–1956.
- [24] R. Chenni, M. Makhlouf, T. Kerbache, and A. Bouzid, "A detailed modeling method for photovoltaic cells," *Energy*, vol. 32, no. 9, pp. 1724–1730, Sep. 2007.
- [25] F. González-Longatt, "Model of photovoltaic module in matlab," *II CIBELEC*, pp. 1–5, 2005.
- [26] K. W. Böer, "The physics of solar cells," *J. Appl. Phys.*, vol. 50, no. 8, p. 5356, 1979.
- [27] J. Nelson and M. Ratner, *The physics of solar cells*, vol. 57, no. 12. 2004, p. 71.
- [28] A. Merdassi, L. Gerbaud, and S. Bacha, "Automatic global modelling of static converters for power electronics systems: Taking into account of causality aspects for model coupling," in *Power Electronics and Applications, 2009. EPE '09. 13th European Conference on*, 2009, pp. 1–10.
- [29] E. Duran, J. Galan, M. Sidrach-de-Cardona, and J. M. Andujar, "A New Application of the Buck-Boost-Derived Converters to Obtain the I-V Curve of Photovoltaic Modules," in *2007 IEEE Power Electronics Specialists Conference*, 2007, pp. 413–417.
- [30] S. Silvestre, A. Boronat, and A. Chouder, "Study of bypass diodes configuration on PV modules," *Appl. Energy*, vol. 86, no. 9, pp. 1632–1640, Sep. 2009.
- [31] L. Hassaine, "Implementación de un Control Digital de Potencia Activa y Reactiva para Inversores. Aplicación a Sistemas Fotovoltaicos Conectados a Red," UNIVERSIDAD CARLOS III DE MADRID, 2010.
- [32] G. . Yu, Y. . Jung, J. . Choi, and G. . Kim, "A novel two-mode MPPT control algorithm based on comparative study of existing algorithms," *Sol. Energy*, vol. 76, no. 4, pp. 455–463, Apr. 2004.
- [33] G. Walker, "Evaluating MPPT converter topologies using a MATLAB PV model," *J. Electr. Electron. Eng.*, 2001.
- [34] R. Hanitscht, "Numerical simulation of current-voltage characteristics of photovoltaic systems with shaded solar cells," vol. 56, no. 6, pp. 513–520, 1996.

- [35] N. Mohan and T. M. Undeland, *Power electronics: converters, applications, and design*. John Wiley & Sons, 2007.
- [36] B. V. P. Chong, L. Zhang, and A. Dehghani, "Modelling & control of a bidirectional converter for a standalone photovoltaic power plant," in *2007 European Conference on Power Electronics and Applications*, 2007, pp. 1–10.
- [37] M. Abdulkadir, B. Musa, and I. Ali, "A REVIEW OF MAXIMUM POWER POINT TRACKING ALGORITHM FOR PHOTOVOLTAIC SYSTEM," *gifre.org*, vol. 1, no. 2, pp. 380–385, May 2011.
- [38] J. W. Bishop, "Microplasma breakdown and hot-spots in silicon solar cells," *Sol. Cells*, vol. 26, no. 4, pp. 335–349, Sep. 1989.
- [39] SHOWTEC, "SHOWTEC SUNSTRIP 1." [Online]. Available: <http://shop.showtec.co.uk/showtec-sunstrip-1?keyword=30642>.
- [40] Sunsei, "Sunsei," *SOLAR PANEL 100W*, 2007. [Online]. Available: <http://cpc.farnell.com/1/1/41472-panel-solar-100w-sunsei-se-6000-icp-global-technologies.html>.
- [41] F. Blaabjerg, F. Iov, T. Kerekes, and R. Teodorescu, "Trends in power electronics and control of renewable energy systems," in *Proceedings of 14th International Power Electronics and Motion Control Conference EPE-PEMC 2010*, 2010.
- [42] L. Martinez Salamero, A. Cid-Pastor, A. El Aroudi, R. Giral, and J. Calvente, "Modelado y Control de Convertidores Conmutados Continua-Continua: Una perspectiva Tutorial," *Rev. Iberoam. Automática e Informática Ind. RIAI*, vol. 6, no. 4, pp. 5–20, Oct. 2009.
- [43] G. R. Walker and P. C. Sernia, "Cascaded DC–DC Converter Connection of Photovoltaic Modules," *IEEE Trans. Power Electron.*, vol. 19, no. 4, pp. 1130–1139, Jul. 2004.
- [44] G. R. Walker and J. C. Pierce, "PhotoVoltaic DC-DC Module Integrated Converter for Novel Cascaded and Bypass Grid Connection Topologies — Design and Optimisation," in *37th IEEE Power Electronics Specialists Conference*, 2004, pp. 1–7.
- [45] A. Sanz, I. Vidaurrazaga, A. Pereda, R. Alonso, E. Roman, and V. Martinez, "Centralized vs distributed (power optimizer) PV system architecture field test results under mismatched operating conditions," in *2011 37th IEEE Photovoltaic Specialists Conference*, 2011, pp. 002435–002440.

- [46] Y. Chen, Y. Liu, and S. Lin, "Double-Input PWM DC/DC Converter for High-/Low-Voltage Sources," *IEEE Trans. Ind. Electron.*, vol. 53, no. 5, pp. 1538–1545, Oct. 2006.
- [47] B. Bryant and M. Kazimierczuk, "Derivation of the Cuk PWM DC-DC converter circuit topology," in *Proceedings of the 2003 International Symposium on Circuits and Systems, 2003. ISCAS '03.*, 2003, vol. 3, pp. III–292–III–295.
- [48] S. Cuk and R. Middlebrook, "A new optimum topology switching dc-to-dc converter," *Power Electron. Spec. ...*, 1977.
- [49] V. MAHOUT and V. BOITIER, "Nonlinear control of a photovoltaic converter," *choice*, no. 2, pp. 1–5, 2003.
- [50] R. W. Erickson, "DC-DC Power Converters," in *Wiley Encyclopedia of Electrical and Electronics Engineering*, John Wiley & Sons, Inc., 2001.
- [51] A. I. Bratcu, I. Munteanu, S. Bacha, D. Picault, and B. Raison, "Cascaded DC–DC Converter Photovoltaic Systems: Power Optimization Issues," *IEEE Trans. Ind. Electron.*, vol. 58, no. 2, pp. 403–411, Feb. 2011.
- [52] F. L. Luo and Y. Hong, "Classical DC/DC Converters," in *Renewable Energy Systems*, CRC Press, 2012, pp. 203–248.
- [53] M. Kazimierczuk, D. Q. Vuong, B. T. Nguyen, and J. A. Weimer, "Topologies of bidirectional PWM dc-dc power converters," in *Proceedings of the IEEE 1993 National Aerospace and Electronics Conference-NAECON 1993*, 1993, pp. 435–441.
- [54] P. Bhatnagar and R. K. Nema, "Maximum power point tracking control techniques: State-of-the-art in photovoltaic applications," *Renew. Sustain. Energy Rev.*, vol. 23, pp. 224–241, Jul. 2013.
- [55] F. Blaabjerg, F. Iov, R. Teodorescu, and Z. Chen, "Power Electronics in Renewable Energy Systems," in *2006 12th International Power Electronics and Motion Control Conference*, 2006, pp. 1–17.
- [56] Y. Fuad, W. L. De Koning, and J. W. Van Der Woude, "Pulse-width modulated d.c.-d.c. converters," *Int. J. Electr. Eng. Educ.*, vol. 38, no. 1, pp. 54–79, 2001.
- [57] E. Wittenbreder, "Buck and boost power converters with non-pulsating input and output terminal currents," US Patent 6,252,383 (<http://www.google.com/patents/US6252383>), 2001.

- [58] O. Gomis-Bellmunt, D. Montesinos-Miracle, S. Galceran-Arellano, and J. Rull-Duran, "Sliding mode control based buck-boost bidirectional converter to drive piezoelectric loads," *Electr. Eng.*, vol. 90, no. 2, pp. 115–125, May 2007.
- [59] M. H. Rashid, *Power Electronics Handbook: Devices, Circuits, and Applications*, Second Edi. Academic Press, 2001, p. Chapter 13, DC–DC Converters.
- [60] S. Cuk, "Modeling, analysis, and design of switching converters," California Institute of Technology (Doctoral Thesis) , <http://adsabs.harvard.edu/abs/1977PhDT.....76C>, 1977.
- [61] D. Challa and R. Inguva, "An Inverter Fed With Combined Wind-Solar Energy System Using CUK-SEPIC Converter," *Int. J. Eng.*, no. 9, pp. 1–8, 2012.
- [62] M. Zhang, F. Wang, and J. Yang, "Novel Cuk circuit and Its application in photovoltaic system," *Power Electron. Syst. Appl. 2009. PESA 2009. 3rd Int. Conf.*, vol. 1, pp. 2–5, 2009.
- [63] V. R. Nasirian, Y. Karimi, M. R. Zolghadri, M. Ahmadian, A. Moayedi, and A. Davoudi, "Small-signal modeling and fast response control strategy for DCVM Cúk converters in PFC applications," in *2011 Twenty-Sixth Annual IEEE Applied Power Electronics Conference and Exposition (APEC)*, 2011, pp. 1795–1802.
- [64] J. Knight, S. Shirsavar, and W. Holderbaum, "An Improved Reliability Cuk Based Solar Inverter With Sliding Mode Control," *IEEE Trans. Power Electron.*, vol. 21, no. 4, pp. 1107–1115, Jul. 2006.
- [65] C. K. Tse, "Nonlinear Dynamic of the Cuk Converter," in *Complex Behavior of Switching Power Converters*, CRC Press, 2003.
- [66] S. Bae and A. Kwasinski, "Maximum power point tracker for a multiple-input Cuk dc-dc converter," *Telecommun. Energy Conf. ...*, 2009.
- [67] M. Gupta, "MPPT Simulation with DC Submersible Solar Pump using Output Sensing Direct Control Method and Cuk Converter," *Int. J. Renew. Energy Res. (...)*, vol. 3, no. 1, pp. 0–5, 2013.
- [68] J. Hallak, "Method for operating an inverter including boos, buck, and CUK converter topologies and arrangement for executing the method," US Patent 7,660,1382010.

- [69] N. Tiwari and D. Das, "MPPT CONTROLLER FOR PHOTO VOLTAIC SYSTEMS USING CUK DC/DC CONVERTOR," *ijater.com*, pp. 164–169, 2012.
- [70] M. Bidin, "Voltage tracking of a DC-DC CUK converter using neural network control," Universiti Tun Hussein Onn Malaysia (Doctoral dissertation) <http://eprints.uthm.edu.my/2922/>, 2012.
- [71] A. Nachez, "Aplicaciones de la conversión CC-CC Convertidor de Cuk," Universidad Nacional de Rosario (Thesis), 2004.
- [72] J. G. Garza, B. Chong, and L. Zhang, "Control of integrated Cuk converter and photovoltaic modules for maximum power generation," in *2012 3rd IEEE International Symposium on Power Electronics for Distributed Generation Systems (PEDG)*, 2012, vol. 2, pp. 175–181.
- [73] A. Safari and S. Mekhilef, "Simulation and Hardware Implementation of Incremental Conductance MPPT With Direct Control Method Using Cuk Converter," *IEEE Trans. Ind. Electron.*, vol. 58, no. 4, pp. 1154–1161, Apr. 2011.
- [74] B. Vui and P. Chong, "Optimal Design and Control of a Stand-alone Photovoltaic Power Plant Transfer Report," The University of Leeds, 2007.
- [75] P. Lei, G. Wei, and W. Yinghong, "Maximum power point tracking control of solar photovoltaic power generation system based on model reference adaptive," in *2009 International Conference on Sustainable Power Generation and Supply*, 2009, pp. 1–5.
- [76] M. Veerachary, T. Senjyu, and K. Uezato, "Analytical investigations for maximum power tracking of PV supplied IDB converter," in *2001 IEEE 32nd Annual Power Electronics Specialists Conference (IEEE Cat. No.01CH37230)*, 2001, vol. 1, pp. 205–209.
- [77] E. Duran, M. Sidrach-de-Cardona, J. Galan, and J. M. Andujar, "Comparative analysis of buck-boost converters used to obtain I–V characteristic curves of photovoltaic modules," in *2008 IEEE Power Electronics Specialists Conference*, 2008, pp. 2036–2042.
- [78] A. Mahmoud, H. Mashaly, S. A. Kandil, H. El Khashab, and M. N. F. Nashed, "Fuzzy logic implementation for photovoltaic maximum power tracking," in *2000 26th Annual Conference of the IEEE Industrial Electronics Society. IECON 2000. 2000 IEEE International Conference on Industrial Electronics, Control and Instrumentation. 21st Century Technologies and Industrial Opportunities (Cat. No.00CH37141)*, 2000, vol. 1, pp. 735–740.

- [79] E. SETIAWAN, I. HODAKA, and Y. YAMAMOTO, "Symbolic Analysis of Maximizing Efficiency of Photovoltaic Power Generation Circuits," *wseas.us*, pp. 49–52, 2012.
- [80] N. Femia, G. Lisi, G. Petrone, G. Spagnuolo, and M. Vitelli, "Distributed Maximum Power Point Tracking of Photovoltaic Arrays: Novel Approach and System Analysis," *IEEE Trans. Ind. Electron.*, vol. 55, no. 7, pp. 2610–2621, Jul. 2008.
- [81] V. Vorperian, "Simplified analysis of PWM converters using model of PWM switch. II. Discontinuous conduction mode," *IEEE Trans. Aerosp. Electron. Syst.*, vol. 26, no. 3, pp. 497–505, May 1990.
- [82] A. Bidram, A. Davoudi, and R. S. Balog, "Control and Circuit Techniques to Mitigate Partial Shading Effects in Photovoltaic Arrays," *IEEE J. Photovoltaics*, vol. 2, no. 4, pp. 532–546, Oct. 2012.
- [83] F. Luo and H. Ye, "Switched inductor two-quadrant DC/DC converter with neural network control," in *Proceedings of the IEEE 1999 International Conference on Power Electronics and Drive Systems. PEDS'99 (Cat. No.99TH8475)*, 1999, no. July, pp. 1114–1119 vol.2.
- [84] A. I. Bratcu, I. Munteanu, S. Bacha, D. Picault, and B. Raison, "Power optimization strategy for cascaded DC-DC converter architectures of photovoltaic modules," in *2009 IEEE International Conference on Industrial Technology*, 2009, pp. 1–8.
- [85] Z. M. Salameh, F. Dagher, and W. A. Lynch, "Step-down maximum power point tracker for photovoltaic systems," *Sol. Energy*, vol. 46, no. 5, pp. 279–282, Jan. 1991.
- [86] J. Bratt, "GRID CONNECTED PV INVERTERS: MODELING AND SIMULATION," San Diego State University, 2011.
- [87] A. R. Kashyap, R. Ahmadi, and J. W. Kimball, "Input voltage control of SEPIC for maximum power point tracking," in *2013 IEEE Power and Energy Conference at Illinois (PECI)*, 2013, pp. 30–35.
- [88] S. Kasat, "Analysis, design and modeling of DC-DC converter using simulink," Oklahoma State University, 2004.
- [89] G. N. Aldahim, A. N. Natsheh, and H. Oirkozak, "Control of Chaotic Behaviour in Parallel-Connected DC-DC Boost Converters," *Energy Procedia*, vol. 18, pp. 1275–1279, Jan. 2012.

- [90] G. G. Moshi, "Optimal Control of a PV-integrated Converter for Partial Shading Conditions," University of Leeds (MSc Dissertation), 2011.
- [91] R. Middlebrook and S. Cuk, "A general unified approach to modelling switching-converter power stages," *Power Electron. Spec. ...*, 1976.
- [92] B. V. P. Chong and L. Zhang, "Controller design for integrated PV-converter modules under partial shading conditions," *Sol. Energy*, vol. 92, pp. 123–138, Jun. 2013.
- [93] N. Femia, G. Petrone, G. Spagnuolo, and M. Vitelli, "Optimization of Perturb and Observe Maximum Power Point Tracking Method," *IEEE Trans. Power Electron.*, vol. 20, no. 4, pp. 963–973, Jul. 2005.
- [94] V. Salas, E. Olías, A. Barrado, and A. Lázaro, "Review of the maximum power point tracking algorithms for stand-alone photovoltaic systems," *Sol. Energy Mater. Sol. Cells*, vol. 90, no. 11, pp. 1555–1578, Jul. 2006.
- [95] K. Ogata, *Modern control engineering*, 4th Editio. Prentice-Hall Inc., NJ, 1997.
- [96] J. Ziegler and N. Nichols, "Optimum settings for automatic controllers," *trans. ASME*, 1942.
- [97] STMicroelectronics, "Datasheet MOSFET STB24NF10," no. November. pp. 1–7, 2000.
- [98] IXYS, "Datasheet Diode DPG10I300PA." IXYS SEMICONDUCTOR, 2006.
- [99] OSRAM, "Ambient Light Sensor SFH 5711." OSRAM, pp. 1–9, 2006.
- [100] Microchip, "Linear Temperature Sensor TC1047." Microship, pp. 1–12, 2012.
- [101] LEM, "Voltage Transducer LV 25-P." [Online]. Available: www.lem.com.
- [102] LEM, "Current Transducer LA 25-NP," 2011. .
- [103] E. Ramsden, *Hall-Effect Sensors: Theory and Application*. Newnes, 2006, pp. 1–272.
- [104] Texas Instrumens, "Microcontroller F28335." [Online]. Available: <http://www.ti.com/product/tms320f28335>.
- [105] R. Duma, P. Dobra, M. Abrudean, and M. Dobra, "Rapid prototyping of control systems using embedded target for TI C2000 DSP," in *2007 Mediterranean Conference on Control & Automation*, 2007, pp. 1–5.

- [106] D. Hercog, M. Curkovic, and K. Jezernik, "DSP based rapid control prototyping systems for engineering education and research," in *2006 IEEE Conference on Computer Aided Control System Design, 2006 IEEE International Conference on Control Applications, 2006 IEEE International Symposium on Intelligent Control*, 2006, pp. 2292–2297.
- [107] Mathworks, "Supported and Compatible Compilers – Release 2009b." [Online]. Available: <http://www.mathworks.co.uk/support/compilers/R2009b/index.html>.
- [108] Texas Instrumens, "TMS320x2833x Analog-to-Digital Converter (ADC) Module, Reference Guide SPRU812A," 2007.
- [109] P. Huynh and B. Cho, "Design and analysis of a regulated peak-power tracking system," *IEEE Trans. Aerosp. Electron. Syst.*, vol. 35, no. 1, pp. 84–92, 1999.
- [110] Texas Instrumens, "Enhanced Pulse Width Modulator (ePWM) , Reference Guide SPRUG04A," 2009.
- [111] Texas Instrumens, "High Resolution PWM, Reference Guide SPRUG02B," 2011. [Online]. Available: <http://www.ti.com/product/tms320f28335>.